U.S. DEPARTMENT OF COMMERCE
NATIONAL OCEANIC AND ATMOSPHERIC ADMINISTRATION
NATIONAL WEATHER SERVICE
NATIONAL CENTERS FOR ENVIRONMENTAL PREDICTION

OFFICE NOTE 426

THE INCLUSION OF GPS LIMB SOUNDING DATA INTO NCEP'S GLOBAL DATA ASSIMILATION SYSTEM

TAKAYUKI MATSUMURA
UCAR VISITING SCIENTIST/JAPAN METEOROLOGICAL AGENCY

JOHN C. DERBER
NOAA/NWS/NCEP/ENVIRONMENTAL MODELING CENTER

JAMES G. YOE
NESDIS/OFFICE OF RESEARCH AND APPLICATIONS

FRANCOIS VANDENBERGHE
NATIONAL CENTER FOR ATMOSPHERIC RESEARCH

XIAOLEI ZOU
FLORIDA STATE UNIVERISTY

JUNE 1999

Abstract

Global Positioning System (GPS) radio occultation data are examined using a ray tracing algorithm for potential incorporation in the National Centers for Environmental Prediction's (NCEP's) Spectral Statistical Interpolation (SSI) analysis system. First the observed bending angle is statistically compared with the simulated one. The investigation demonstrates that the simulated bending angle from the global analysis agrees well with the observed angle between the altitude of 7km and 35km. Next two case studies on super refraction are presented. The result suggests that the limb sounding technique often can only be applied above a certain critical altitude (200m-800m) where the near surface inversion is typically found in moist regions.

Experiments are then performed examining the impact of the data on analyses. The experiments show that the analysis procedure works properly and fits the observations reasonably. These results validate the reliability of the radio occultation data and the applicability of the assimilation procedure. However, while significant improvement on cost performance has been achieved for the ray tracing algorithm, considerable further effort (at least 2 orders of magnitude improvement is speed) is required to make the operational use of this data computationally feasible.

1. Introduction

The radio occultation sounding technique has been used since the 1960s to sense planetary atmospheres. The current availability of the Global Positioning System (GPS) makes it possible to derive the atmospheric information for our own planet. To demonstrate the potential capability of the GPS limb sounding technique, a low earth orbit (LEO) satellite carrying a GPS receiver was launched in April 1995 (Ware et. al., 1996). The University Corporation for Atmospheric Research / Payload Operations Control Center (UCAR/POCC) has processed and stored the data from this instrument and has made it widely available for research purposes.

The LEO satellite receives the GPS radio signal through the atmospheric limb and measures the excess phase delay of the GPS signal during the occultation. From this signal, a corresponding bending angle, the angle formed by the ray tangent vector at the transmitter and that at the receiver, can be estimated. When a radio signal passes through the Earth's limb, the ray trajectory is bent due to the gradient of the atmospheric refractivity. Since the refractivity relates to temperature, moisture and pressure of the atmosphere, a consecutive sequence of the bending angles for a certain occultation event provides information on the vertical profiles of these quantities.

In principle, a single LEO satellite can report about 500 sounding profiles a day globally in concert with the constellation of 24 GPS satellites. The vertical resolution of the soundings can be very high (200m) unlike other non-limb sounding space-based observations. Since the signal is obstructed neither by cloud nor rain, the soundings are available regardless of weather conditions around the occultation location. Measuring a phase delay insures highly accurate soundings without any long-term degradation nor dependency upon specific instruments. In addition, utilizing the existing GPS network should reduce the cost of the necessary instrumentation.

However, there are difficulties in using this data. Since the observations are produced after an integration along a long trajectory, the horizontal resolution of the observation can be relatively coarse (200km or more). Also, since the refractivity relates to a combination of temperature, moisture and pressure, it is not possible to determine the source of the signal without auxiliary information. Kursinski et.al. (1997) extensively discussed the spatial coverage, resolution, accuracy and error characteristics of the GPS radio occultation technique.

Eyre and Offiler (1998) examined requirements on the radio occultation measurement for inclusion in variational data assimilation. Variational data assimilation techniques have the potential to fully utilize the data by taking advantage of the strengths of the GPS data and accounting for the weaknesses. Variational techniques allow the incorporation of any type of observations when the analysis variables can be accurately transformed into the same form as the observation. It has been shown that substantial improvements in the impact of polar orbiting sounding data result from using radiance data rather than retrievals(e.g., Derber and Wu, 1998 and McNally et al., 1999). Note that much of the improvement for the polar orbiting data resulted because the quality control and the definition of the observational errors could be done better in terms of the radiance observations. Although several studies estimating the potential impact of the GPS limb sounding data capability have been reported (e.g., Leroy, 1997, Rocken et. al., 1997 and Kuo et. al., 1998), they have primarily examined retrieved temperature profiles obtained by means of the Abelian inversion. Since the retrieval procedures introduce unnecessary assumptions, variational assimilation techniques usually perform best with observational data closer to its original form.

In this paper, the limb sounding data are investigated in the context of the global analysis/forecast system at NCEP. In section 2, the observation data, basic principles and necessary tools are discussed. Then in section 3, model bending angles are simulated from the global analysis/forecast by means of a ray tracing technique and compared to the observations. Prior to and during the comparison, the ray tracing code was examined and modified to improve the efficiency and quality of the result when necessary. Next, two case studies involving super refraction are examined in section 4 showing a situation in which there exists a critical altitude below which the limb sounding technique can not be applied. Then in section 6, the observations are incorporated in the global analysis fields to examine the reliability of the data and the applicability of the ray tracing technique. Finally, section 6 presents conclusions and contains a discussion of the results.

2. Data and basic principles

2.1 Limb sounding data

The observational data set examined in this paper is from the level 3 version 4.25 processing at POCC[1]. In this data, an improved estimation of the contribution of the ionosphere to the excess phase delay has been introduced. In the results presented in this paper, data is used from 11 October, 1995. In Figure 2.1, the 138 profiles available worldwide for this day are shown. The arrow indicates the ray tangent vector at the occultation location.

Each profile consists of about 300 records for respective perigee points up to the altitude of 60km with 200m spacing. Figure 2.2 shows the cumulative number of observations for each vertical level. The height of the lowest perigee point for one particular profile depends upon both the atmospheric situation (especially moisture distribution) and the topography at the occultation location. It is apparent from Figure 2.2 that the number of observations decreases rapidly below 8km.

A bending angle and a impact parameter are reported at each perigee point together with the 3 dimensional location of the perigee point, observation time, and the normal vector of the perigee plane. The perigee plane is defined for individual trajectories by the 2 satellite locations and the Earth center. The trajectory is expected to be on the plane during the propagation. The impact parameter is characterized as a distance from the local curvature center of the occultation location to the line passing through one of two satellites (transmitter or receiver) and being parallel to the ray tangent vector at the satellite (see Figure 2.3). Under the assumption of spherical symmetry, the impact parameter is invariable for one trajectory and thus two impact parameters defined by the GPS and LEO respectively are to be identical each other;

$$p_a = xn\sin(\phi) \tag{2.1}$$

where p_a is the impact parameter, x the length of the vector to any point on a particular ray trajectory from the local curvature center, n the index of refraction and ϕ the angle between the x vector and the ray tangent vector at the point. The bending angle ε can be regarded as a univalued function of the

[1] <http://cosmic.cosmic.ucar.edu/gpsmet/>

impact parameter $\varepsilon(p_a)$.

2.2 Ray tracing method

Ray tracing is an essential tool to assimilate the raw limb sounding data directly into a numerical weather prediction system through a 3-dimensional variational data assimilation technique. It simulates the radio signal propagation from the GPS to the LEO and produces a bending angle from the model atmosphere which is comparable to the observations. The ray tracing code developed by the National Center for Atmospheric Research (NCAR) and the Florida State University (FSU) (Zou et.al. (1998a,b)) is used here. The tangent linear model and its adjoint are also provided with the ray tracing code. The distinctive feature of this ray tracing algorithm is that a simulated bending angle is interpolated to the observed height before comparison with the observed bending angle. This treatment can significantly reduce computational cost, since it is not necessary to calculate the exact ray to and from the actual satellite locations. The impact parameter is assumed to increase monotonically with respect to the height of the perigee point for each profile.

The Fermat principle for electromagnetic signal propagation gives the ray equation which governs the behavior of the ray trajectory under the influence of a refractivity field (Gorbunov and Sokolovskiy (1993)):

$$\frac{d^2\vec{\mathbf{x}}}{ds^2} = n\nabla n \tag{2.2}$$

$$ds = \frac{dl}{n} \tag{2.3}$$

where $\vec{\mathbf{x}}(s)$ is a vector originating at the Earth's center and directed to the GPS ray trajectory, l the length of the ray, and s the reduced distance.

The ray equation (2.2) can be decomposed into two first order equations;

$$\frac{d\vec{\mathbf{x}}}{ds} = \vec{\mathbf{v}} \tag{2.4}$$

$$\frac{d\vec{\mathbf{v}}}{ds} = n\nabla n . \tag{2.5}$$

where $\vec{\mathbf{v}}$ indicates the ray tangent vector at the position $\vec{\mathbf{x}}$.

Once initial values for $\vec{\mathbf{x}}$ and $\vec{\mathbf{v}}$ are given, (2.4) and (2.5) can be numerically solved for any given n.

The index of refraction n is derived from temperature (T), pressure (P) and water vapor partial pressure (Pw);

$$n = 1 + c_1 \frac{P}{T} + c_2 \frac{Pw}{T^2}, \tag{2.6}$$

where $c_1 = 77.6 \times 10^{-6}$ and $c_2 = 0.373$ K^2/hPa are constants (Bean and Dutton ,1966).

The Alternating Direction Implicit (ADI) method (Peaceman and Rachford, 1955, Zou et.al., 1998a,b) was chosen to numerically integrate the ray equation for its advantage in both accuracy and efficiency over the traditional Runge-Kutta method. The step size for the integration is set to 30km in the atmosphere below the altitude of 130km. It is assumed that the space above 130km is a vacuum and thus no refraction occurs above this level.

The horizontal gradient of the refractivity is neglected in (2.5). Only the vertical component is taken into account when a trajectory is traced. Note that the ray tracing procedure still accounts for horizontal variations in the vertical gradient.

Given ε_o, p_{ao}, $\vec{\mathbf{t}}_p$, $\vec{\mathbf{x}}_p$, $\vec{\mathbf{n}}_p$, $\vec{\mathbf{r}}_c$ and R_{gps}, the initial values $\vec{\mathbf{x}}_0$ and $\vec{\mathbf{v}}_0$ for the integration can be calculated with following equations;

$$\vec{\mathbf{v}}_{0a} = \vec{\mathbf{t}}_p + \frac{\vec{\mathbf{x}}_p}{|\vec{\mathbf{x}}_p|} \tan\left(\frac{\varepsilon_o}{2}\right) \tag{2.7}$$

$$\vec{\mathbf{v}}_0 = \frac{\vec{\mathbf{v}}_{0a}}{|\vec{\mathbf{v}}_{0a}|} \tag{2.8}$$

$$\vec{\mathbf{p}}_0 = \left\langle \vec{\mathbf{v}}_0, \vec{\mathbf{n}}_p \right\rangle \tag{2.9}$$

$$h = \left(\vec{\mathbf{r}}_c, \vec{\mathbf{p}}_0\right) + \sqrt{{p_{ao}}^2 - \left(\vec{\mathbf{r}}_c, \vec{\mathbf{n}}_p\right)^2} \tag{2.10}$$

$$\vec{\mathbf{x}}_0 = h \cdot \vec{\mathbf{p}}_0 - \sqrt{{R_{gps}}^2 - h^2} \cdot \vec{\mathbf{v}}_0 \tag{2.11}$$

where $\vec{\mathbf{x}}_0$ is the initial vector to the ray, $\vec{\mathbf{v}}_0$ the initial ray tangent vector, ε_o the observed bending angle, p_{ao} the observed impact parameter, $\vec{\mathbf{t}}_p$ the unit ray tangent vector at the perigee point, $\vec{\mathbf{x}}_p$ the vector to the perigee point from the Earth center, $\vec{\mathbf{n}}_p$ the unit normal vector of the perigee plane, $\vec{\mathbf{r}}_c$ the vector to the local curvature center at the occultation location and $R_{gps}\left(= 26000km\right)$ the given radius of the GPS orbit. $\left(\vec{\mathbf{a}}, \vec{\mathbf{b}}\right)$ indicates scalar product and $\left\langle \vec{\mathbf{a}}, \vec{\mathbf{b}} \right\rangle$ the vector product.

Figure 2.4 illustrates the relationship between the 3 vectors in equation (2.7). The initial ray tangent vector is expected to form an angle of $\varepsilon_o/2$ with the ray tangent vector at the perigee point. Figure 2.5 demonstrates the derivation of length h in equation (2.10). The diagram shows the plane normal to the initial ray tangent vector at the center of the Earth.. The point O refers the Earth center, D the local curvature center for the occultation location (projection onto the plane), CD corresponds to the observed impact parameter. The length of line CO is denoted by h. Figure 2.6 illustrates the relationship in equation (2.11) on the perigee plane (normal to the vector $\vec{\mathbf{n}}_p$), where 'A' is the location of GPS transmitter. BO corresponds to h in Figure 2.5.

Under the assumption of spherical symmetry, these initial conditions (2.7) - (2.11) are totally consistent with the geometric definition of the quantities recorded in the data set. However it can not be guaranteed that the point $\vec{\mathbf{x}}_0$ indicates the actual GPS satellite location nor that the $\vec{\mathbf{v}}_0$ represents the exact ray direction which would reach the LEO. Note that the exact solution for $\vec{\mathbf{x}}_0$ and $\vec{\mathbf{v}}_0$ is not required in this examination, since the simulated bending angle is interpolated to the observed height of perigee point as mentioned above.

A ray tracing procedure ends when the trajectory comes out from the atmosphere at 130km. The ray tangent vector at the terminal point $\vec{\mathbf{v}}_{end}$, together with the initial ray tangent vector $\vec{\mathbf{v}}_0$, gives the simulated bending angle ε_f .

$$\varepsilon_f = \arcsin\left(\left\langle \frac{\vec{\mathbf{v}}_0}{|\vec{\mathbf{v}}_0|}, \frac{\vec{\mathbf{v}}_{end}}{|\vec{\mathbf{v}}_{end}|} \right\rangle\right) \tag{2.12}$$

Using (2.1), the simulated impact parameter p_{af} is derived from the final vector $\vec{\mathbf{x}}_{end}$ and the ray tangent vector at that position $\vec{\mathbf{v}}_{end}$.

$$p_{af} = \left| \left\langle \vec{\mathbf{x}}_{end} - \vec{\mathbf{r}}_c, \frac{\vec{\mathbf{v}}_{end}}{|\vec{\mathbf{v}}_{end}|} \right\rangle \right| \tag{2.13}$$

Note that the final vector $\vec{\mathbf{x}}_{end}$ is subtracted from the vector to the local curvature center at the occultation event $\vec{\mathbf{r}}_c$ before deriving the impact parameter.

After performing ray tracings for all perigee points observed at one occultation event, a profile of the simulated bending angle with respect to the simulated impact parameter $\varepsilon_f\left(p_{af}\right)$ is obtained. Generally speaking, it is not guaranteed that the simulated impact parameter p_{af} for a perigee point realizes the same value as the observed one p_{ao} , though the initial impact parameter has been set to the observed value. In order to calculate the observational residual $\left(\Delta\varepsilon = \varepsilon_o - \varepsilon_f\right)$, a simulated bending angle at the observed impact parameter $\varepsilon_f\left(p_{ao}\right)$ is needed. For this purpose, the simulated bending angle at the simulated impact parameter $\varepsilon_f\left(p_{af}\right)$ is interpolated to the level of the observed impact parameter p_{ao} . A linear interpolation method is introduced here. This technique can be applied only when the impact parameter increases monotonically with respect to the height of the perigee point.

2.3. Background field and data assimilation method

The Spectral Statistical Interpolation (SSI) objective analysis system which is operational at NCEP is used for the analysis experiments in section 5 at reduced resolution (T62L28). The SSI analysis system, used in the operational assimilation system for the Global Spectral Model (GSM), is a 3-dimentional variational data assimilation (3D-VAR) technique (Parrish and Derber (1992)). The variational method provides a powerful tool to incorporate almost any type of observation. In most versions of 3D-VAR, the solution is sought iteratively so that the cost function, a measure of undesirable characteristics of the

analysis, takes its local minimum value. The cost function J and its gradient used in the SSI analysis system are given as follows;

$$J = \mathbf{x}^{\mathrm{T}}\mathbf{B}^{-1}\mathbf{x} + (L\mathbf{x}-\mathbf{y})^{\mathrm{T}}(\mathbf{F}+\mathbf{O})^{-1}(L\mathbf{x}-\mathbf{y}) + J_c \tag{2.14}$$

$$\nabla J = \mathbf{B}^{-1}\mathbf{x} + \mathbf{L}^{\mathrm{T}}(\mathbf{F}+\mathbf{O})^{-1}(L\mathbf{x}-\mathbf{y}) + \nabla J_c \tag{2.15}$$

where $\mathbf{x}$ is the vector of analysis variables, $\mathbf{y}$ the vector of observation quantities, L the operator describing the observation forward model, $\mathbf{L}$ the tangent linear operator model for L, $\mathbf{B}$ the forecast error covariance matrix, $\mathbf{O}$ the observational error covariance matrix, $\mathbf{F}$ the representativeness error covariance matrix and J_c is a constraint term which provides additional balance and physical limits to the analysis.

The minimization procedure is explained as follows. First the observation forward model (L) transforms the analysis variables $(\mathbf{x})$ to the observation space and simulates the same quantities as the observation $(L\mathbf{x})$. Next the observation $(\mathbf{y})$ is compared with the simulated quantity and the residual $(L\mathbf{x}-\mathbf{y})$ is projected back to the space of the analysis variables by making use of the adjoint of the tangent linear model of the observation forward model $(\mathbf{L}^{\mathrm{T}})$. The projected residual for all observations, together with the other penalty terms measuring departure from the background field $(\mathbf{B}^{-1}\mathbf{x})$ and the constraints (∇J_c), gives the gradient of the cost function. The error covariance matrices $\mathbf{B}$, $\mathbf{O}$ and $\mathbf{F}$ control weighting for the related terms respectively. Then the analysis variables are modified so that the cost function takes a smaller value than before using a non-linear optimization algorithm. This procedure is repeated until the local minimum is attained.

Since the model top boundary of the Global Spectral Model (GSM) is about 40 km $(\sigma = 0.0027)$, the monthly climatology of the COSPAR International Reference Atmosphere (CIRA) (Rees et. al. (1990)) is applied for describing the state above the model atmosphere up to 130 km.

3. Statistical characteristics of the limb sounding data and the model simulated bending angle

3.1 Properties of the observations

Figure 3.1 shows the mean bending angle profile for 138 observations. The vertical axis indicates the height of the perigee point. Roughly speaking the bending angle decreases exponentially with height because of the vertical distribution of the atmospheric refractivity. Therefore an exponential regression curve for the mean bending angle is introduced here in order to visualize the detailed structure of the observed bending angle. Hereafter this curve is referred as the standard or reference profile. The reference profile is described as

$$\varepsilon_r = \varepsilon_0 \exp\left(-\frac{z}{H}\right), \tag{3.1}$$

where z is height and ε_r is the reference profile of the bending angle. The constants are specified as ε_0 = 32.032 milli radian and H =6.579 km. The standard profile is used to normalize the bending angle profiles. This rescaling allows improved visualization of the results without any loss of generality.

Figure 3.2 shows the normalized bending angle $(\varepsilon/\varepsilon_r)$ and its standard deviation. Both the average and the standard deviation show relatively large values around 17 km of height in connection with the tropopause in tropics where the gradient of the index of refraction is relatively large. The standard deviation exceeds 15% at this level. It is 5-7% for the levels below 12 km. Since few observations are reported below 2km due to the complex distribution of the water vapor, those below this level are excluded from the statistics. In the lower stratosphere from 20 to 45 km the standard deviation is about 8-10%, gradually increasing with height in the upper stratosphere (above 45km) due to vertical oscillations in the observations. At the level of 60 km the standard deviation exceeds about 40%. A sample profile showing the vertical oscillations appears in Figure 3.3. These oscillations may be from errors in the processing of the data or may be real structures such as gravity waves.

3.2 Properties of the simulated bending angle

The analysis and the subsequent forecast of the global data assimilation system (using a 28 level 62 wave

triangular truncation version) at NCEP is introduced as independent data to compare with the observations. First, a 5 hour forecast from each analysis time (00,06,12,18 UTC, October 11, 1995) is produced with the results saved every hour. The hourly prognostic variables are used to obtain the atmospheric index of refraction. The model bending angles corresponding to the observation are then simulated by means of the ray tracing techniques. Time differences of 30 minutes or less between observed and simulated bending angles are ignored.

Figure 3.4 shows the zonal mean index of refraction and its departure from the global average for 12 UTC October 11, 1995. The index of refraction decreases exponentially with height. At the level of 17 km there is a maximum related to the tropical tropopause, while minima are in the two polar regions at this level. A similar situation appears near surface. The latitudinal dependence is relatively small between 5km and 7km.

The average of the simulated bending angle and its standard deviation corresponding to the actual observation are shown in Figure 3.5. One of the noticeable things here is that the standard deviation above 45 km does not increase as with the observations. Note that the CIRA climate is used in the upper stratosphere and that the vertical resolution of the GSM is coarse in the stratosphere. Therefore, the simulated bending angle does not contain any of the oscillations (real or otherwise) observed in the upper atmosphere (see Figure 3.3). On average, the simulated bending angle is slightly larger than observed one above 45km. This may indicate that the CIRA data contains a bias for this season. For the rest of levels, the average of the simulated bending angle and its standard deviation are quite similar to observed values.

The positioning error of the simulated perigee point against the observation was examined. The simulated perigee point is defined here as the lowest point on the simulated trajectory. The observed perigee point is compared with the simulated perigee point on the trajectory whose initial impact parameter is the same as the observed one. The positioning error is characterized by three components tangent to the ray, normal to the perigee plane and the vertical.

Figure 3.6 shows the tangent component of the mean positioning error over 138 profiles. The abscissa represents the distance along the Earth's surface. The thick solid line indicates the bias (simulated – observation). The thin dotted lines denote bias plus/minus standard deviation. Note that the step length of ray tracing is set to 30km. Since no interpolation is performed to search for the simulated perigee point, it is reasonable to consider that a standard deviation of about 15km results from a truncation error of ray

tracing. Compared with the step length of the ray tracing, the bias is small enough to be considered negligible at all vertical levels. The vertical oscillation, with a wavelength of 5km, could also be caused by the truncation error.

The vertical component of mean positioning error is displayed in Figure 3.7. Comparing with the vertical interval of observation (200m), both bias and standard deviation are small at all levels except near the surface. The larger errors below 6km could result from many different reasons including errors in the analysis/forecast moisture, the small sample, modeling errors and the super refraction effect discussed below.

The positioning error normal to the perigee plane is presented in Figure 3.8. The bias is only a few meters in the stratosphere and about -30 meters in the troposphere. The standard deviation is 30m to 100m in the stratosphere. The smallest value is found near 16km. Above that level it increases gradually with height .

3.3 Properties of the bending angle residual

The mean (observed - simulated) and standard deviation of the bending angle residual are shown in Figure 3.9. From the viewpoint of data assimilation, the residual in the observation space is to be projected back to the model variables space in order to obtain the gradient of the cost function. No significant bias is detected between 7km and 35 km, with a negative bias increasing with height above 35 km as mentioned in the previous subsection. Another negative bias is also seen in the lower troposphere below 5km where the number of observations is limited. It is possible that both the inappropriate description of the moisture in the model and limited observation availability cause the near surface bias. The standard deviation is about 2-3% and is almost constant between 7 km and 35 km. The standard deviation also increases gradually above 35km and below 7km in the same levels that the bias increases.

The standard deviation below 7km can be reduced by excluding three particular soundings. Figure 3.10 (a), (b), (c) display the bending angle profiles for the three soundings. Figure 3.11 shows the mean observational residual and the standard deviation, when the suspect soundings shown in Figure 3.10 are excluded. Note the large differences over thin layers near the surface. These soundings may contain super refraction as discussed in the next section in either the simulated or observed bending angles.

Figure 3.12 shows the vertical correlation of the residual. The residuals seem to be nearly independent

from each other below 23km. Some vertical correlation is seen between 23km and 45km, however it can probably be neglected. The residual shows more complicated correlation above 45km due to the oscillations in the vertical.

4 Boundary layer and super refraction

In this section, the effect of the boundary layer moisture on the radio signal propagation is demonstrated for two cases. In both cases, steep vertical gradients of moisture produce super refraction of the radio signal trajectory. The steep gradient of moisture relates closely to the existence of a thermal inversion at the top of the boundary layer. It is shown that super refraction makes it difficult to identify which simulated ray actually corresponds to the real observation. This means that even if the observation exists, it is exceedingly difficult to assimilate it into the numerical weather prediction model below a certain critical altitude.

Figure 4.1 shows a bending angle sequence simulated for one particular observation in the Southeastern Atlantic ((4-1) in Figure 2.1). The simulated rays are ten times as dense in the vertical as the observations with the interval between the starting point for the rays being about 20 m. The step size for integrating the ray equation is set to 10 km for this experiment. Though no observation exists below 2.8km for this case, the ray tracing is extended till the ray intercepts the Earth. It is found that ray B passes considerably closer to the earth than ray A.

Figure 4.2 illustrates the ray trajectories simulated for this occultation event. The projection of the trajectories on the occultation plane is shown. Radio signals enter from the upper left and exit to the right with the spherical distance on the Earth adopted as the horizontal axis. It is found that ray B travels a markedly different path from ray A in spite of the initial close trajectories. Note that all rays following B take similar trajectories to B. However, trajectories for these rays cross each other and thus bending angle decreases in reverse as the ray gets closer to the ground (see Figure 4.1).

Figure 4.3 shows the cross section of the forcing term $\left(-n\nabla n\right)$ from the ray equation (2.2) on the occultation plane. Note that the forcing term solely consists of its vertical component. When a ray passes through the area where the forcing term is large (small), the refraction of the ray is large (small). There is a large forcing area at 600m around the occultation event and a small forcing area exists about at 360m,

which forces the path for ray B.

Figure 4.4(a) shows the simulated vertical profile of index of refraction at the point. The thick mark along the vertical scale indicates the model layer heights. The forcing term is displayed in Figure 4.4(b). The large forcing of the ray is associated with the steep index of refraction gradient. The forcing term in equation (2.6) can be decomposed into three terms corresponding to the gradient of temperature, moisture and pressure:

$$n\nabla n = c_1 \frac{n}{T}\nabla P + c_2 \frac{n}{T^2}\nabla Pw - \frac{n(n-1)}{T}\nabla T. \tag{4.1}$$

The vertical profiles of temperature and moisture are plotted in Figure 4.4(c) and three constituents of the forcing term are shown in Figure 4.4(d). It is evident that the forcing term is dominated by the moisture gradient. The steep gradient of the moisture is associated with a thermal inversion layer.

The equation for the impact parameter at the perigee point (2.1) can be re-written in terms of refractivity:

$$p_a = xn = \mathrm{Re}\left(1+\frac{z}{\mathrm{Re}}\right)(1+N), \tag{4.2}$$

where $N = (n-1)$ and $x = (\mathrm{Re}+z)$. N is the refractivity (x 10^{-6}), Re the local curvature radius of the Earth at the point and z the height of perigee point. Since $\frac{zN}{\mathrm{Re}} << 1$, (4.2) may be approximated:

$$p_a \cong \mathrm{Re}+\mathrm{Re}\,N + z. \tag{4.3}$$

Rearranging terms results in;

$$z + \mathrm{Re}\,N = (p_a - \mathrm{Re}) = p_m, \tag{4.4}$$

where p_m is the relative impact parameter. When the relative impact parameter is constant in the vertical, the vertical gradient of refractivity can be shown from (4.4) to be;

$$\left(\frac{\partial N}{\partial z}\right)_{p_o} = -\frac{1}{\mathrm{Re}} \tag{4.5}$$

When the gradient of refractivity exceeds this value, more than one perigee point has the same impact parameter. Then the impact parameter is not a monotonic function with respect to the height of perigee point, and the bending angle is not a univalued function of impact parameter.

Since the forcing term of the ray equation (2.5) may be rewritten as

$$-n\nabla n = -(1+N)\nabla N \cong -(1+N)\frac{\partial N}{\partial z}, \tag{4.6}$$

the critical value of the forcing term can be estimated from (4.5) and (4.6) ;

$$(-n\nabla n)_{crtical} = \frac{1}{\mathrm{Re}}(1+N) \cong \frac{1}{\mathrm{Re}}. \tag{4.7}$$

Using a typical value for the radius of the earth (6.378×10^6) ;

$$(-n\nabla n)_{crtical} = 157 \times 10^{-9}\ (/\mathrm{m}). \tag{4.8}$$

As shown in Figure 4.4(b), the maximum value of the forcing term exceeds this critical value.

A second example ((4-2) in Figure 2.1) is presented in Figure 4.5 through Figure 4.8. In this case, the vertical gradient of the forcing term is so steep that a duct is formed 200m below the peak of the forcing term. One particular ray actually runs into the duct and is transmitted further away resulting in an extremely large bending angle for this level. Both the existence of a thermal inversion at the top of the boundary layer and the high water vapor concentration in the boundary layer force the strong refraction in this layer.

The geographical distribution for the maximum value of the forcing term below 4km is illustrated in Figure 4.9. The value is derived from the global analysis for 12UTC, October 11, 1995. Only values larger than 157×10^{-9} /m are displayed here. This figure gives an indication of how often super refraction areas occur. Most of the super refraction area is in tropics and sub-tropics between 33S and

33N of latitude. Over the continents values exceeding the critical value are usually close to shore. The super refraction area is most closely related to the existence of thermal inversions or stable layers and the subsequent concentration of water vapor near surface. The critical altitude for super refraction depends on the thickness of the moist boundary layer, which varies from 200m to 800m.

5. Analysis experiments

In this section, four analysis experiments are described which investigate the suitability of the ray tracing code and its adjoint and to estimate the impact of GPS/MET observations on the global analysis field. The analysis time is 12UTC, October 11, 1995. The observation data used here are thirty occultation data between 09UTC and 15UTC. The locations of the data are shown in Figure 5.1. The time difference of the observations from the analysis time is neglected.

The configuration of the experiments is presented in Table 5.1. A single GPS profile (No.15 in Figure 5.1) is analyzed into the operational analysis field in EXP 1. Thirty profiles of GPS bending angle are analyzed simultaneously in EXP 2. In EXP 3, conventional observation data are analyzed as well as GPS occultation data into a 6 hours forecast for the analysis time. As a control experiment, only the conventional data are analyzed in EXP4.

The observation error covariance matrix is required to analyze the observations. The error variance is estimated from the standard deviation profile presented at section 3.3 by fitting a series of piecewise linear functions (dotted line in Figure 3.9). Since the vertical observational error correlation is small and not well known (see section 3.3), the vertical correlation of the error is neglected.

Observation data above 46km is not assimilated, since these data are not expected to impact the analyses.

5.1 Single GPS profile

In this subsection, one GPS profile is assimilated into the operational analysis field (EXP 1). The profile selected here was collected at 12:13PM, closest to the analysis time in the data set. It is located at 56.5N and 81.9W in Hudson Bay. The background field for the analysis is the operational global analysis. Thus other observations at the analysis time have been assimilated into the background field.

Figure 5.2 shows the vertical profile of the bending angle observed and its corresponding simulated profile from the background field. Though the simulated one does not describe the fine structure of the observation because of the limited vertical resolution of the model, the model roughly shows good agreement.

The minimization procedure shows excellent convergence to the solution. The variation of the cost function during the minimization procedure is shown in Figure 5.3 with respect to the number of iterations. The norm of the gradient of the cost function is also indicated in Figure 5.4. The norm of the gradient decreases by a factor of more than 3000 after 11 iterations. This reduction satisfied the convergence requirements in the analysis system and the analysis procedure restarts the analysis procedure while relinearizing some components about the current solution. This relinearization is referred to as the second outer iteration. The 12th iteration in Figure 5.4 corresponds to the first iteration of the second outer iteration.

The analysis increment (the difference between the analysis and the background) for surface pressure is presented in Figure 5.5. The maximum increment is recognized at the occultation location. Most of North America is affected by the observation because of the large horizontal scale of the background error covariance.

Figure 5.6 shows the analysis increment of surface pressure along 56N from the date line to the Greenwich meridian. The maximum increment exceeds about -1.7hPa near the occultation location.

Figure 5.7 shows the analysis increment of temperature at sigma level 11 (~633hPa). This level chosen because it exhibits the maximum temperature increment in the troposphere. The analysis increment of temperature along 56N at the sigma level 11 is displayed in Figure 5.8. The maximum value of -1.4 K is reached near the occultation location. Figure 5.9 shows the vertical structure of the analysis increment of temperature at the occultation location. The ordinate indicates altitude in km. The thick mark along the ordinate corresponds to the model layer.

Figure 5.10 shows the analysis increment of specific humidity at the sigma level 10 (~694hPa) where the specific humidity increment is at its maximum (0.17 g/kg). Figure 5.11 is the analysis increment of specific humidity along 56N at the sigma level 10. Figure 5.12 shows the vertical structure of the analysis

increment of specific humidity at the occultation location. Significant moisture change has occurred only in the troposphere below the level of 8km.

Figure 5.13 shows the vertical profile of the normalized analysis increment of index of refraction. The increment is normalized by the index of refraction of the background field at each vertical level. The change above 5km primarily corresponds to that of temperature while the moisture profile affects strongly the index of refraction near surface below 5km.

Figure 5.14 is the vertical profile of the change of ray forcing term $(n\nabla n)$ during the analysis. Figure 5.15 is same as Figure 5.14 but for the three components of the forcing term (see equation (4.1)). Note that the pressure term depends upon the temperature, since the GSM is based on the hydrostatic approximation. Again it is evident that the change of the ray forcing term above 5km is most strongly related to the temperature increment and to the moisture effect below 5km.

Figure 5.16 shows simulated bending angle from the analysis field. The observation is superimposed as in Figure 5.2. The departure from the observation seen in Figure 5.2 has been reduced at most altitudes. The change of the simulated bending angle during the analysis is shown in Figure 5.17. As expected, close similarity between the change of bending angle and that of ray forcing term (see Figure 5.14) can be seen.

Figure 5.18 compares observational residuals of bending angle obtained from the background field and the analysis. The residual is reduced at almost all levels of height below 40km owing to the data analysis procedure. This reduction is of about the expected amplitude given the observational and background error variances.

5.2 Thirty GPS profiles

In this subsection, thirty GPS profiles between 09UTC and 15UTC are included into the analysis field (EXP 2).

The variation of cost function during the minimization procedure is shown in Figure 5.19 with respect to the number of iterations. The norm of gradient of the cost function is also indicated in Figure 5.20. The norm of the gradient decreases by a factor of more than 3000 after 21 iterations. Iterations after the 18th in Figure 5.20 corresponds to the second outer iteration.

The individual contributions to the cost function for each occultation data are displayed in Figure 5.21 for each observation. The open circles indicate the initial value (background field) of the penalty and the closed circles denote the value at the final state (analyzed field). This diagram indicates that the minimization procedure changes all profiles of model bending angles towards the observations.

Figure 5.22 shows the same as Figure 5.21 but with respect to the latitude of the occultation event. Open circles indicate initial value of the penalty and closed squares denote the value at the final state. Large penalty values of the penalty are found in the tropics at the initial state. Even at the final state, relatively large values remain in tropics. Generally speaking the amplitude of oscillations is relatively large in tropics. If real, the vertical resolution of the numerical model is too coarse to describe the fine structure (e.g., gravity waves) in the stratosphere. For this reason, the penalty terms retain large values at the final state of the minimization process.

The analysis increment of surface pressure is presented in Figure 5.23. Most local maxima and minima are found at or around the observation points assimilated (see Figure 5.1). The analysis increment pattern contains a clear zonal structure. Figure 5.24 shows the zonal mean analysis increment of surface pressure. Negative bias can be seen in tropics and positive bias in high latitude area. The differences exceed more than 2.5 hPa or 0.25% of mean surface pressure between polar regions and the tropics. It is difficult to justify such a large systematic mass transfer in the analysis.

The analysis increment of total precipitable water is shown in Figure 5.25. Since the horizontal scale in the background error covariances is smaller than the temperature fields, the increments are even more localized around the observation points.

Figure 5.26 displays the zonal mean analysis increment of temperature. Larger increments are found in upper stratosphere in the polar region, though no observations exists in this area. Cooling is dominant in tropics. It is thought that this feature relates to the systematic bias on the analysis increment of surface pressure mentioned above. In terms of vertical levels, cooling appears at the levels of about 800hPa, 200hPa and 80hPa and warming can be found around 400hPa and 100hPa.

The amplitude of zonal mean surface pressure bias (0.25%) is as same order as those of the ellipticity of the Earth (0.3%) and the latitudinal variation of the acceleration of gravity(0.5%). Note that both the

ellipticity and the gravity variation have been taken into account in the observation forward model in this study when the geopotential heights of the background field are converted into the geodesic height and vice versa. An additional experiment (EXP 2A) corresponding to EXP 2 is performed in order to examine the impact of the gravity variance. In this experiment the acceleration of gravity is set to a constant value $9.80665 m/s^2$. Other conditions of the experiment are identical with those of EXP 2. The analysis increment of surface pressure is displayed in Figure 5.27. The zonal mean analysis increment of surface pressure is presented in Figure 5.28. The zonal mean analysis increment of temperature is also shown in Figure 5.29. It is clear that the systematic bias of surface pressure increment almost disappears. The cooling bias in tropics is also mitigated. In principle, inclusion of the variation in gravity is reasonable and desirable. However, the result shown here indicates that including this variation for only one type of data produces inconsistencies in the assimilation system.

5.3 Thirty GPS profiles and conventional data

In addition to the thirty occultation data introduced in the previous subsection, all other available conventional data such as rawinsondes and aviation reports are assimilated simultaneously into a 6 hours forecast for the analysis time (EXP 3). Note that radiance data are excluded from this experiment. The cost function in this experiment includes the penalty term for limiting humidity, which forces moisture not to be negative nor super saturated. It is reasonable and preferable to introduce this kind of penalty, but it is known that the minimization process needs more iterations for convergence because of the step-function-like behavior of this term.

In order to examine the impact of the GPS limb sounding data, the control experiment is carried out as EXP 4, in which no occultation data are assimilated. All other conditions for EXP 4 are as same as those for EXP 3.

The variations of cost function for EXP 3 and EXP 4 are shown in Figure 5.30 with respect to the number of iterations. The norms of gradient are also indicated in Figure 5.31. The minimization process ends at the 161st iteration step in EXP 3 and 157th in EXP 4 respectively, since the norm of the gradient decreases by a factor of more than 3000. Iterations after the 100th in Figure 5.31 corresponds to the second outer iteration.

The difference of the analysis of surface pressure between EXP 3 and EXP 4 is presented in Figure 5.32.

Compared with the result of EXP 2 (see Figure 5.23), the impact of the occultation data on the analyzed field is small and less than 0.5hPa. Figure 5.33 shows the zonal mean difference of surface pressure between EXP 3 and EXP 4. Though the amplitude is smaller than that of EXP 2 (see Figure 5.24), the systematic zonal structure is still detectable in EXP 3.

The difference of the analysis of total precipitable water between EXP 3 and EXP 4 is shown in Figure 5.34. The impact of the occultation data on the analyzed field in EXP 3 is as same as that in EXP 2. Since the horizontal scale of the forecast error covariance for moisture field is relatively small, the effect of an observation is localized around the observation point and one datum rarely affects another in data sparse areas.

Figure 5.35 displays the zonal mean difference of temperature between EXP 3 and EXP 4. The impact of the GPS in EXP 3 is smaller than in EXP 2.

An additional experiment (EXP 3A) in which the acceleration of gravity is set to a constant as in EXP 2A is also performed. Other conditions of the experiment are identical with those of EXP 3. The difference of surface pressure between EXP 3A and EXP 4 is displayed in Figure 5.36. The zonal mean difference of surface pressure is presented in Figure 5.37. The zonal mean difference of temperature is also shown in Figure 5.38. As shown in EXP 2A it is clear that both the systematic bias of surface pressure and the cooling bias in tropics are mitigated.

6. Summary and conclusions

The GPS limb sounding data has been examined in order to begin assessment of its potential use in a state-of-the-art global data assimilation system.

The observed bending angle has been compared with that obtained by a ray tracing technique from the operational analysis/forecast at NCEP. Though the simulated bending angle does not describe the fine structures in the stratosphere due to the lack of the vertical resolution, it shows good agreement with the observation between 7km and 35km. The observational residual has no significant bias between these levels.

Next two case studies of super refraction were presented. It is found that the limb sounding technique can

be applied only above a certain critical altitude (200m-800m) when a thermal inversion is formed near the surface in the moist areas. The result suggests that there is a need for real-time quality control of the limb sounding data by excluding data in this region. The existence of the critical altitude can be diagnosed in the background field for each sounding. The actual observation below the critical altitude should be excluded from the assimilation and the data near the altitude have to be given a large error variance. The major quality control problem is when the observations contain super refraction and the background does not.

Four analysis experiments were performed for the active limb sounding data. In EXP 1, one specific profile was included in the analysis. The analysis variables were changed within an acceptable range and the observational residual of bending angle was reduced reasonably during the minimization process.

In EXP 2, thirty limb sounding profiles were assimilated simultaneously. The SSI and the ray tracing scheme again produces satisfactory results. However, it was noted that the analysis increment of surface pressure field contained a systematic zonal structure. It was found that the surface pressure bias was related to the latitudinal variance of the acceleration of gravity. The bias occurred when the variance of gravity is taken into account for the GPS limb sounding observation forward model and not in the rest of the assimilation system. Including the variance of gravity into only one type of data caused inconsistencies within the data assimilation system. The result indicated that the data assimilation system should have incorporated the latitudinal variance of the acceleration of gravity from end to end. However, until this happens, the GPS limb soundings should be processed without the latitudinal variation in gravity.

A comprehensive assimilation test was carried out as EXP 3 in concert with other conventional observational data to examine the stability of the non-linear optimization procedure. In terms of the norm of the gradient the experiment shows similar convergence as the control run (EXP 4). The impact of the GPS occultation data is smaller than the exclusive run EXP 2.

Further studies are required on several aspects. First, a data assimilation cycle including the GPS occultation data is desirable for a reasonably long period. The comparison of the resulting analysis and forecast with conventional data can indicate the reliability and impact of the GPS limb sounding data.

Though significant improvement on cost performance is achieved here for the ray tracing algorithm, the

forward model still costs 0.439 seconds per profile of CPU time on the cray C90 at NCEP for one profile and the adjoint code requires 0.796 seconds. For one step of the minimization, the forward model is executed once for simulating model bending angle and another 6 times due to step-size estimation for the non-linear optimization algorithm and the adjoint model once for obtaining the gradient of the cost function. As for the POCC data there are more than 30 occultation events in the time window of 6 hours for the analysis. Thus 200 iterations requires more than 6 hours of CPU time. In the near future, many more soundings will be available. Therefore, improving cost performance at least several orders of magnitude is essential for operational use.

The observation forward model can be simplified under the assumption of spherical symmetry. Eyre (1994) proposed a simple forward model to simulate bending angle, in which (2.1) is directly integrated to obtain bending angles and the refractivity profile at the occultation location is solely used. Asymmetry can be taken into account by adding a correction term.

An observation forward model should be formulated to meet the operational requirement for computational efficiency as well as accuracy.

Acknowledgment

The authors are grateful to Russ Treadon, and Wan-Shu Wu (NCEP/EMC) for discussing the results and for giving useful comments on this article. The author is grateful to Simon Rosenfeld (NESDIS) for his help and excellent comments. This work was partially supported by Integrated Program Office of NOAA National Polar-orbiting Operational Environmental Satellite System. This work was made possible by a collaborative project on data assimilation between the National Centers for Environmental Prediction and the Japan Meteorological Agency.

References

Bean, B. R. and E. J. Dutton 1966: Radio Meteorology, National Bureau of Standards Monograph 92, Boulder CO. USA.

Derber J. C. and W.-S. Wu 1998: The use of TOVS cloud-cleared radiances in the NCEP SSI analysis system. Mon. Wea. Rev., 126, 2287-2299.

Eyre, J. R. 1994: Assimilation of radio occultation measurements into a numerical weather prediction system. Research Department Technical Memorandum No.199, European Centre for Medium-Range Weather Forecasts, Reading UK.

Eyre, J. R. and D. Offiler 1998: Radio occultation measurements in operational meteorology. Forecasting Research Technical Report No. 246, UK Met. Office Bracknell UK.

Gorbunov, M. E. and S. V. Sokolovskiy 1993: Remote sensing of refractivity from space for global observations of atmospheric parameters; Max-Planck-Institut Fuer Meteorology Report No. 119.

Kuo, Y.-H., X. Zou, S. J. Chen, W. Huang, Y.-R. Guo, R. A. Anthes, M. Exner, D. Hunt, C. Rocken and S. Sokolovskiy 1998 : A GPS/MET sounding through an intense upper-level front. Bull. Amer. Meteor. Soc., 79, 617-626.

Kursinski, E. R., G. A. Haji, J. T. Schofield, R. P. Linfield and K. R. Hardy 1997: Observing Earth's atmosphere with radio occultation measurements using the Global Positioning System. J. Geophys. Res., 102(D19), 23429-23465.

Leroy, S. S. 1997: Measurement of geopotential heights by GPS radio occultation. J. Geophys. Res., 102(D6), 6971-6986.

McNally, A. P., J. C. Derber, W.-S. Wu and B.B. Katz, 1999: The use of TOVS level-1B radiances in the NCEP SSI analysis system. Submitted to Q. J. Roy. Meteor. Soc.

Parrish, D. F. and J. C. Derber 1992: The National Meteorological Center's Spectral Statistical-

Interpolation analysis system. Mon. Wea. Rev., 120, 1747-1763.

Peaceman, D. W. and H. H. Rachford, Jr. 1955: The numerical solution of parabolic and elliptic differential equations. J. Soc. Indust. Appl. Math., 3, 28-41.

Rees, D., J. J. Barnett and K. Labitzke 1990: COSPAR International Reference Atmosphere Part II: Middle Atmosphere Models. Adv. in Space Res., 10, No. 12, 517.

Rocken, C., R. Anthes, M. Exner, D. Hunt, S. Sokolovskiy, R. Ware, M. Gorbunov, W. Schreiner, D. Feng, B. Herman, Y.-H. Kuo and X. Zou 1997: Analysis and validation of GPS/MET data in the neutral atmosphere. J. Geophys. Res., 102(D25), 29849-29866.

Ware, R., M. Exner, D. Feng, M. Gorbunov, K. Hardy, B. Herman, Y. Kuo, T. Meehan, W. Melbourne, C. Rocken, W. Schreiner, S. Sokolovskiy, F. Solheim, X. Zou, R. Anthes, S. Businger and K. Trenberth, 1996: GPS sounding of the atmosphere from Low Earth Orbit: Preliminary results. Bull. Amer. Meteor. Soc., 77, 19-40.

Zou, X., F. Vandenberghe, B. Wang, M. E. Gorbunov, Y. H. Kuo, S. Sokolovskiy, J.C. Chang and J. G. Sela 1998: Direct assimilation of GPS/MET refraction angle measurements Part I: Concept and results of ray tracing. Submitted to J. Geophys. Res..

Zou, X., B. Wang, F. Vandenberghe, M. E. Gorbunov, Y. H. Kuo, S. Sokolovskiy, J.C. Chang and J. G. Sela 1998: Direct assimilation of GPS/MET refraction angle measurements Part II: Variational assimilation using adjoint techniques. Submitted to J. Geophys. Res..

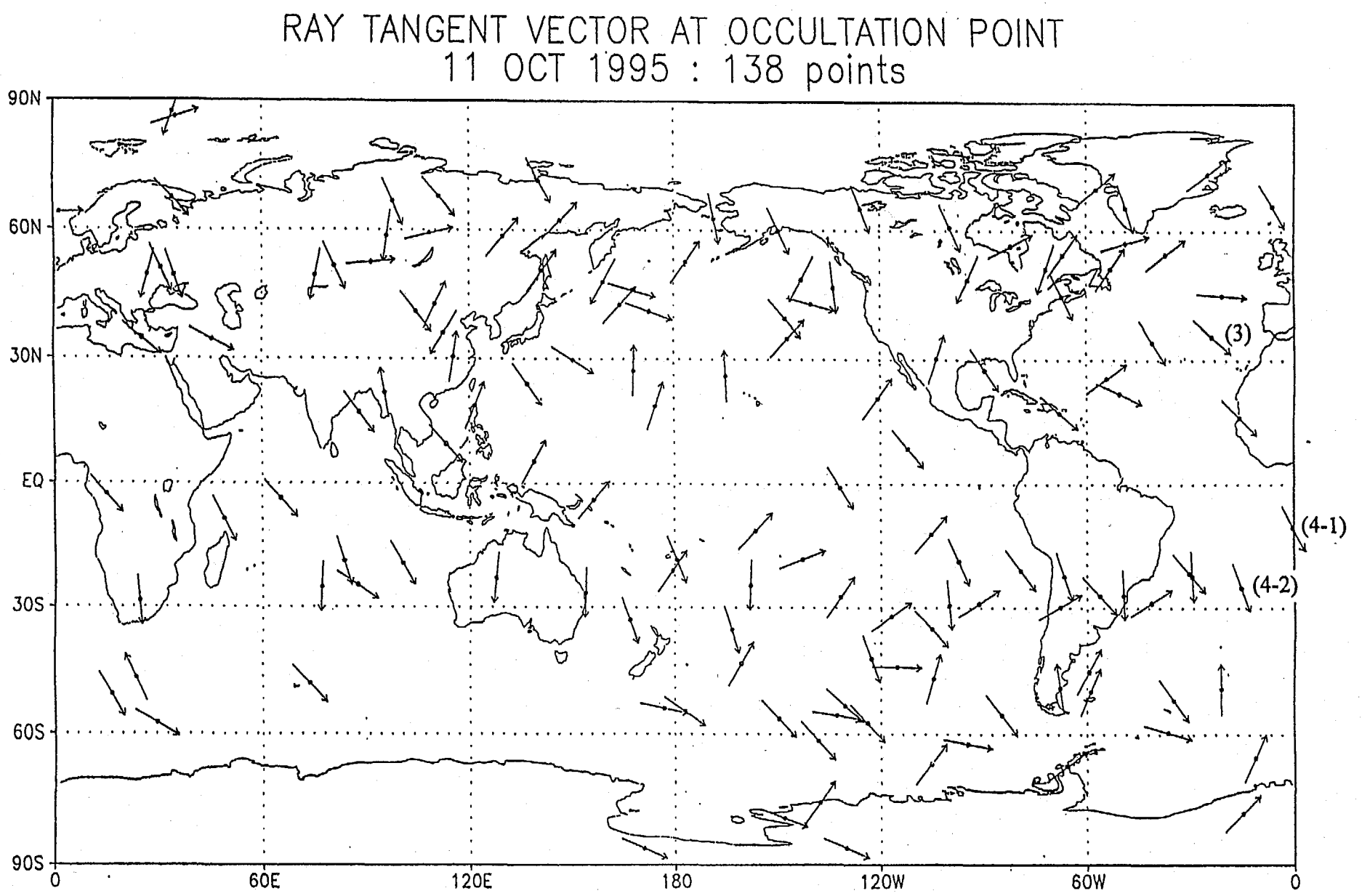

Fig. 2.1 : Geographical distribution of the 138 GPS limb soundings reported on October 11, 1995. The arrow indicates the ray tangent vector for the occultation. (3) indicates the sample profile shown in Fig. 3.3. (4-1) and (4-2) are the observations presented in section 4.

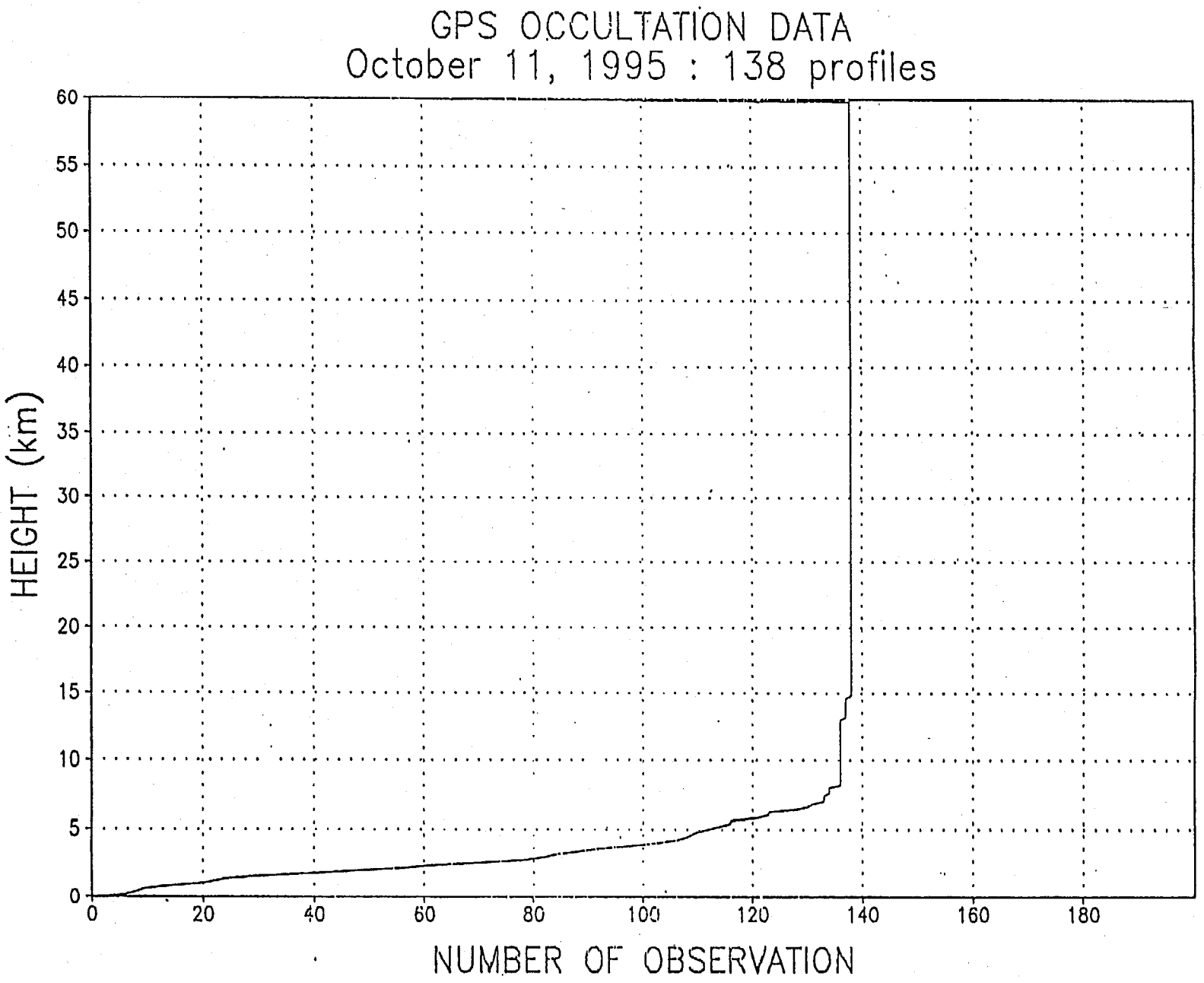

Fig. 2.2 : The number of observations for each vertical level. The maximum number is 138. The ordinate indicates the altitude of the perigee point.

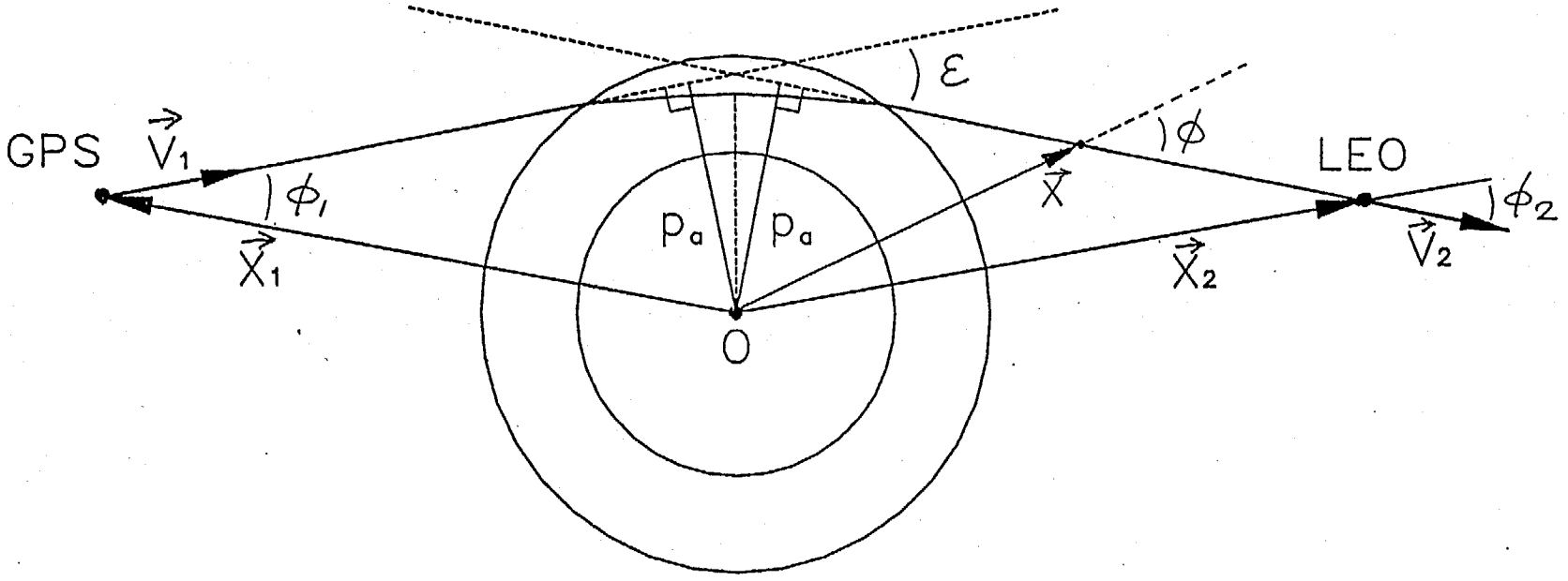

Fig. 2.3 : Geometry of the radio occultation measurement, where ε is bending angle, p_a impact parameter, $\vec{\mathbf{x}}$ the vector to the ray from the local curvature center, $\vec{\mathbf{v}}$ ray tangent vector and ϕ the angle between the $\vec{\mathbf{x}}$ vector and the ray tangent vector. Subscripts 1 and 2 indicate GPS and LEO respectively.

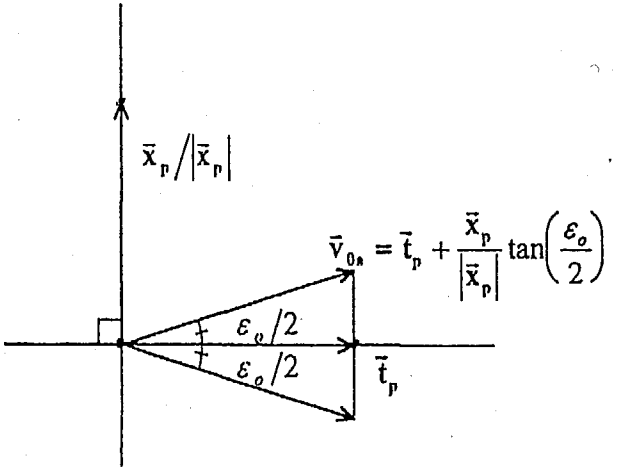

Fig. 2.4 : Relationship among 3 vectors in equation (2.7) on the perigee plane. $\vec{v}_{0a}$ the initial ray tangent vector, $\vec{t}_p$ the unit ray tangent vector at the perigee point, $\vec{x}_p$ the vector to the perigee point from the Earth center, ε_o the observed bending angle. $\vec{v}_{0a}$ is expected to form an angle of $\varepsilon/2$ with $\vec{t}_p$.

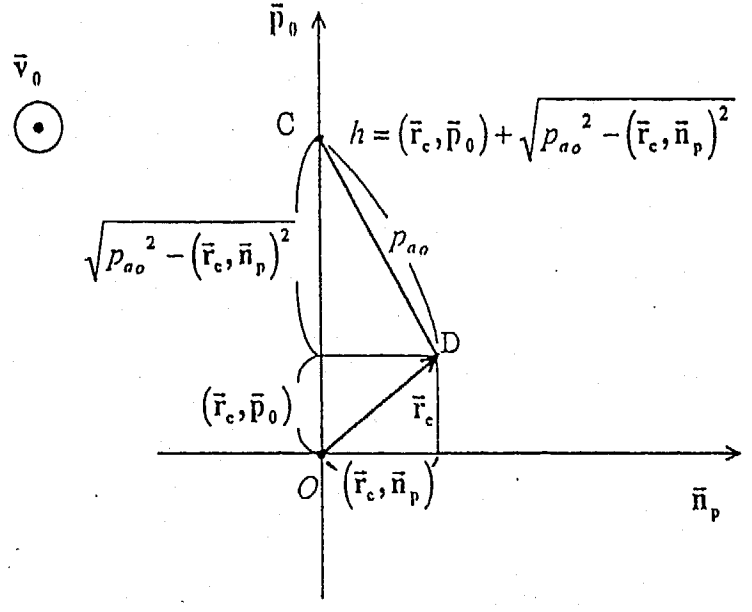

Fig. 2.5 : Explanation for the length h in equation (2.10). The plane normal to the initial ray tangent vector at the center of the Earth is illustrated. The point O refers the center of the Earth, D the local curvature center for the occultation (projection onto the plane), CD corresponds to the observed impact parameter. h is the length of line CO.

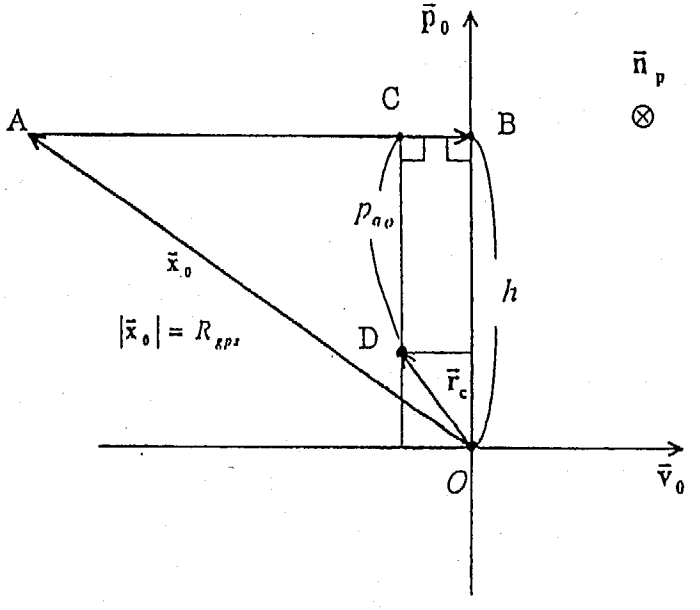

Fig. 2.6 : Explanation for equation (2.11) on the perigee plane (normal to the vector $\vec{n}_p$). O is the center of the Earth, 'A' is the location of GPS transmitter to be detected, D the local curvature center for the occultation (projection onto the plane). BO corresponds to h in Fig. 2.5.

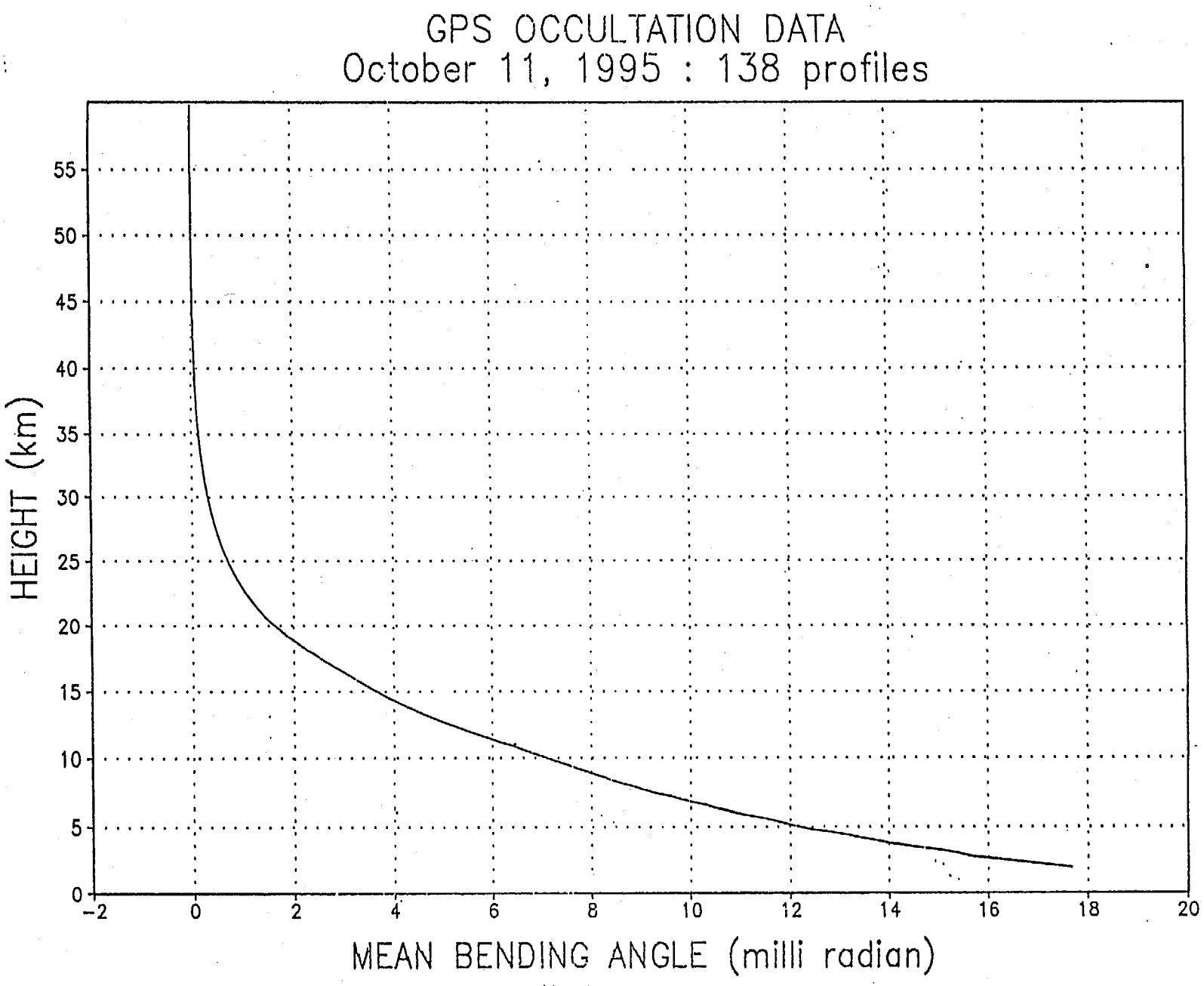

Fig. 3.1 : Mean bending angle profile for 138 observations on October 11, 1995. The ordinate indicates the altitude of perigee point.

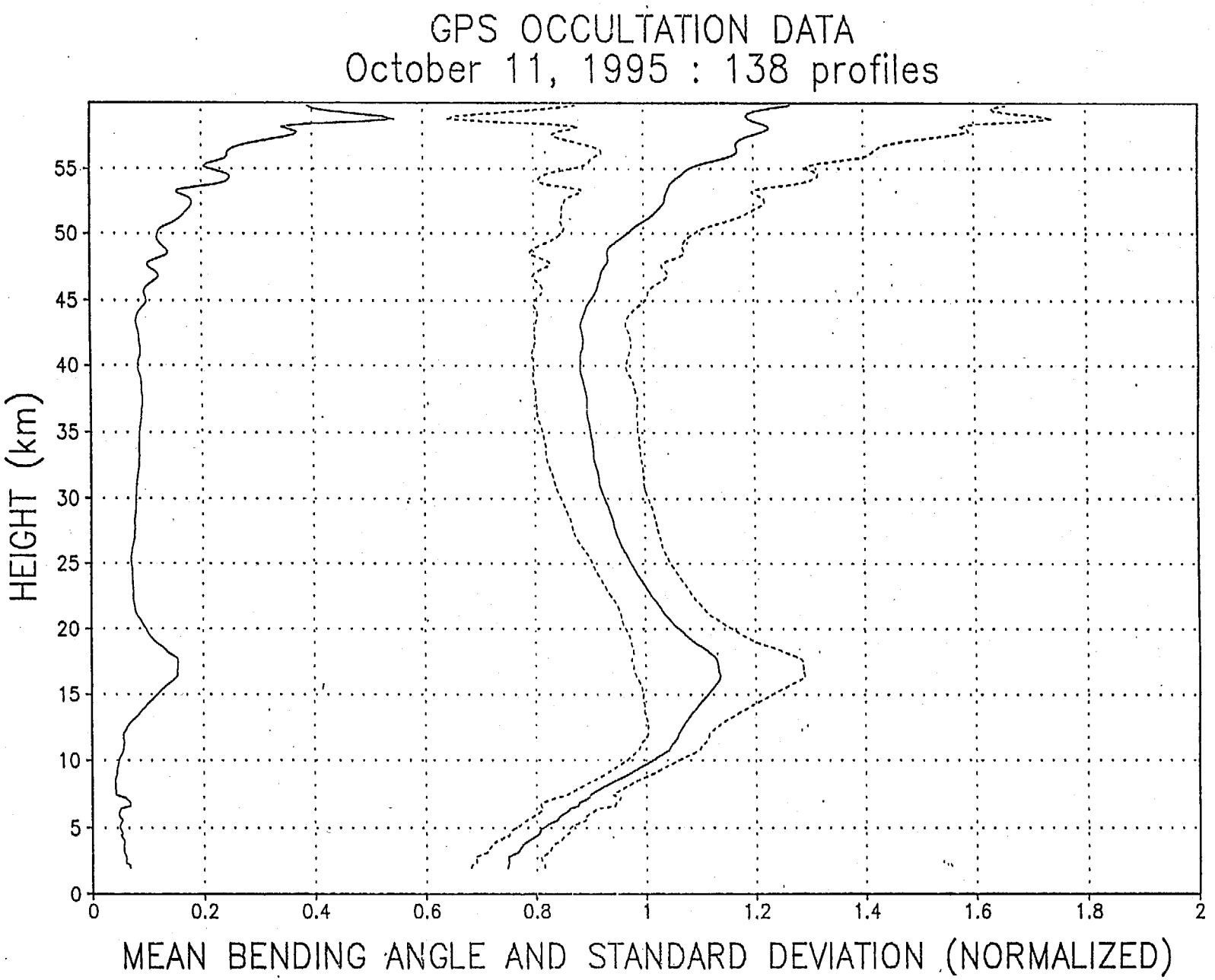

Fig. 3.2 : Normalized mean bending angle of the observation and its standard deviation. The ordinate indicates the altitude of perigee point. Thick solid line is the average $\left(\overline{\varepsilon_o}/\varepsilon_r\right)$. Thin solid line (left) is the standard deviation $\left(\sigma_o/\varepsilon_r\right)$. Thin dashed lines denote the average plus/minus the standard deviation $\left(\left(\overline{\varepsilon_o} \pm \sigma_o\right)/\varepsilon_r\right)$. ε_r is the reference profile of the bending angle.

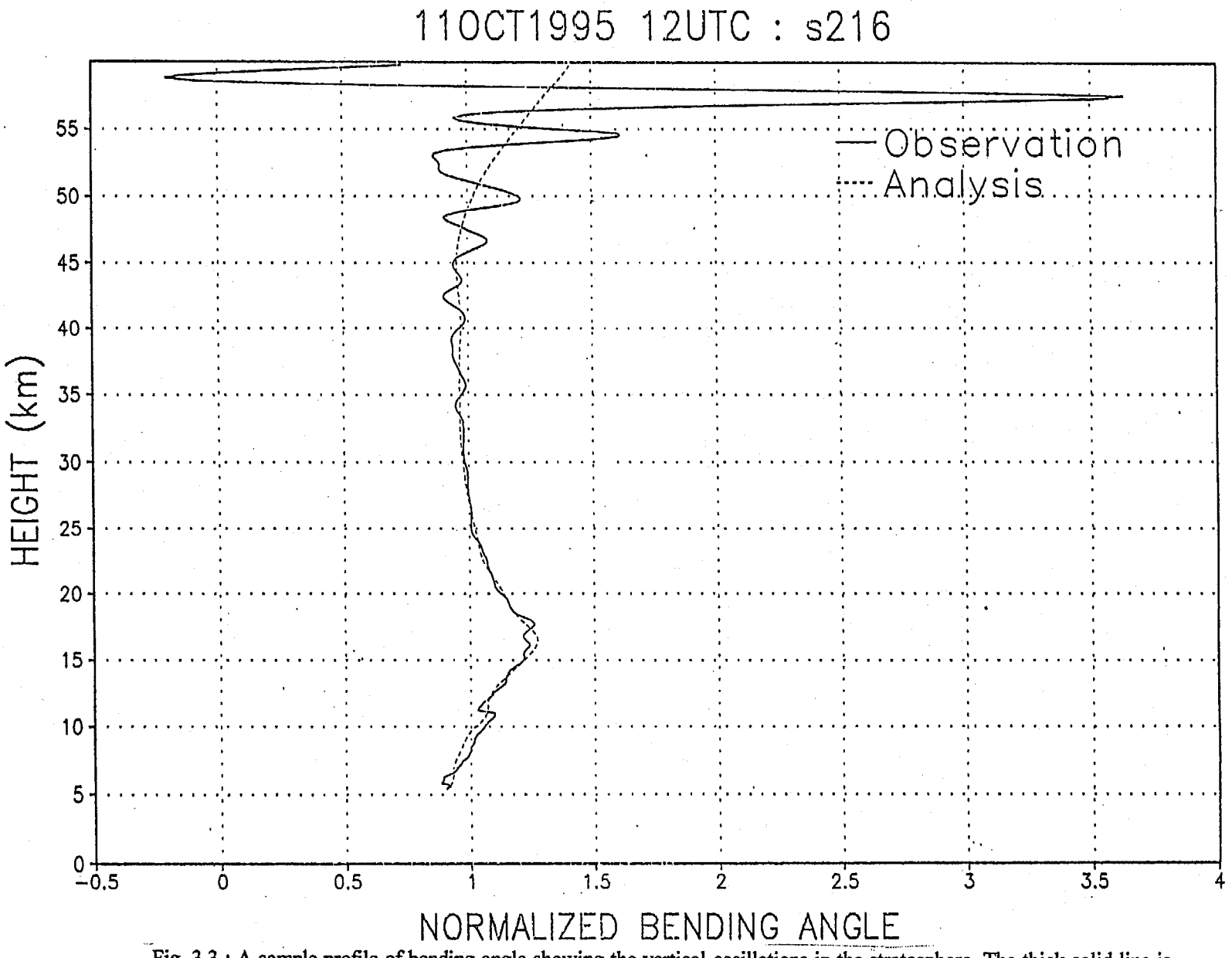

Fig. 3.3 : A sample profile of bending angle showing the vertical oscillations in the stratosphere. The thick solid line is the observed profile $(\varepsilon_o/\varepsilon_r)$. The thin dashed line is the simulated profile from the global analysis filed $(\varepsilon_f/\varepsilon_r)$. ε_r is the reference profile of the bending angle. The observation is from 12:27, October 11,1995 and located at 35.509N, 23.737W ((3) in Fig.2.1).

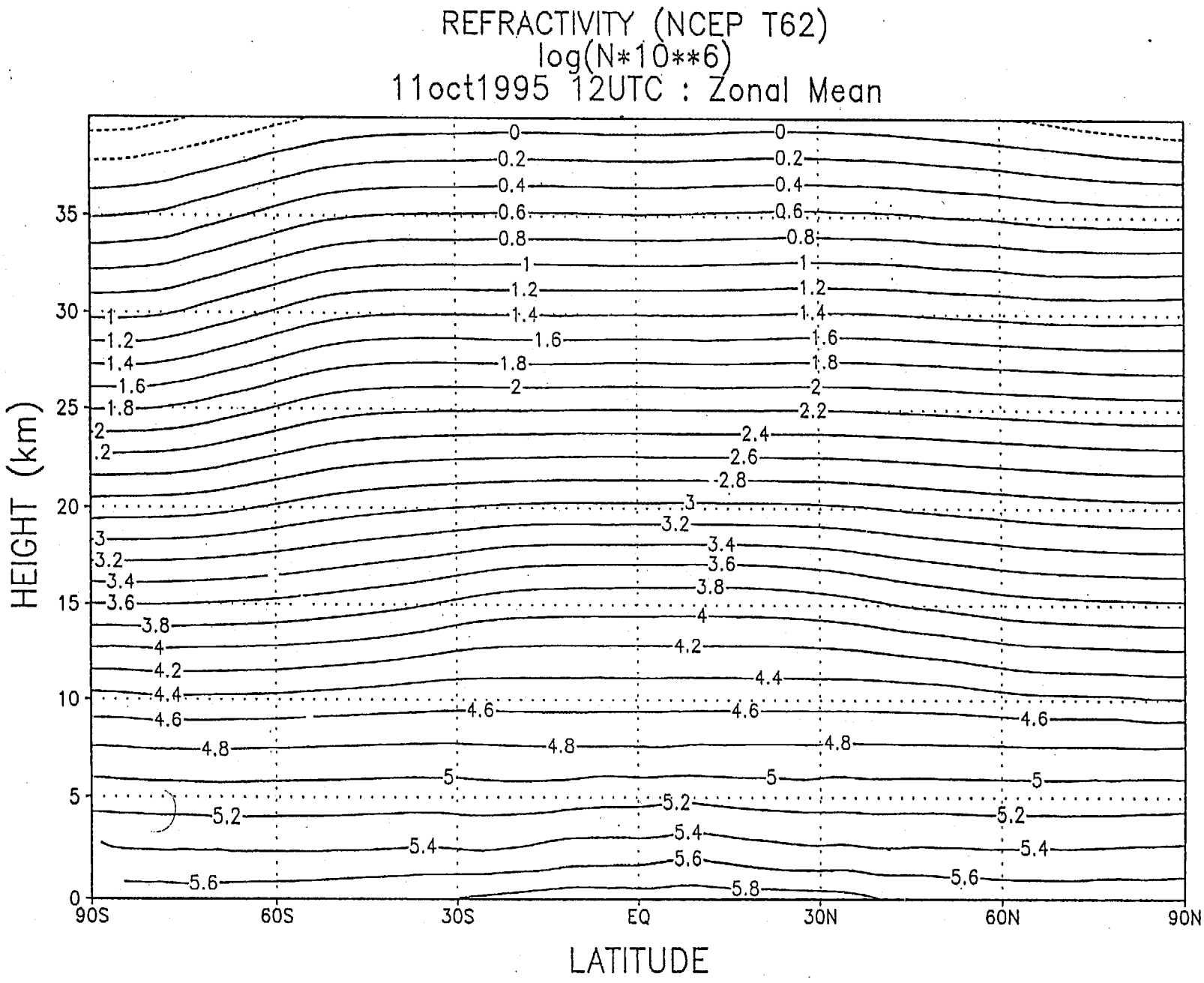

Fig. 3.4 (a) : Zonal mean index of refraction derived from the global analysis for 12 UTC, October 11, 1995. $\log\left((n-1)\times 10^{6}\right)$ is shown, where n is zonal mean index of refraction.

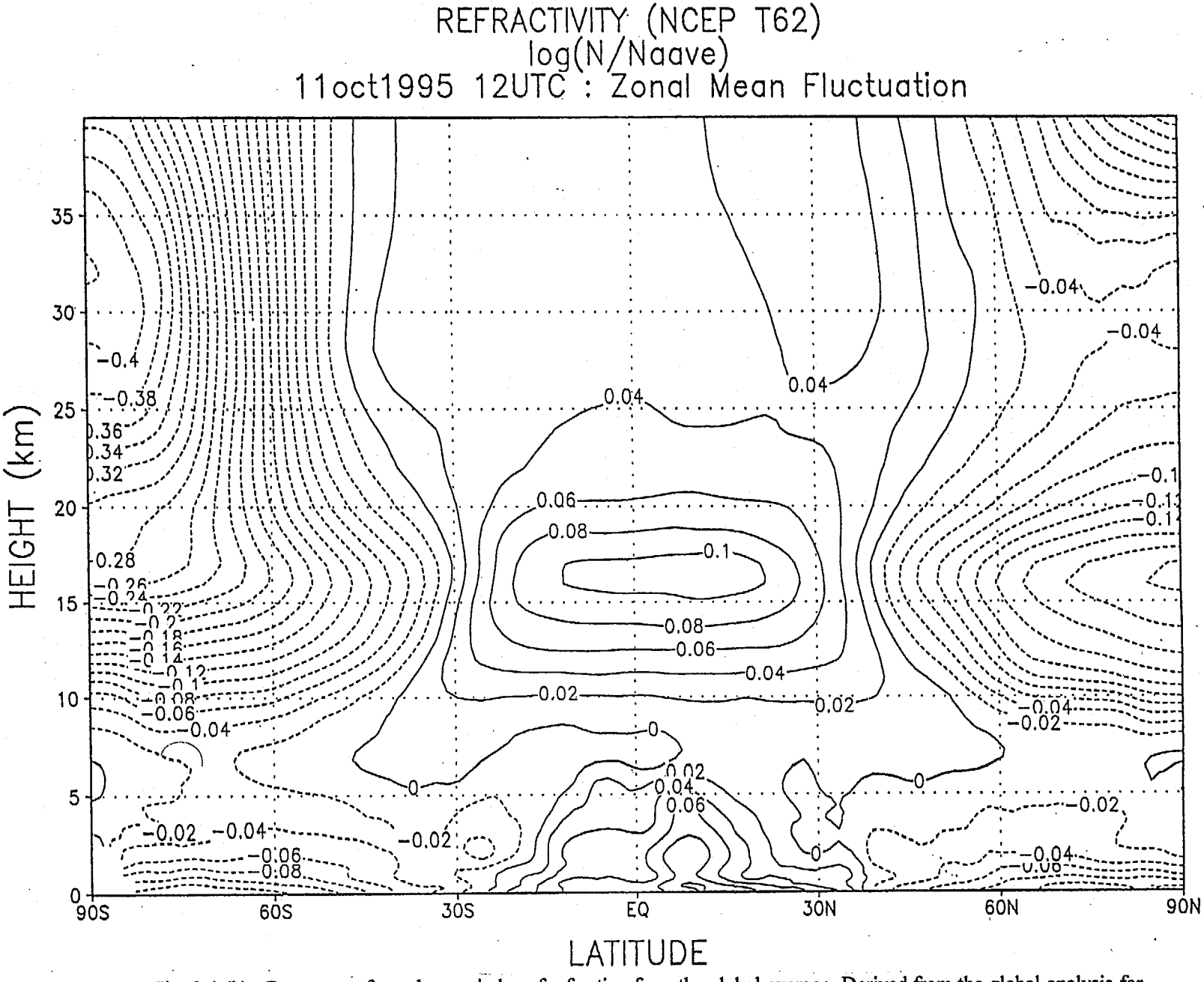

Fig. 3.4 (b) : Departure of zonal mean index of refraction from the global average. Derived from the global analysis for 12 UTC, October 11, 1995. $\log\left((n-1)/(n_{ave}-1)\right)$ is shown, where n is zonal mean index of refraction and n_{ave} is the global average of the index of refraction.

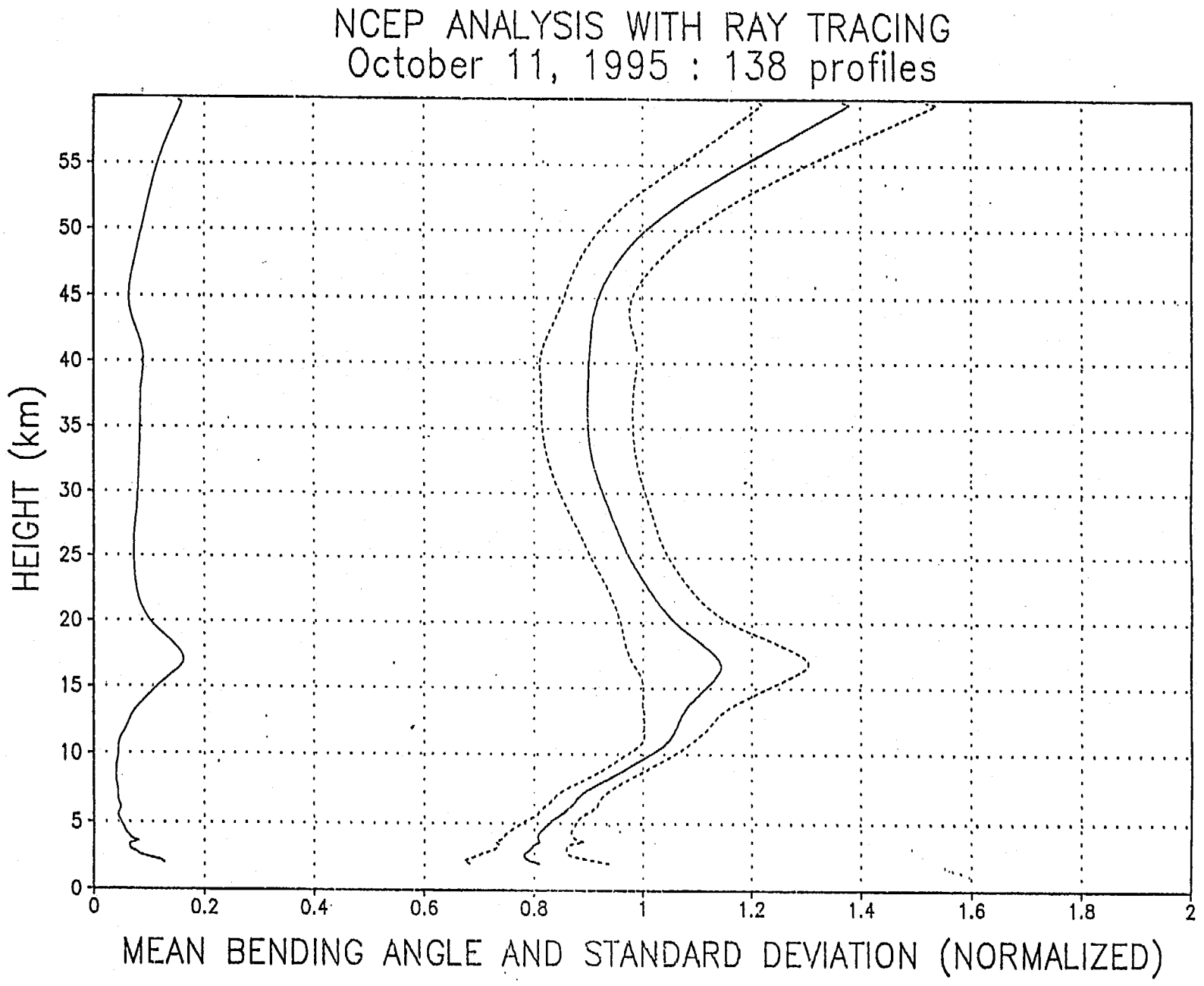

Fig. 3.5 : Same as Fig. 3.2 but for the simulated bending angle corresponding to the actual observation.

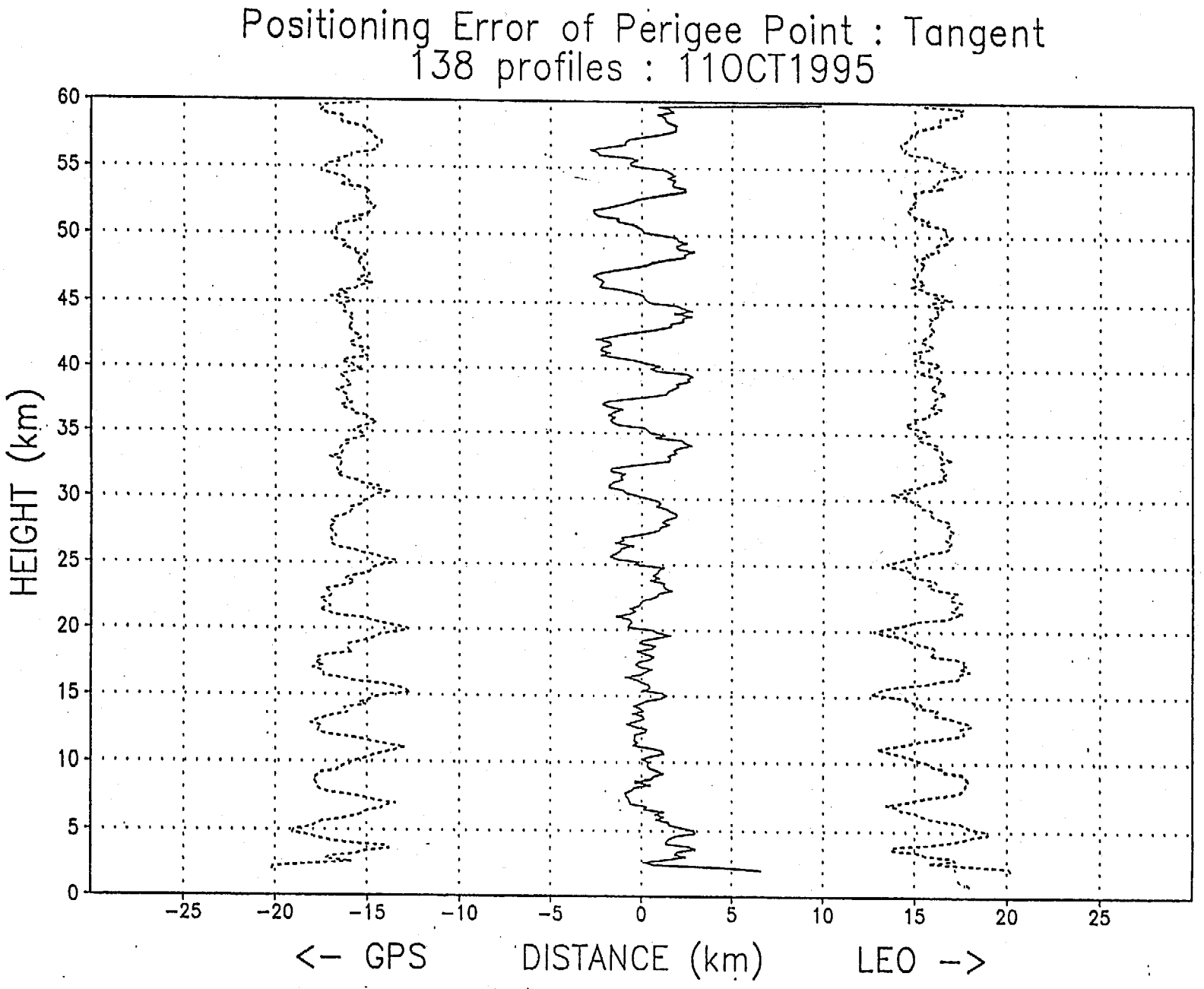

Fig. 3.6 : Tangent component of mean positioning error over 138 profiles. Thick solid line indicates bias of the error. Thin dotted lines denote bias plus/minus standard deviation.

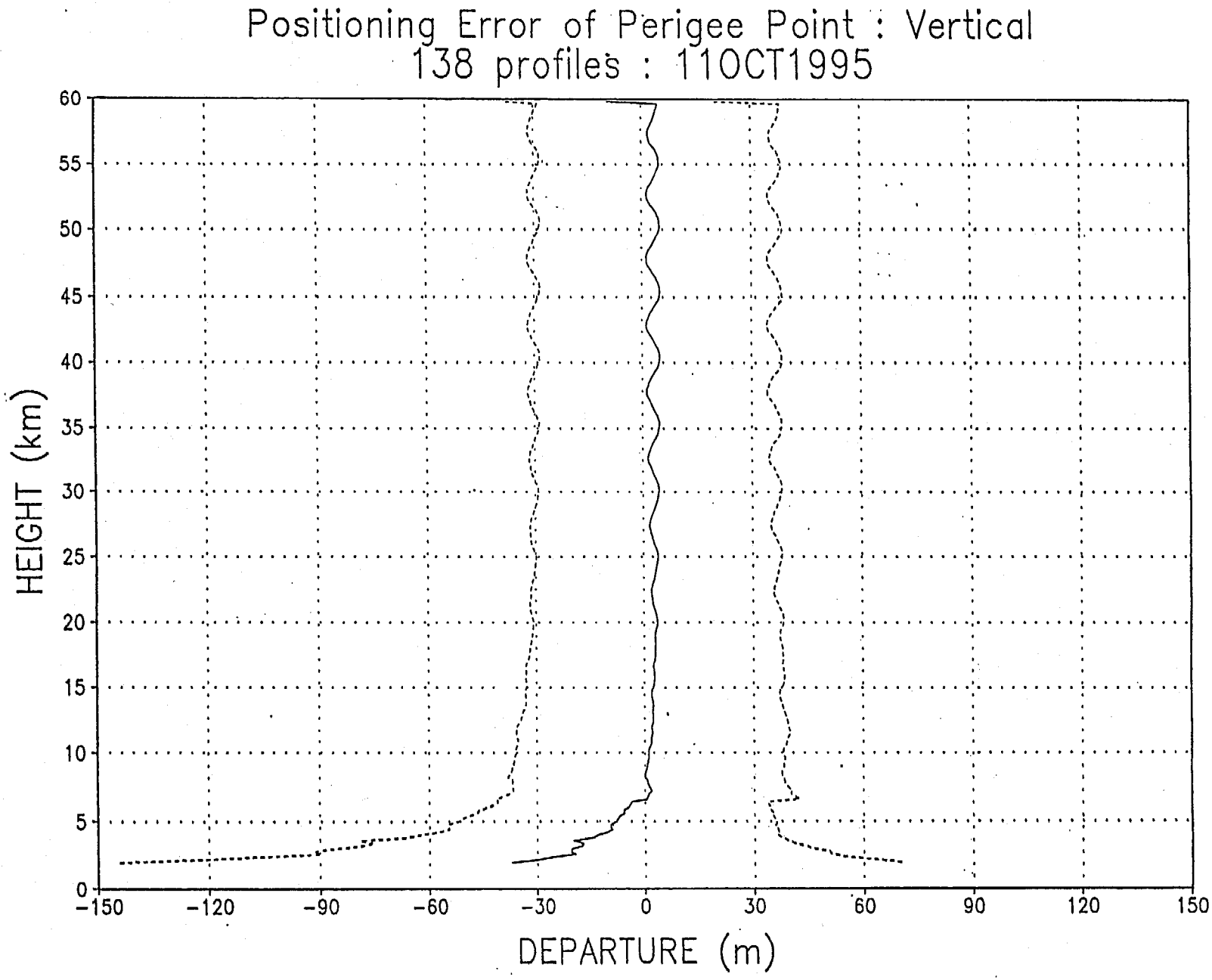

Fig. 3.7 :Same as Fig. 3.6 except vertical component.

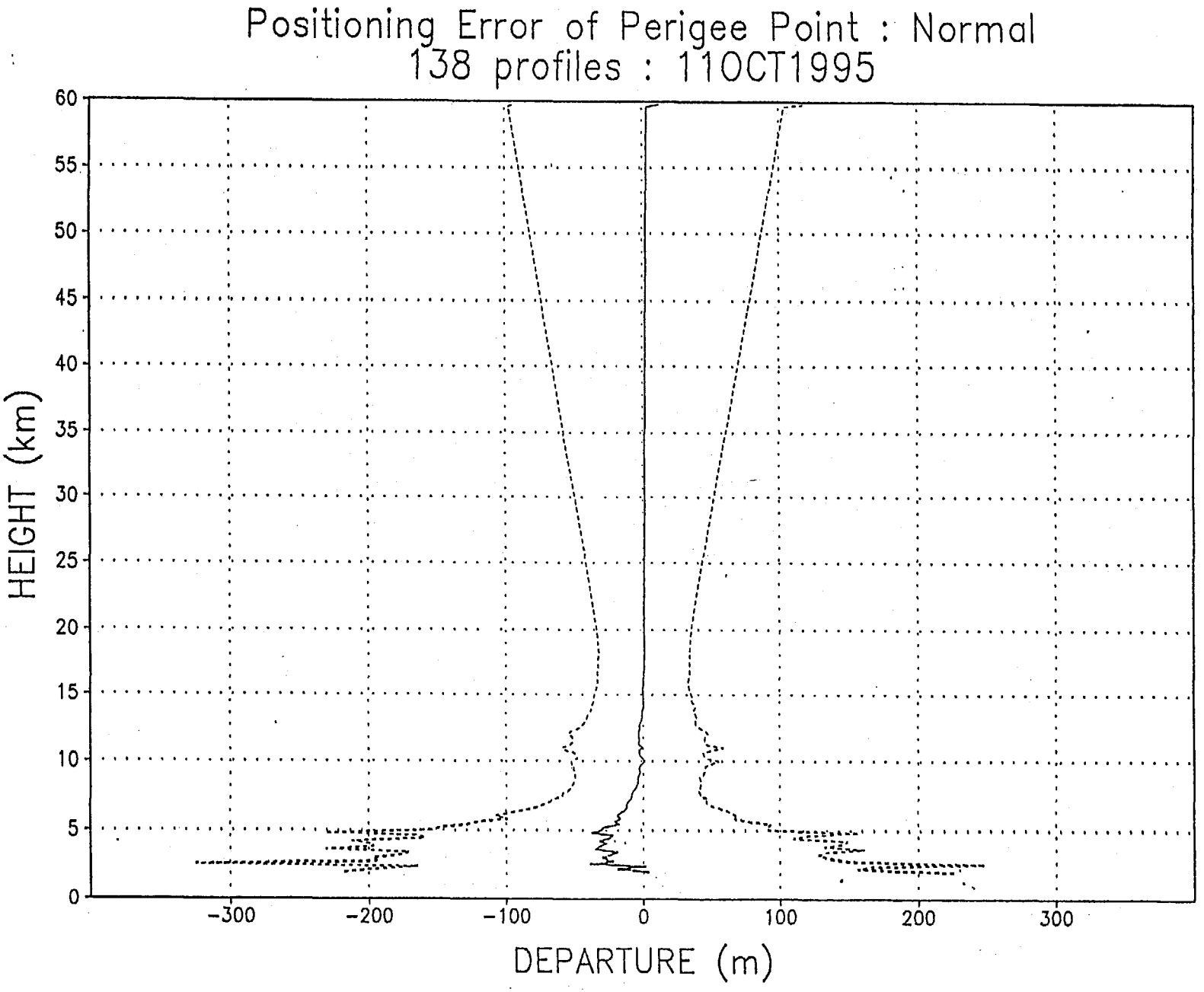

Fig. 3.8 : Same as Fig. 3.6 except mean positioning error normal to the perigee plane.

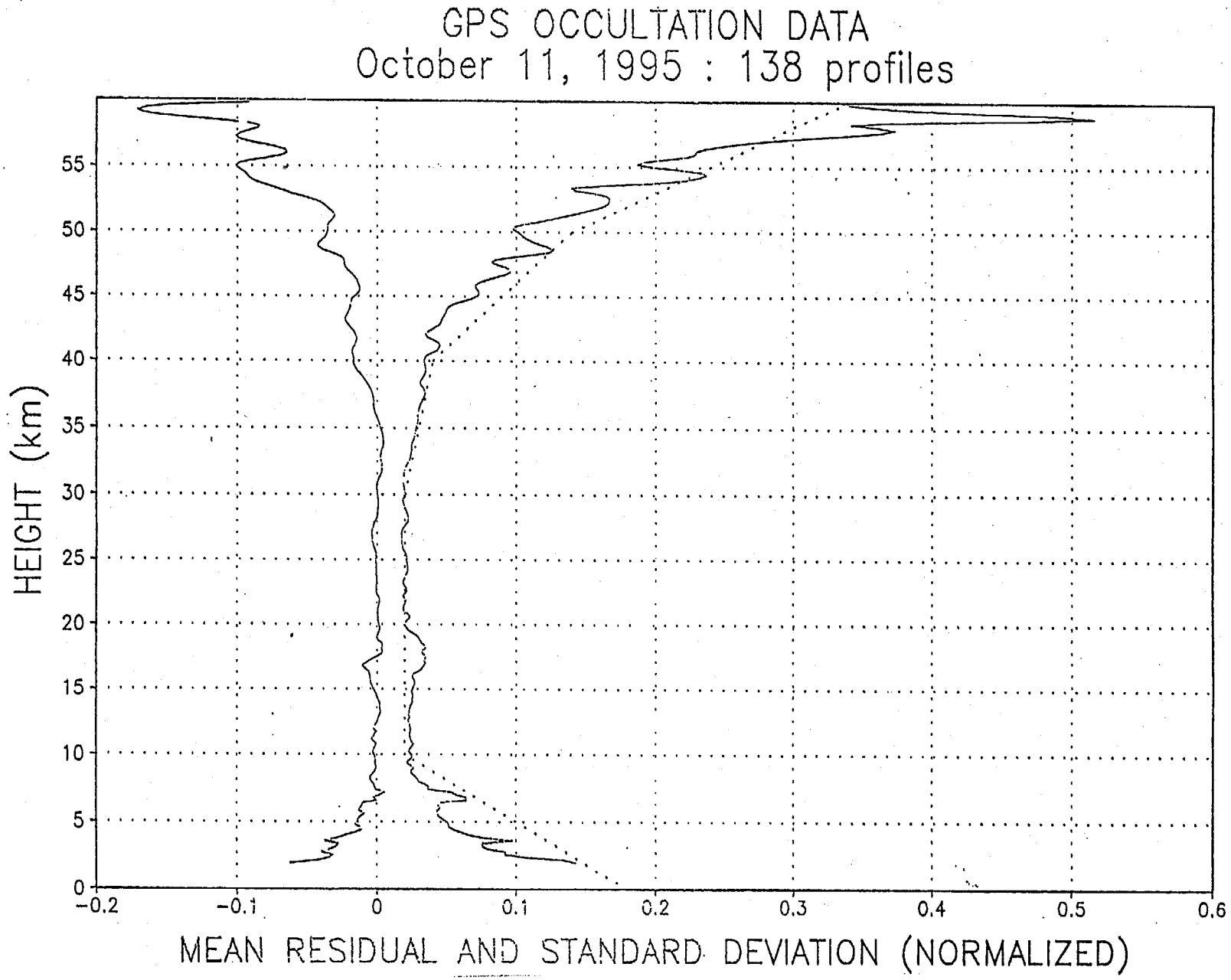

Fig. 3.9 : Average of the observational residual and its standard deviation. The ordinate indicates the altitude of perigee point. Thick solid line is the average $\left(\overline{\Delta\varepsilon}/\varepsilon_r\right)$. Thin solid line is the standard deviation $\left(\sigma_\Delta/\varepsilon_r\right)$. ε_r is the reference profile of the bending angle. Thin dotted line indicates a estimated observation error introduced in section 5.

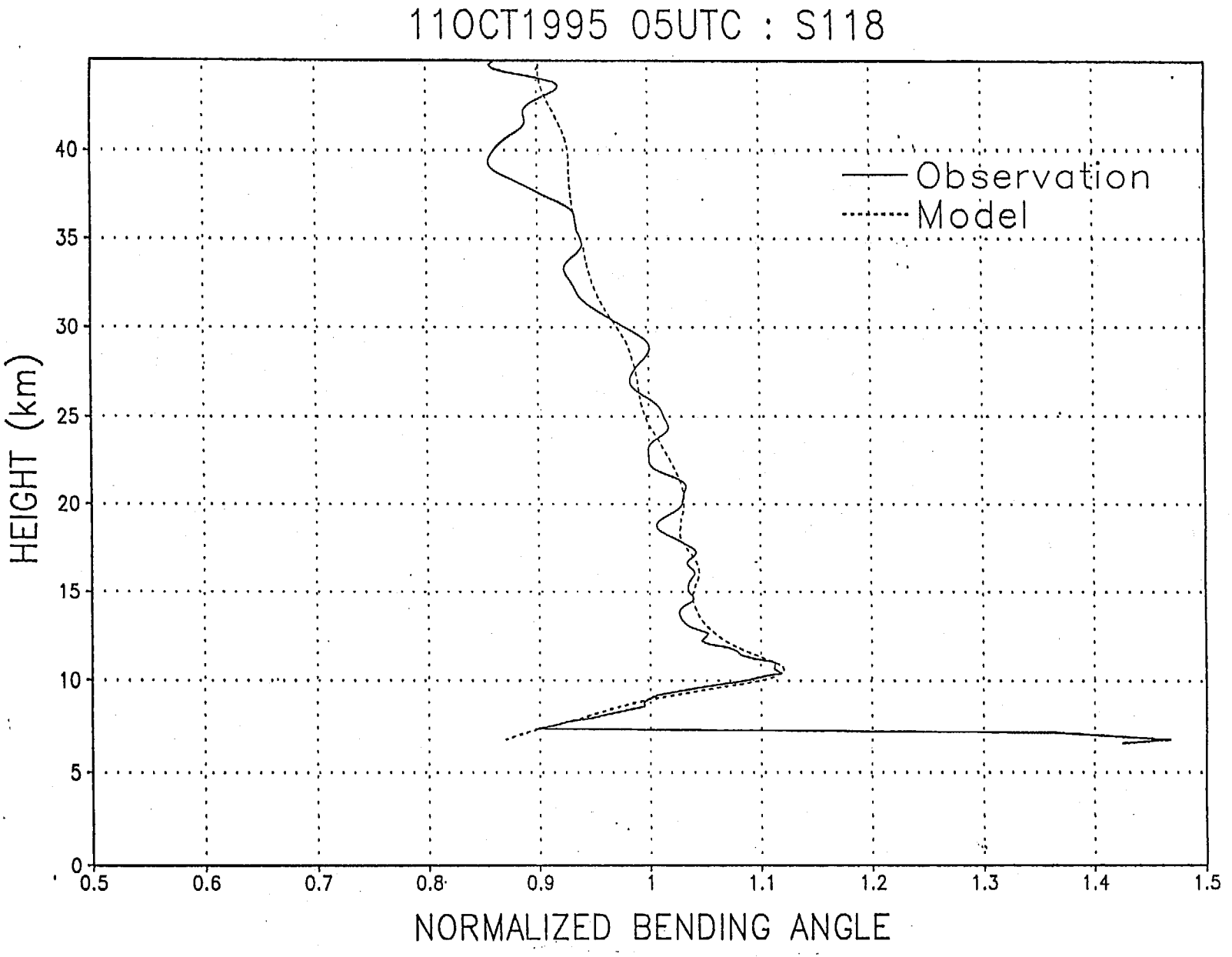

Fig. 3.10 (a) Vertical profile of bending angle at 51.231N, 53.098W. Observation time is 5:25UTC, October 11, 1995. The solid line and the dottod line indicate observation and model simulation respectively. Normalized by the reference profile.

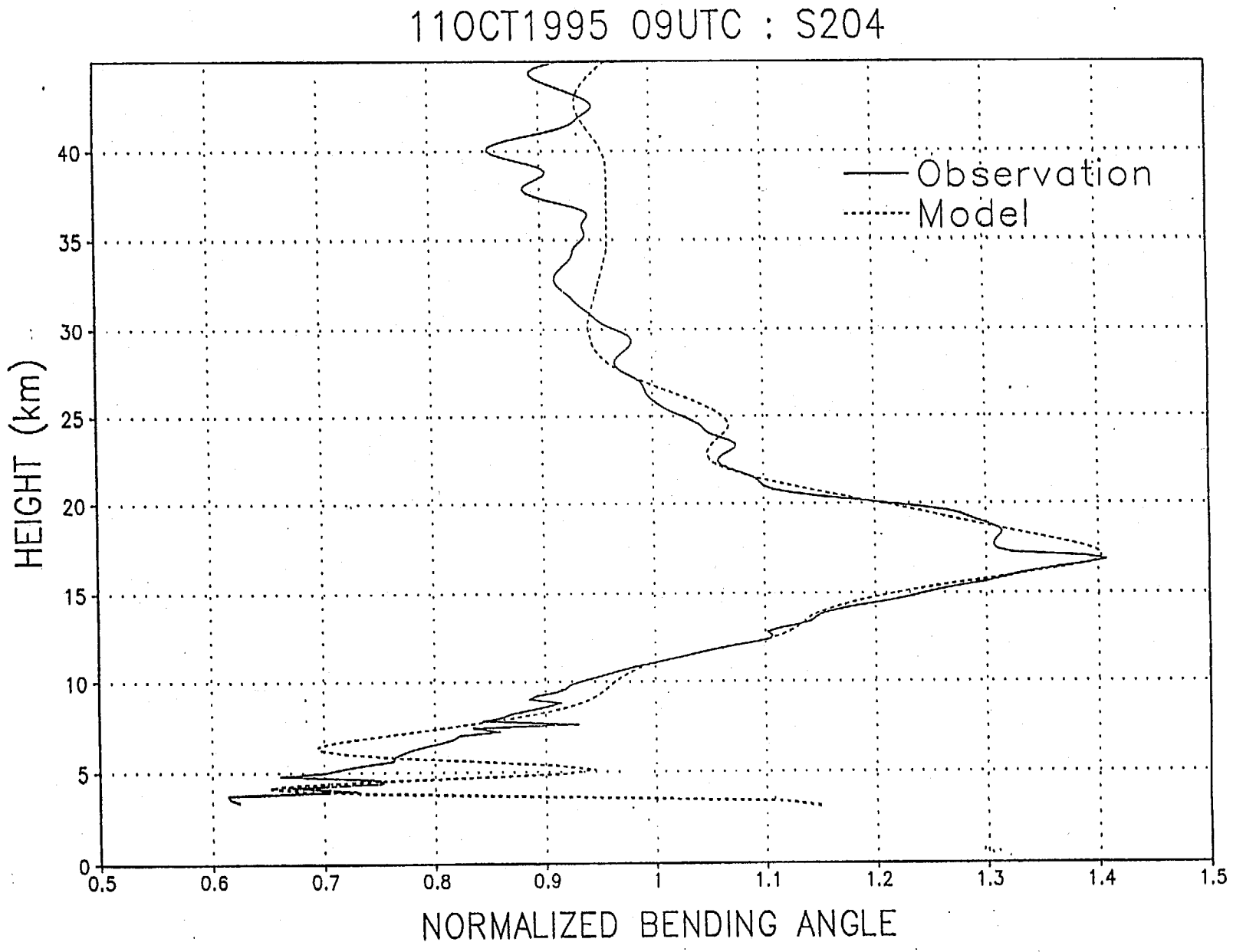

Fig. 3.10 (b) Same as Fig. 3.10 (a) except observation time 9:22UTC and location 8.809S, 49.110E.

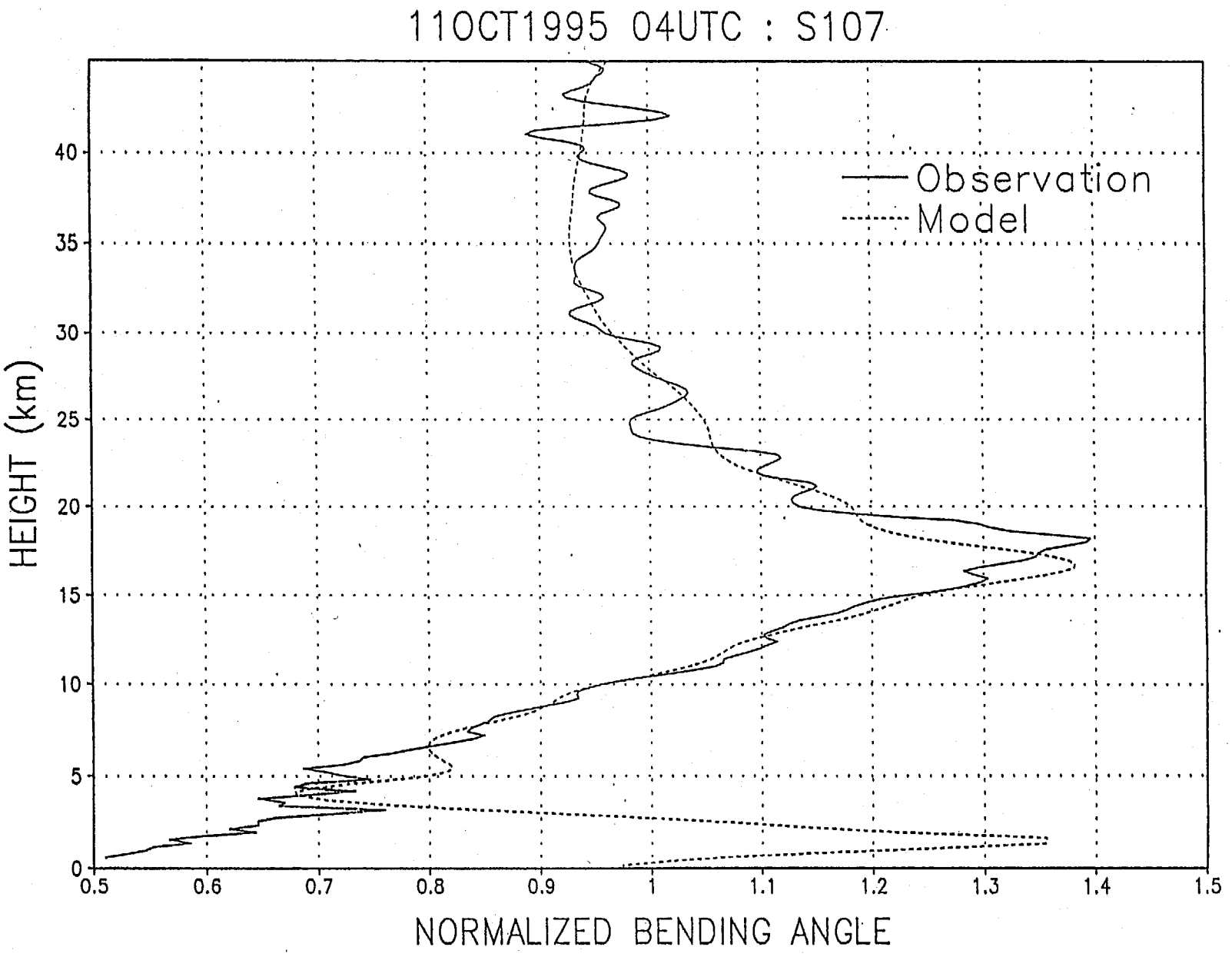

Fig. 3.10 (c) Same as Fig. 3.10 (a) except observation time 3:34UTC and location 25.518N, 54.192W.

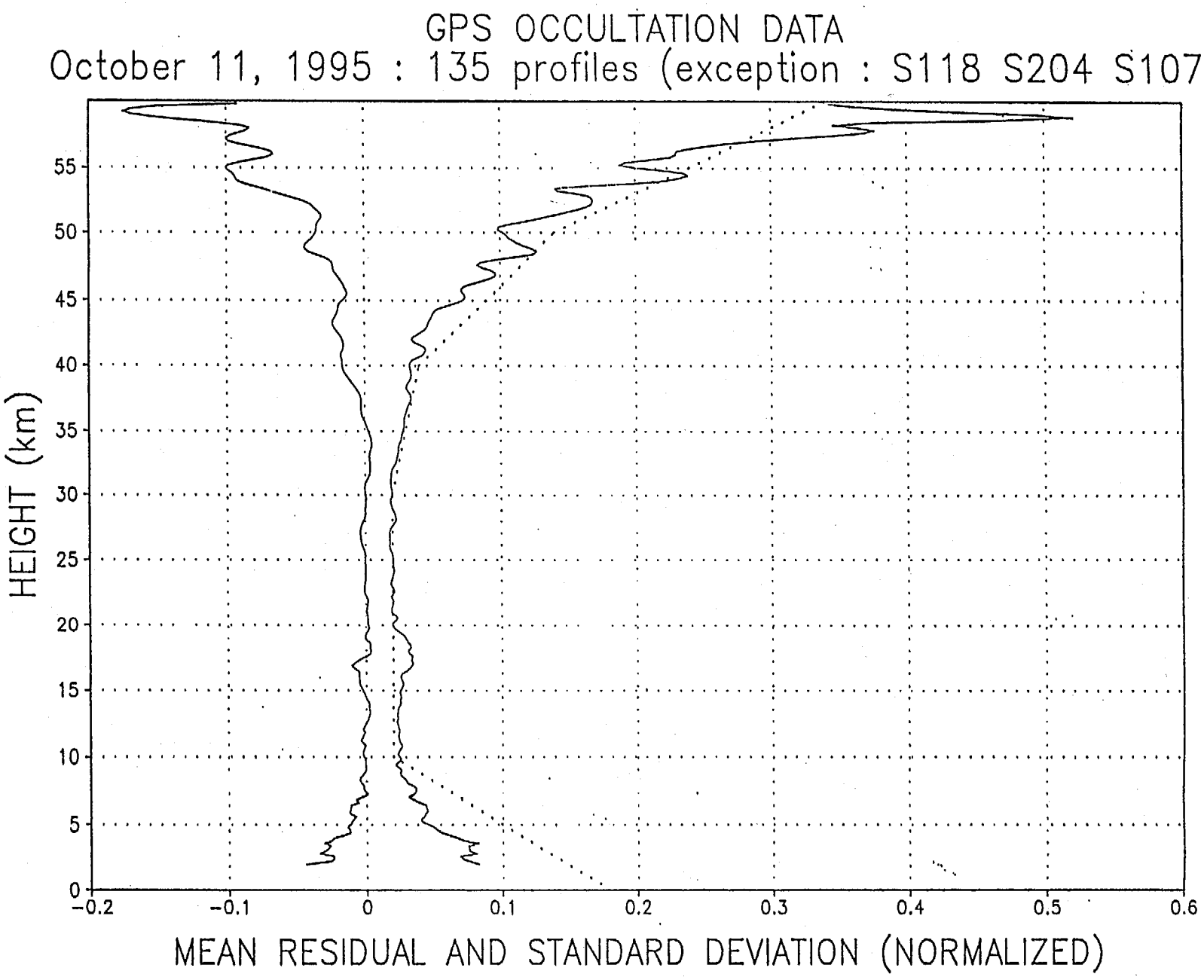

Fig. 3.11 Same as Fig. 3.9 but three soundings in Fig 3.10 are excluded.

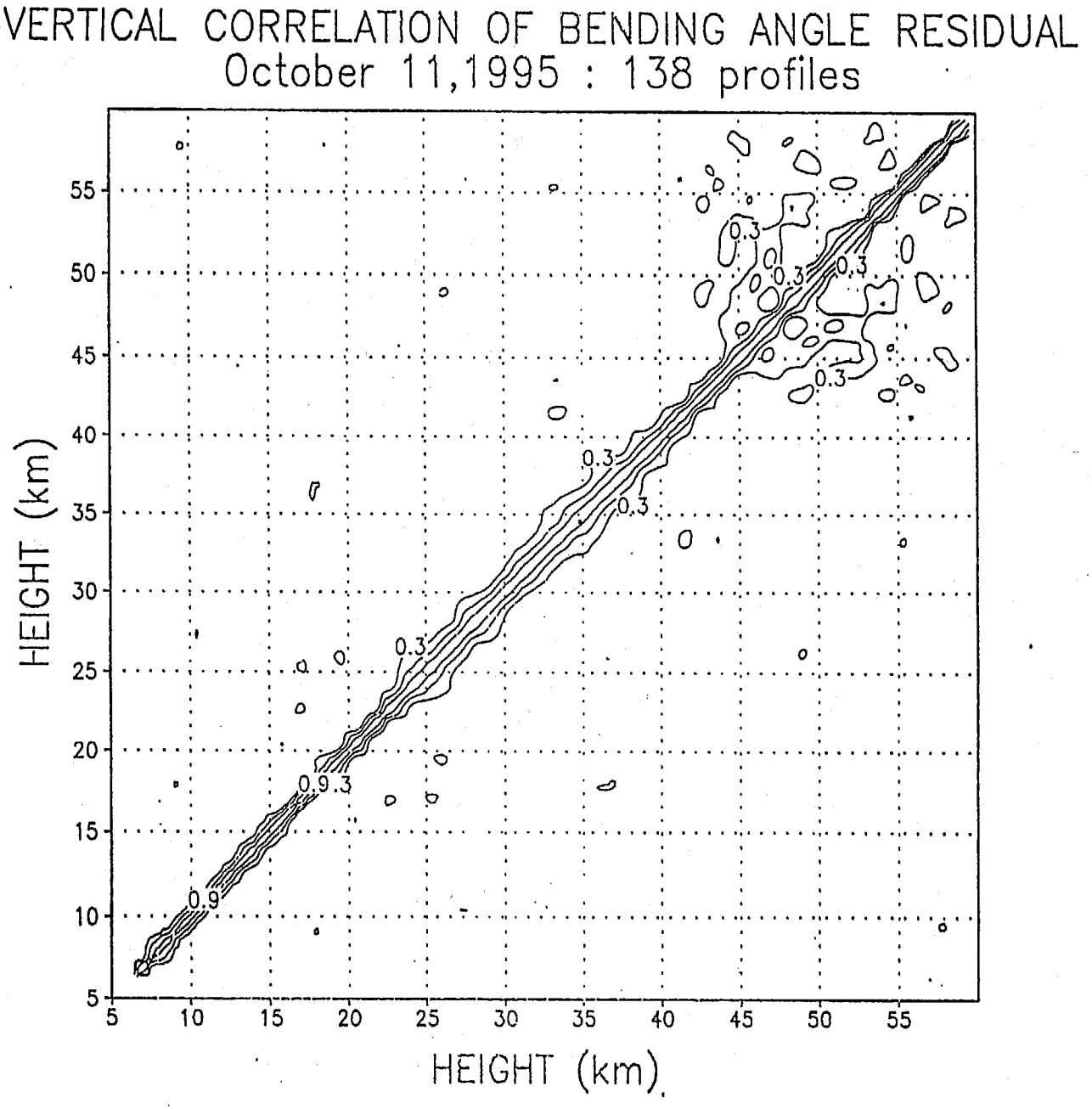

Fig. 3.12 : Vertical correlation of the observational residual. Contour levels are 0.3, 0.6 and 0.9.

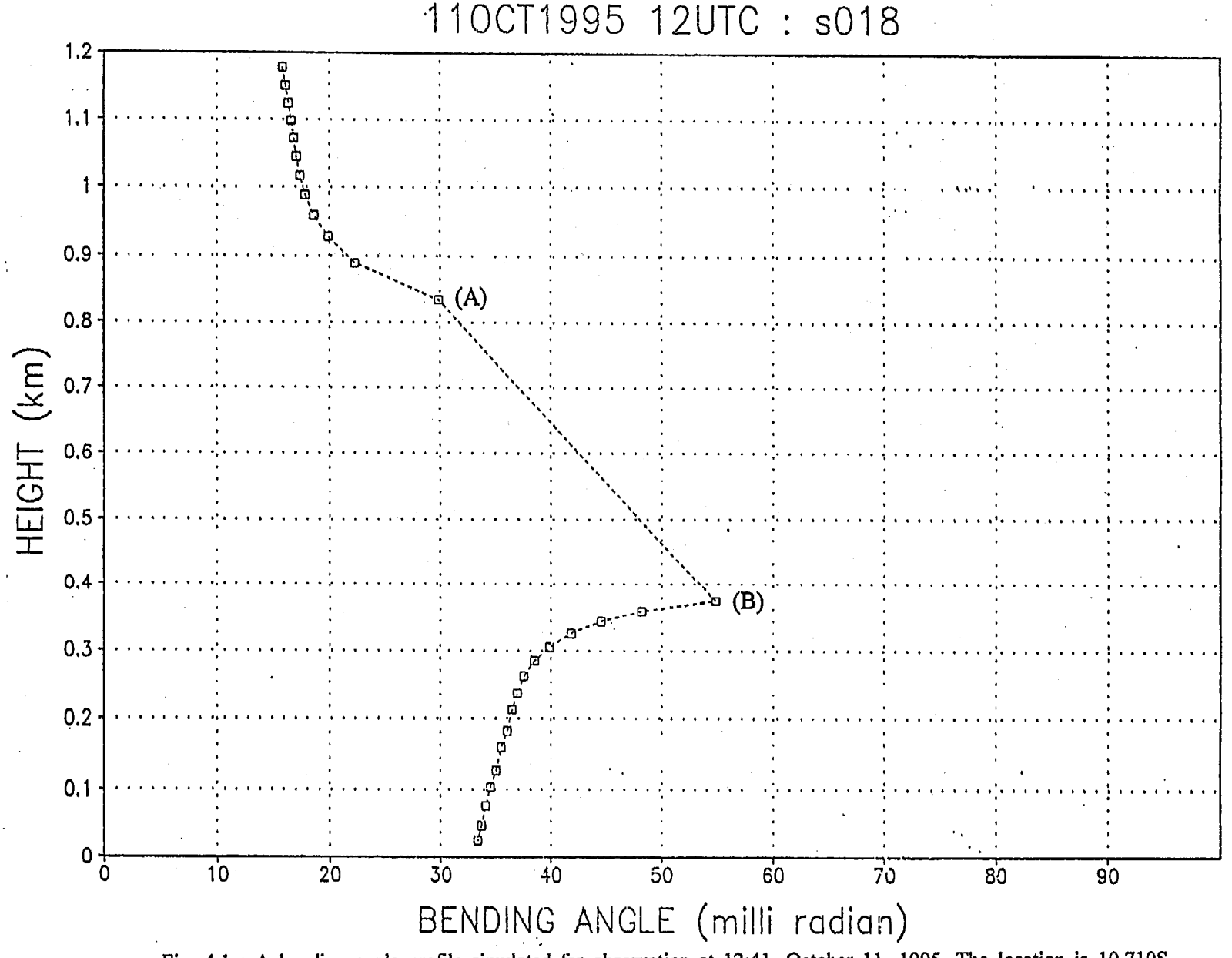

Fig. 4.1 : A bending angle profile simulated for observation at 12:41, October 11, 1995. The location is 10.710S, 0.326W ((4-1) in Fig. 2.1). Analysis field for 12UTC is used for the ray tracing.

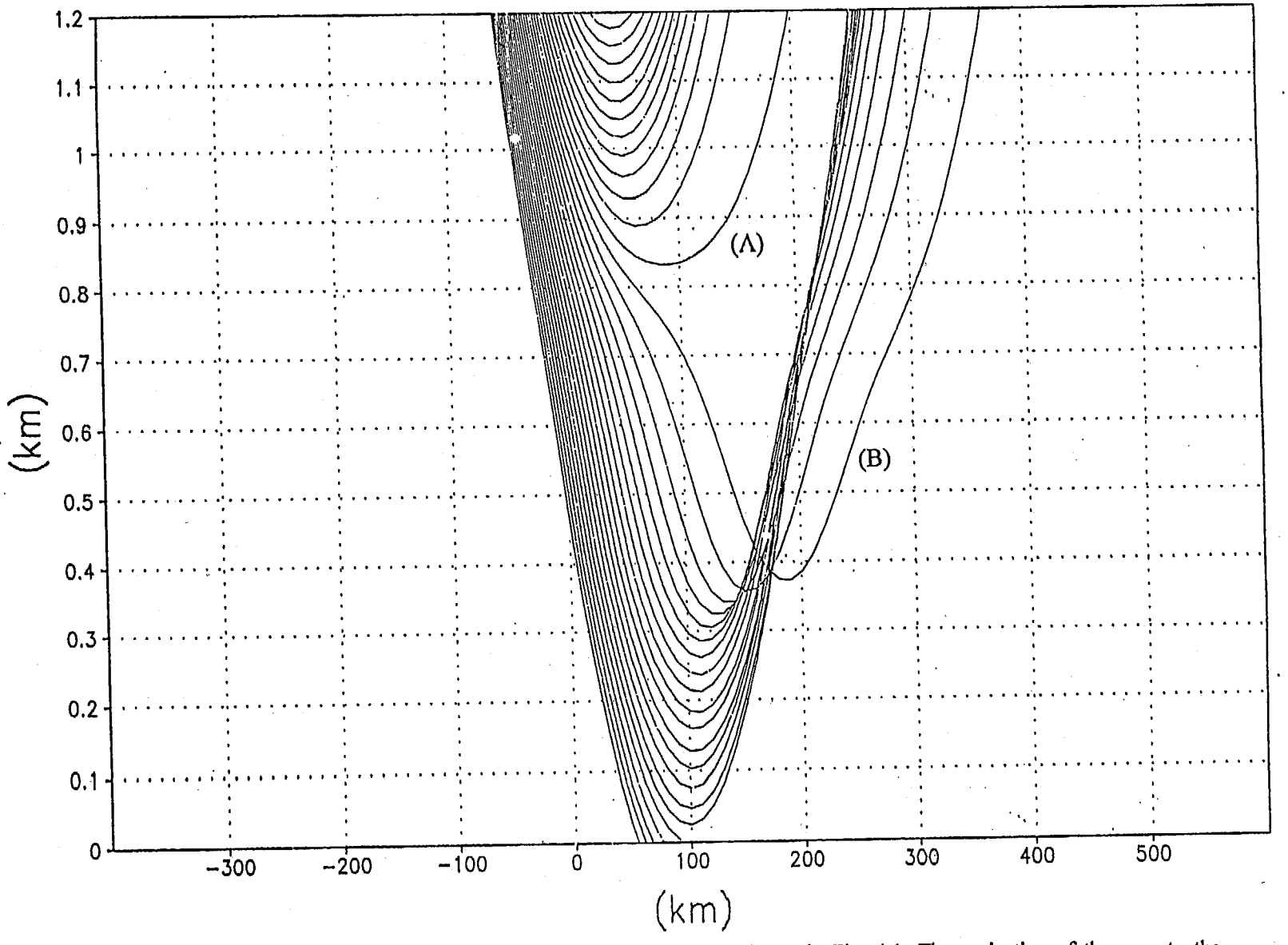

Fig. 4.2 : Ray trajectories simulated for the occultation event shown in Fig. 4.1. The projection of the rays to the occultation plane are displayed. The abscissa indicates the spherical distance on the Earth. Radio signals come down from upper left and go to the right. The rays labeled (A) and (B) correspond to those in Fig. 4.1 respectively.

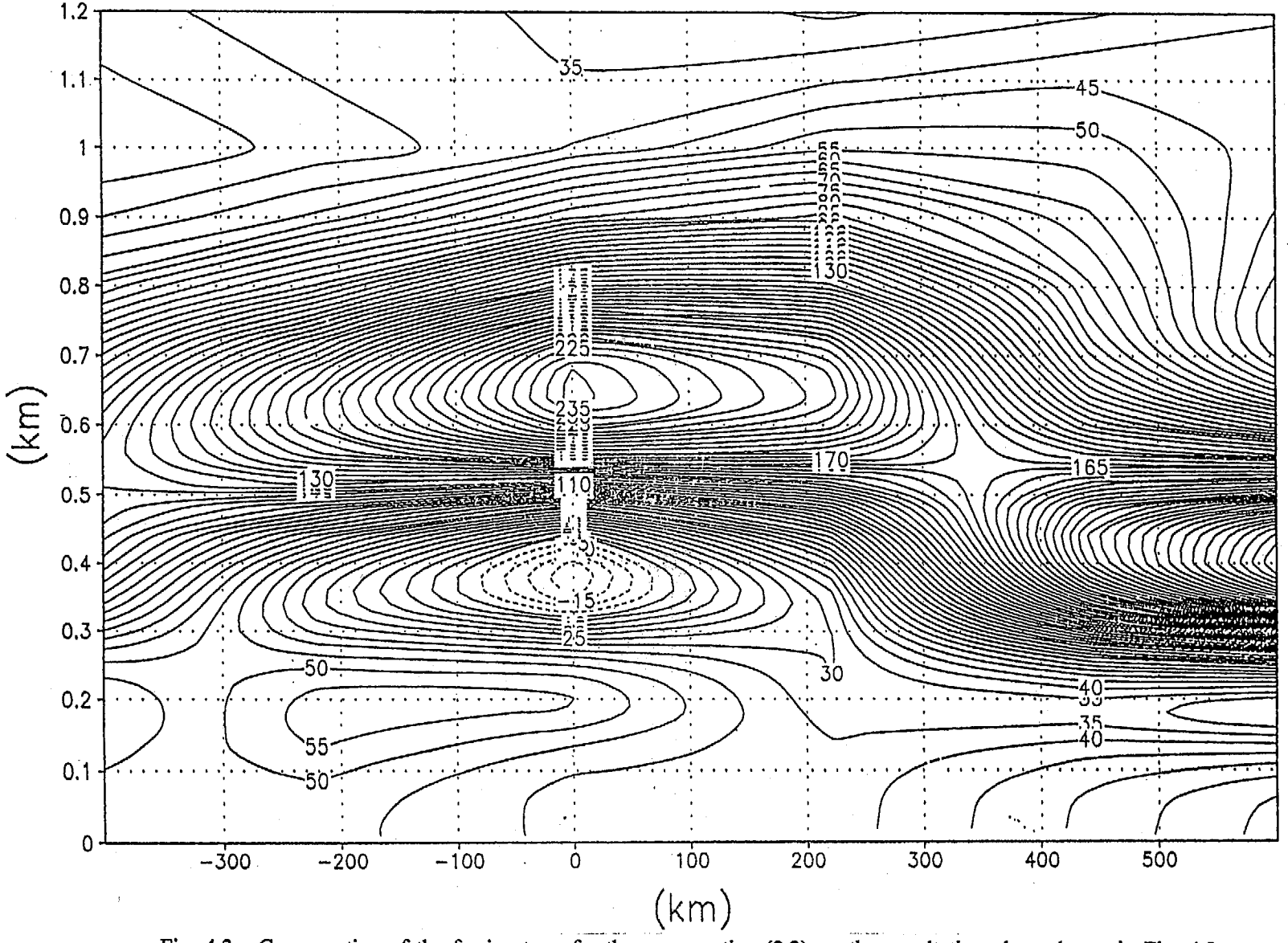

Fig. 4.3 : Cross section of the forcing term for the ray equation (2.2) on the occultation plane shown in Fig. 4.2. $\left(-n\nabla n \times 10^{9}\right)$ is shown, where n is index of refraction. Only the vertical component of the ∇n is taken into account. The analysis field for 12UTC, October 11, 1995 is used.

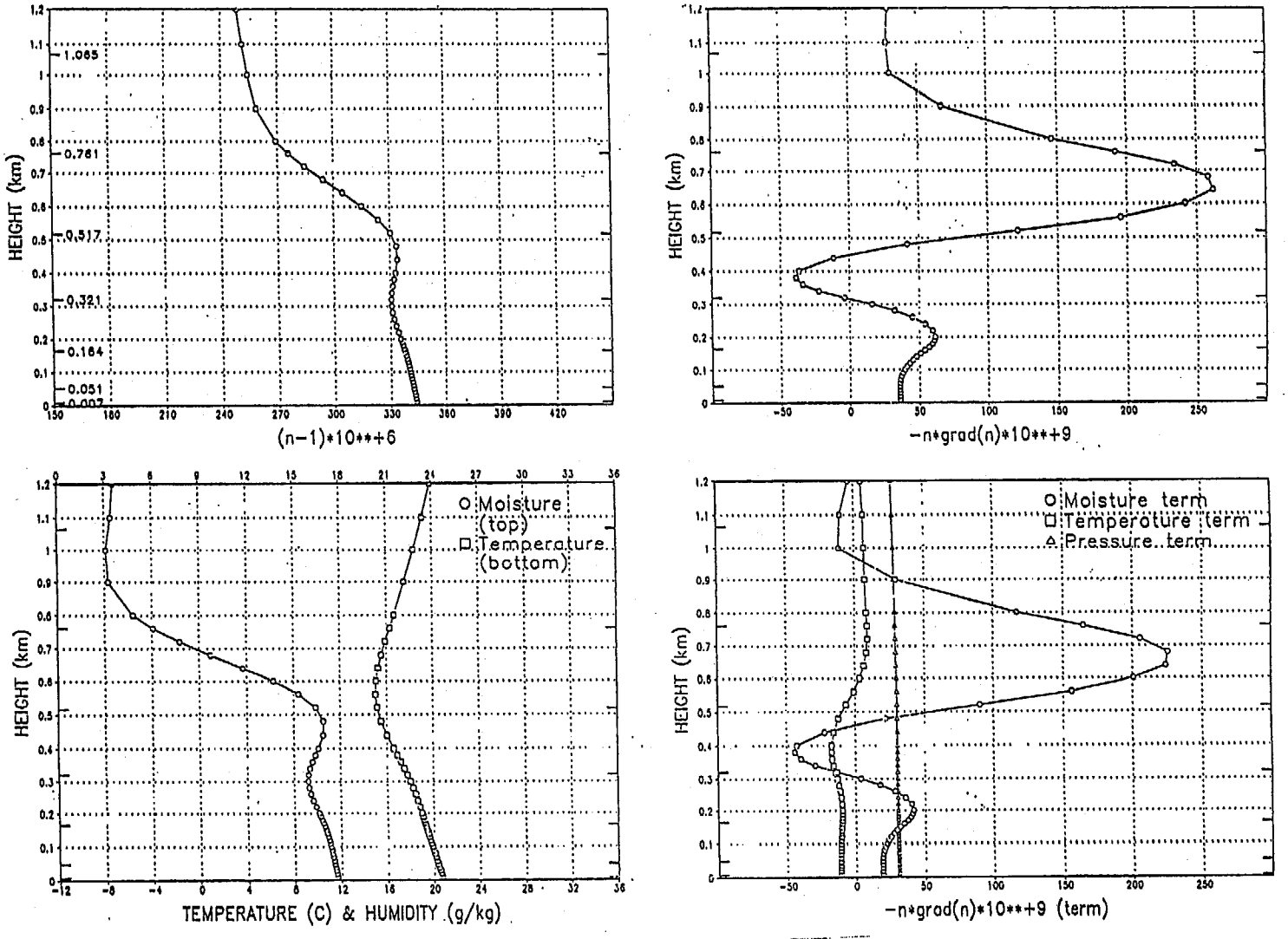

Fig. 4.4 : Vertical profile of $(n-1)\times 10^6$ (a), the forcing term of the ray equation $\left(-n\nabla n\times 10^9\right)$ (b), temperature and moisture (c) and contribution to the forcing from the moisture term $\left(c_2 n\nabla Pw/T^2\right)$, temperature term $\left(-n(n-1)\nabla T/T\right)$ and the pressure term $\left(c_1 n\nabla P/T\right)$ (d) for the occultation event shown in Fig. 4.1. The analysis field for 12UTC, October 11, 1995 is used. n is the index of refraction and the thick mark along the vertical scale indicates the model layer height at this point.

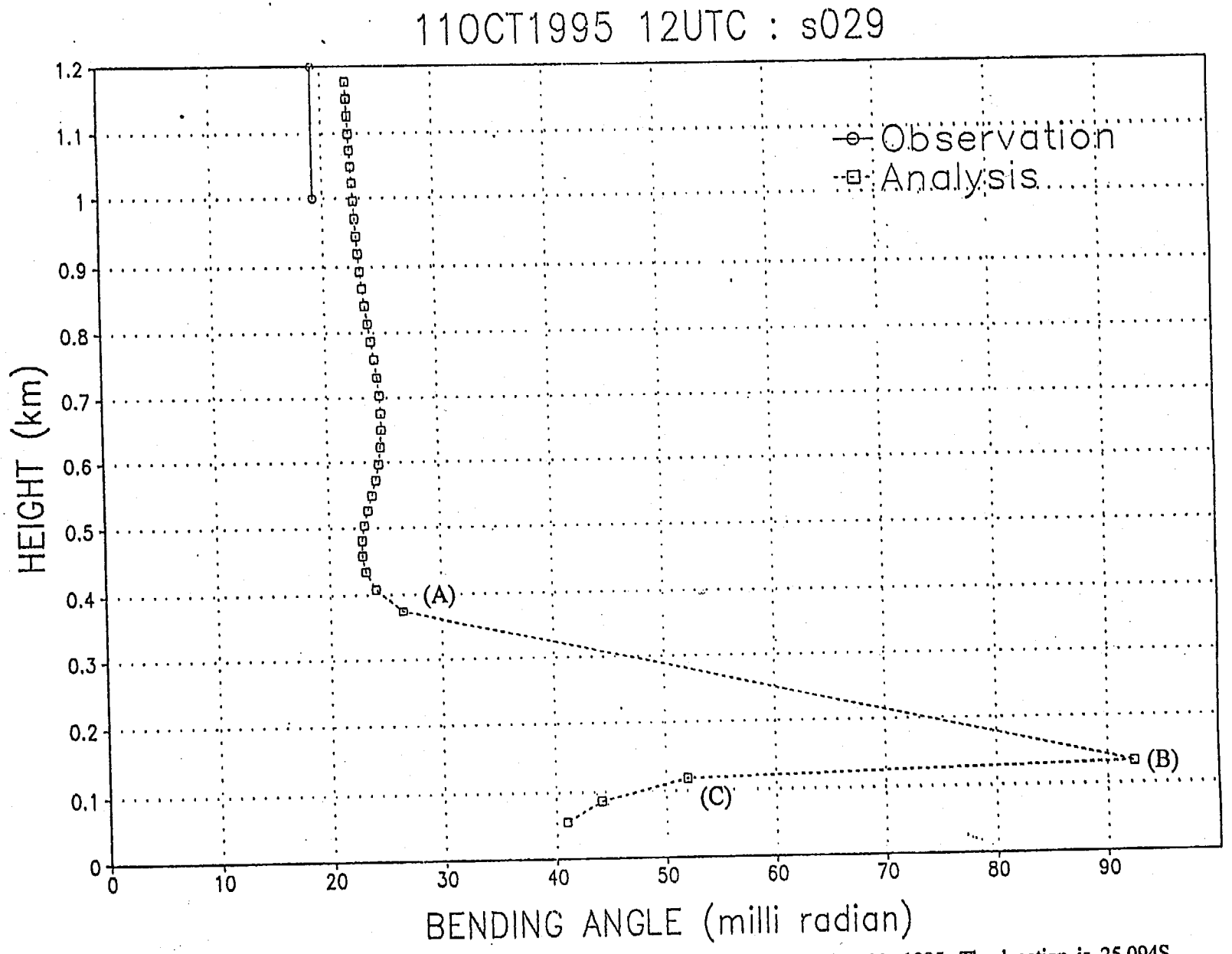

Fig. 4.5 : A bending angle profile simulated for observation at 14:26, October 11, 1995. The location is 25.094S, 15.479W ((4-2) in Fig. 2.1). The analysis field for 12UTC is used for the ray tracing.

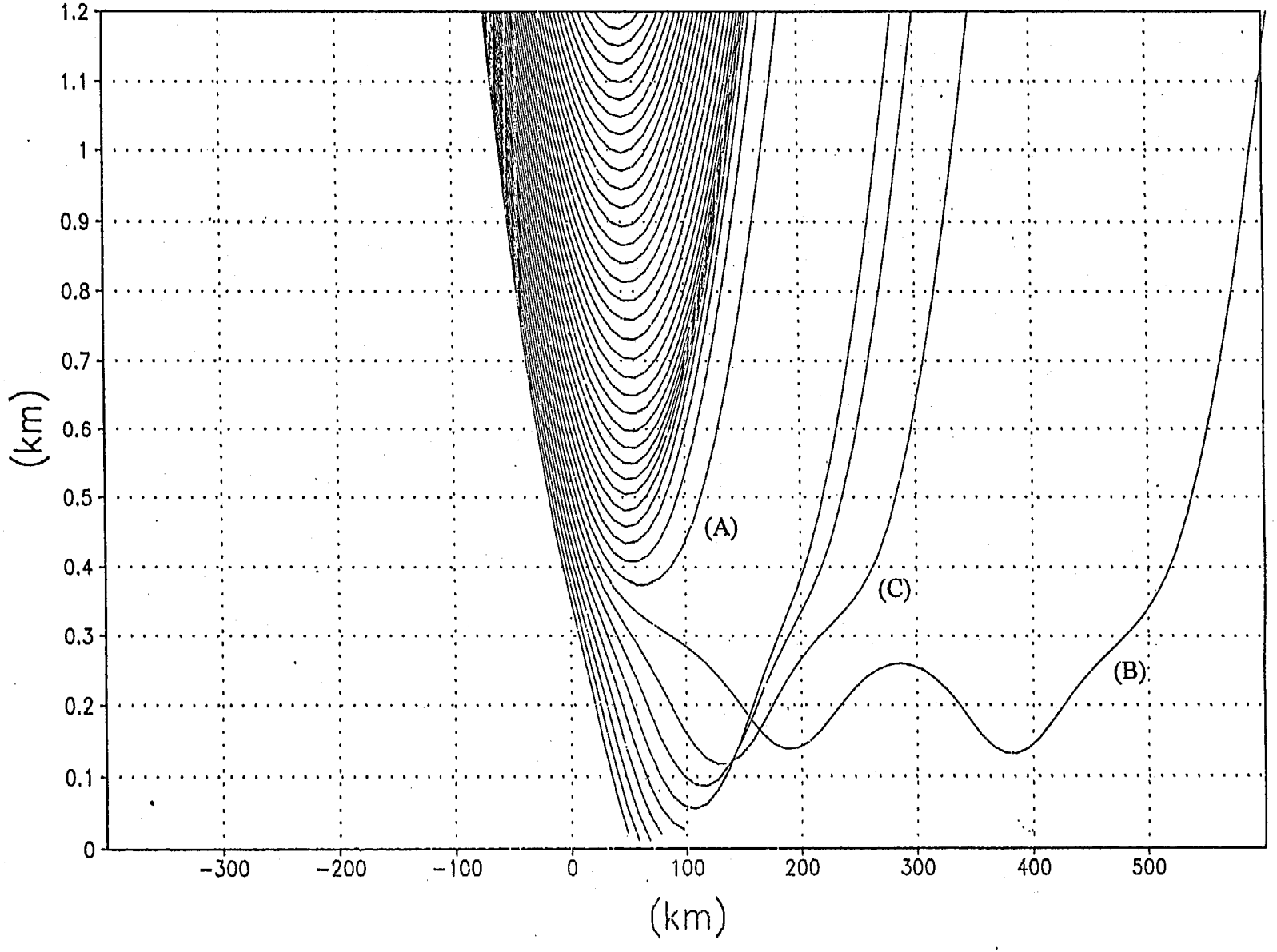

Fig. 4.6 : Same as Fig.4.2 except showing occultation event in Fig.4.5.

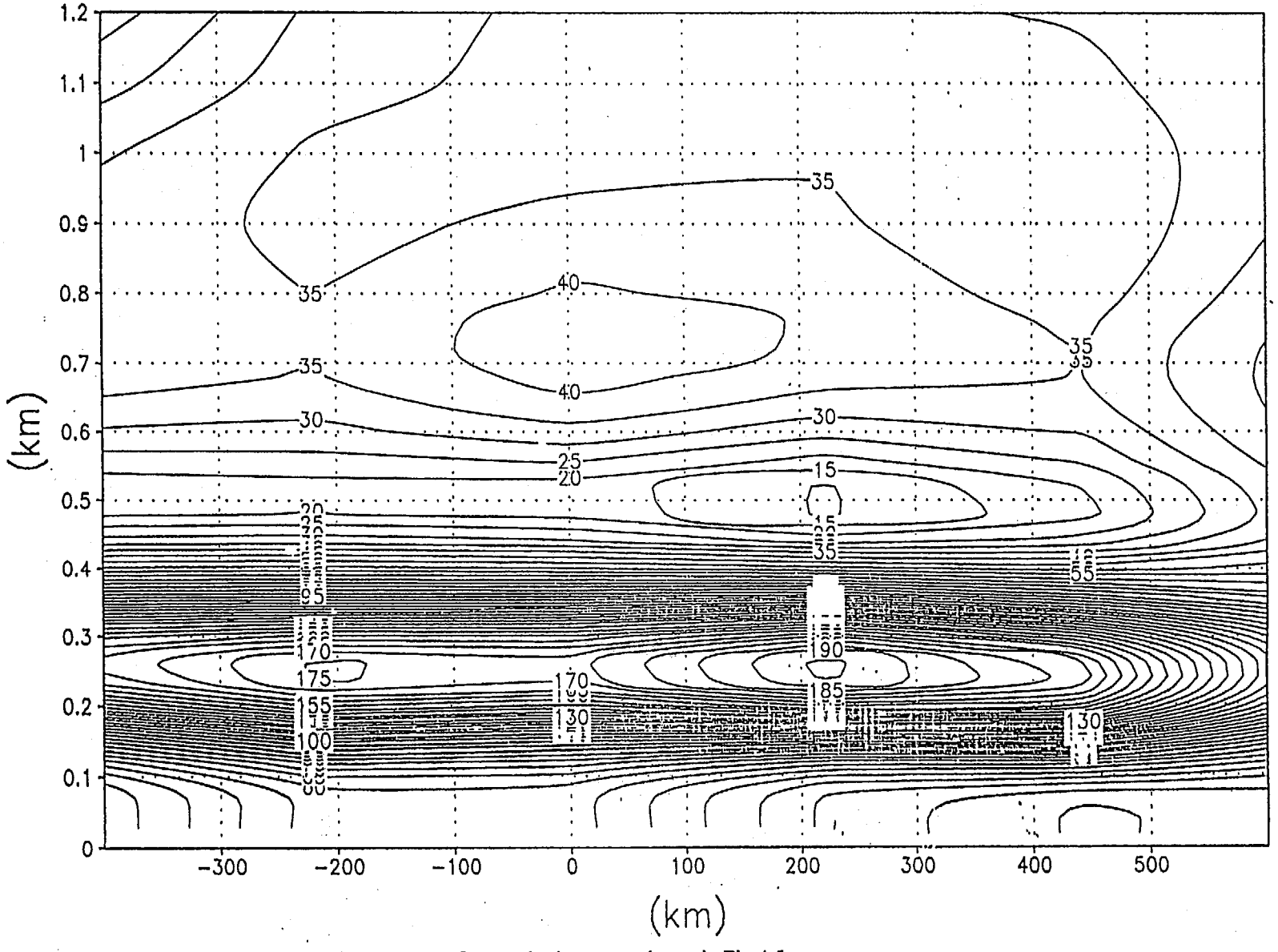

Fig. 4.7 : Same as Fig.4.3 except for occultation event shown in Fig.4.5.

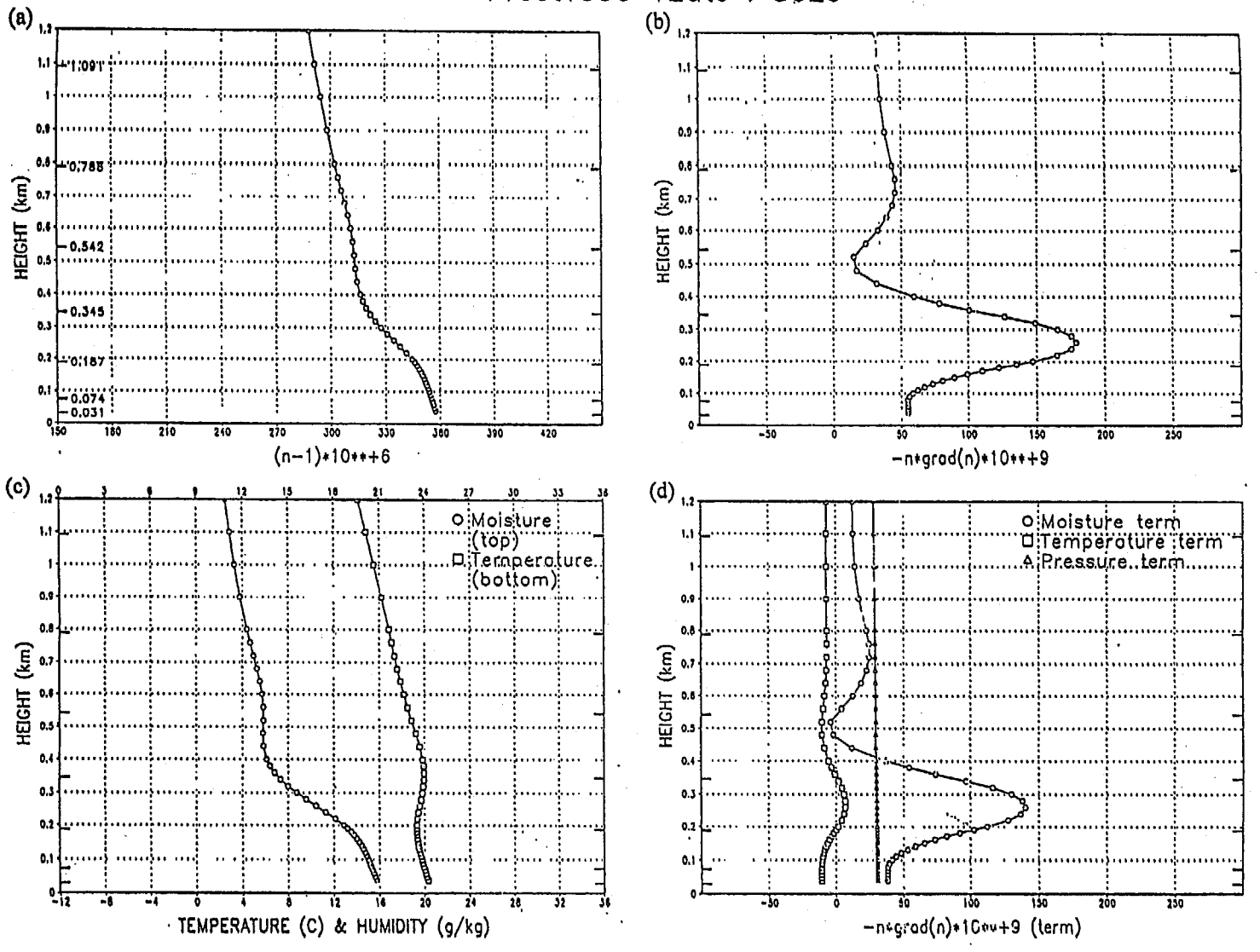

Fig. 4.8 : Same as Fig.4.4 except for occultation event shown in Fig.4.5.

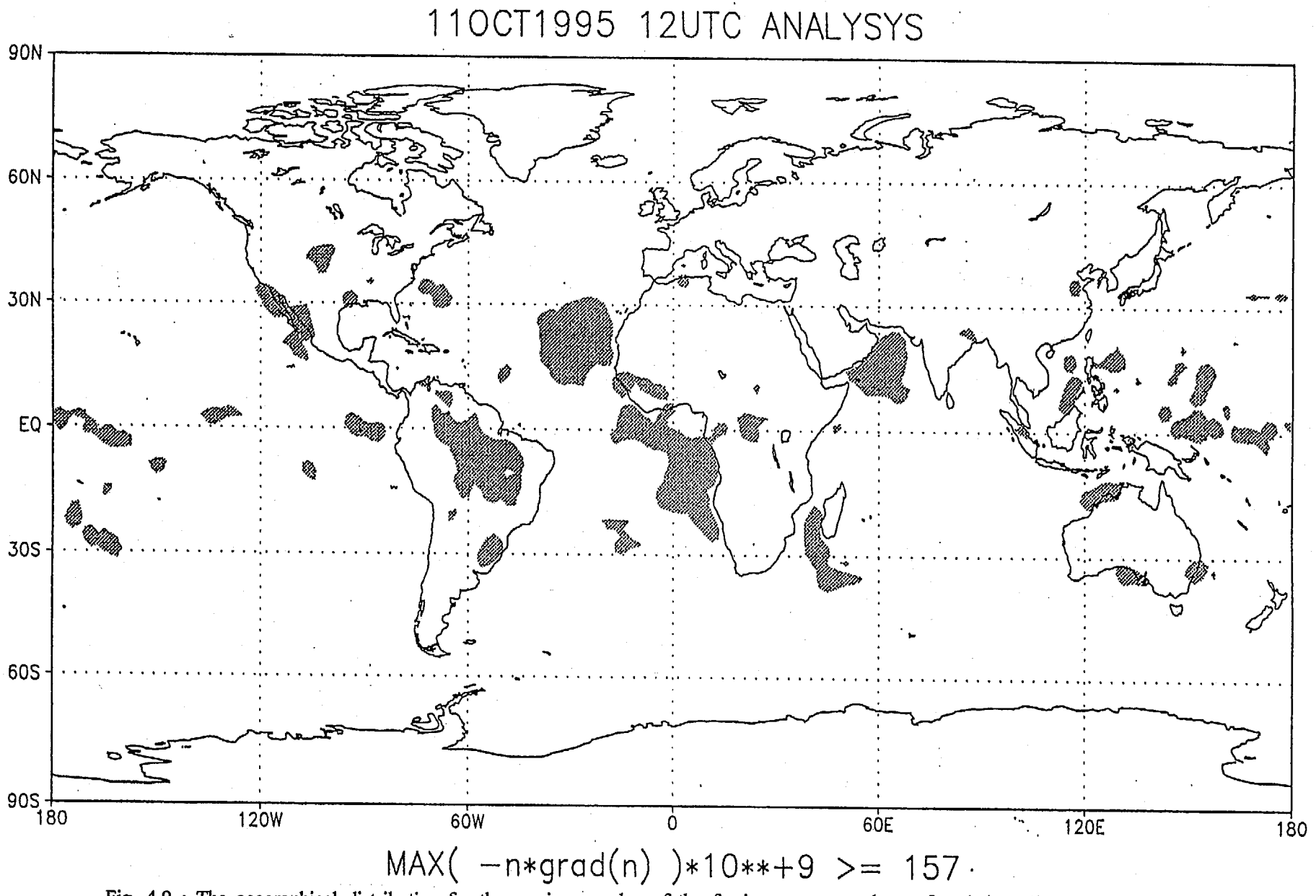

Fig. 4.9 : The geographical distribution for the maximum value of the forcing term near the surface below 4km $\left(-n\nabla n \times 10^{9}\right)$, where n is index of refraction. Only values larger than 157×10^{-9} are displayed. The values are derived from the global analysis for 12UTC, October 11, 1995.

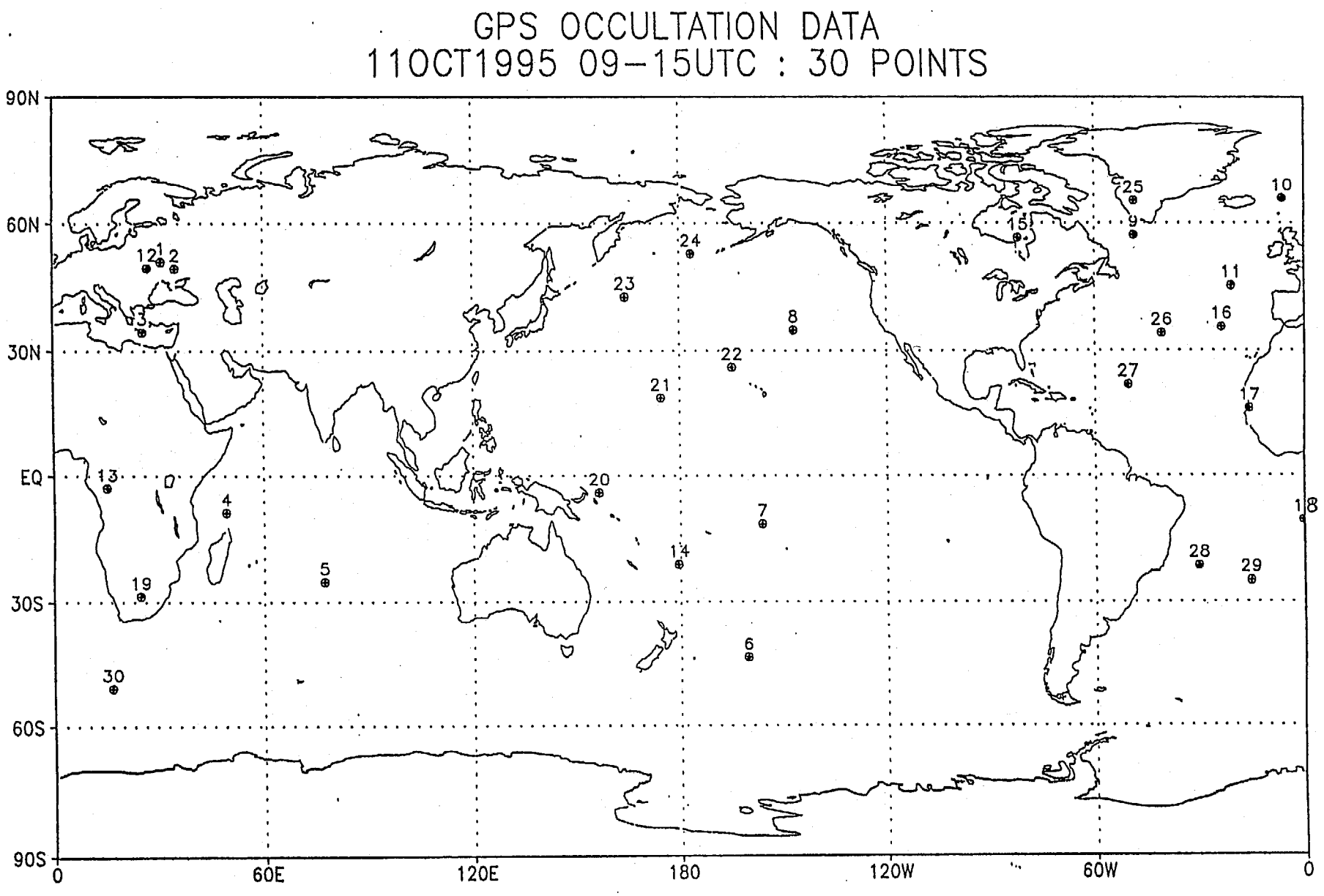

Fig. 5.1 : Location of 30 GPS data from 09UTC to 15UTC, October 11, 1995. The 15th observation is used in EXP 1.
All data are used in EXP 2 and EXP 3

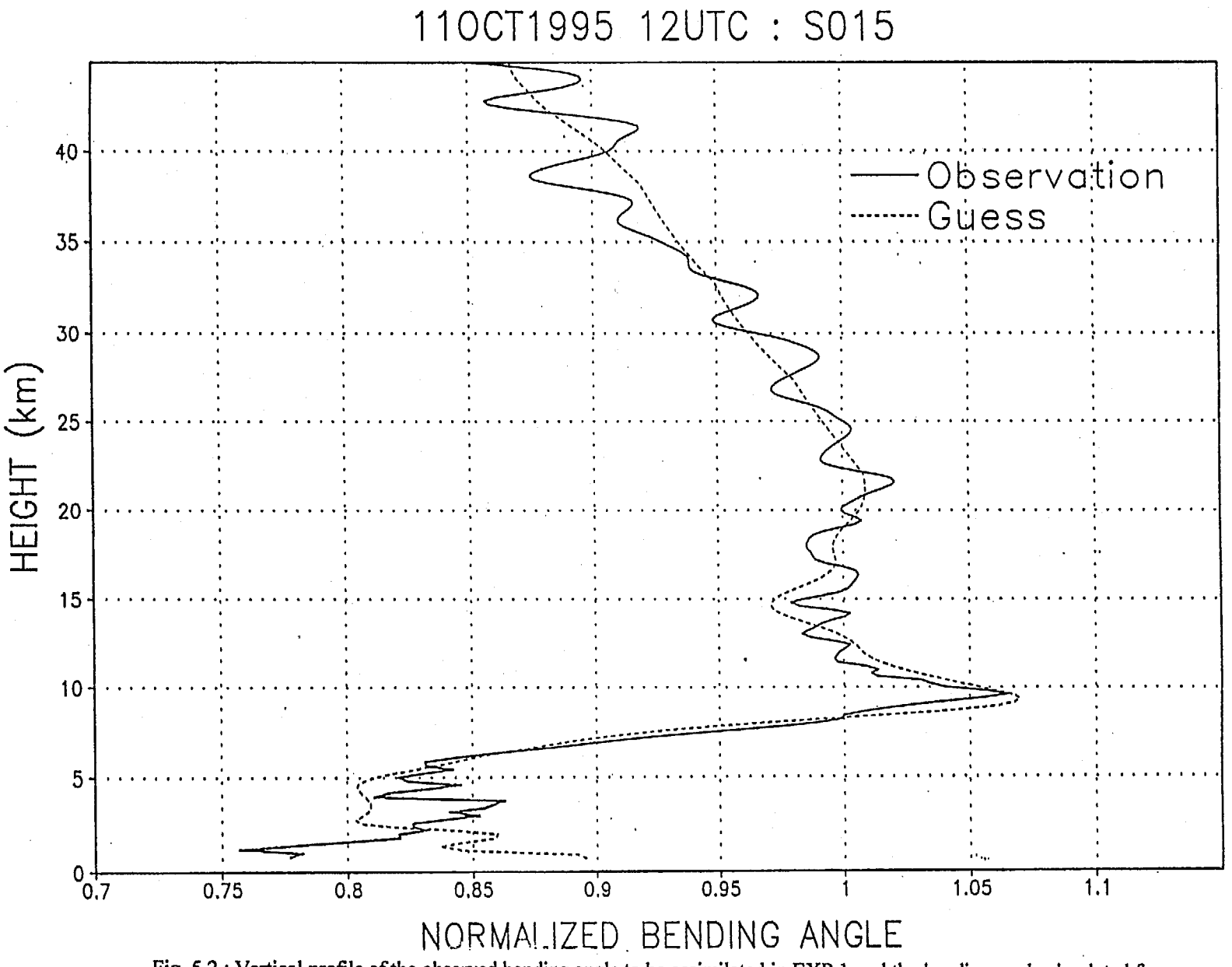

Fig. 5.2 : Vertical profile of the observed bending angle to be assimilated in EXP 1 and the bending angle simulated from the background field. Thick solid line is the observed. Thin dashed line is the simulated. Normalized by the reference profile ε_r .

	GPS data (number)	conventional data	back ground field
EXP 1	yes (1)	no	operational analysis
EXP 2	yes (30)	no	operational analysis
EXP 3	yes (30)	yes	6 hours forecast for the analysis time
EXP 4	no	yes	6 hours forecast for the analysis time

Table 5.1 :Configuration of the experiments.

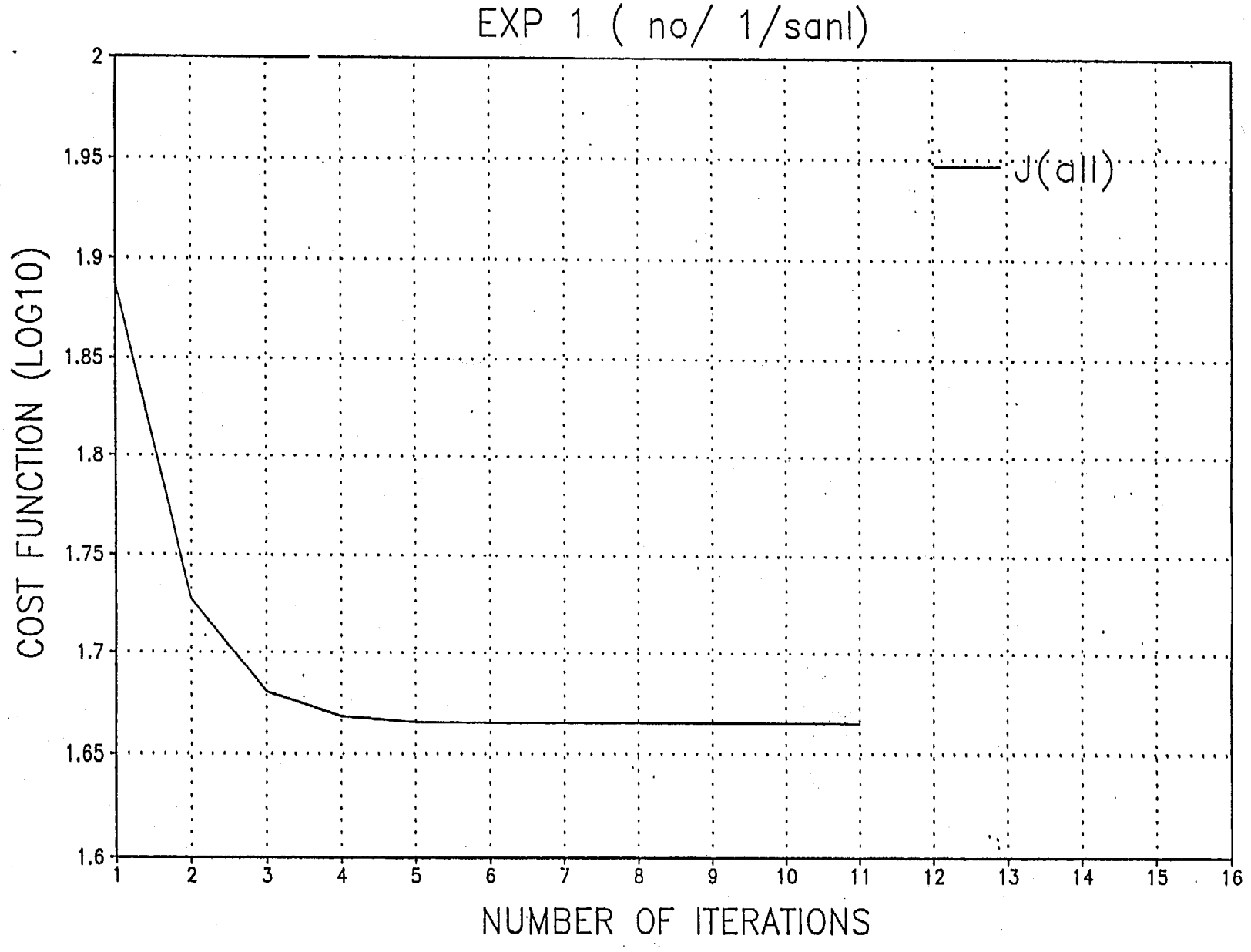

Fig. 5.3 : The variation of cost function during the minimization procedure in EXP 1 with respect to the number of iterations.

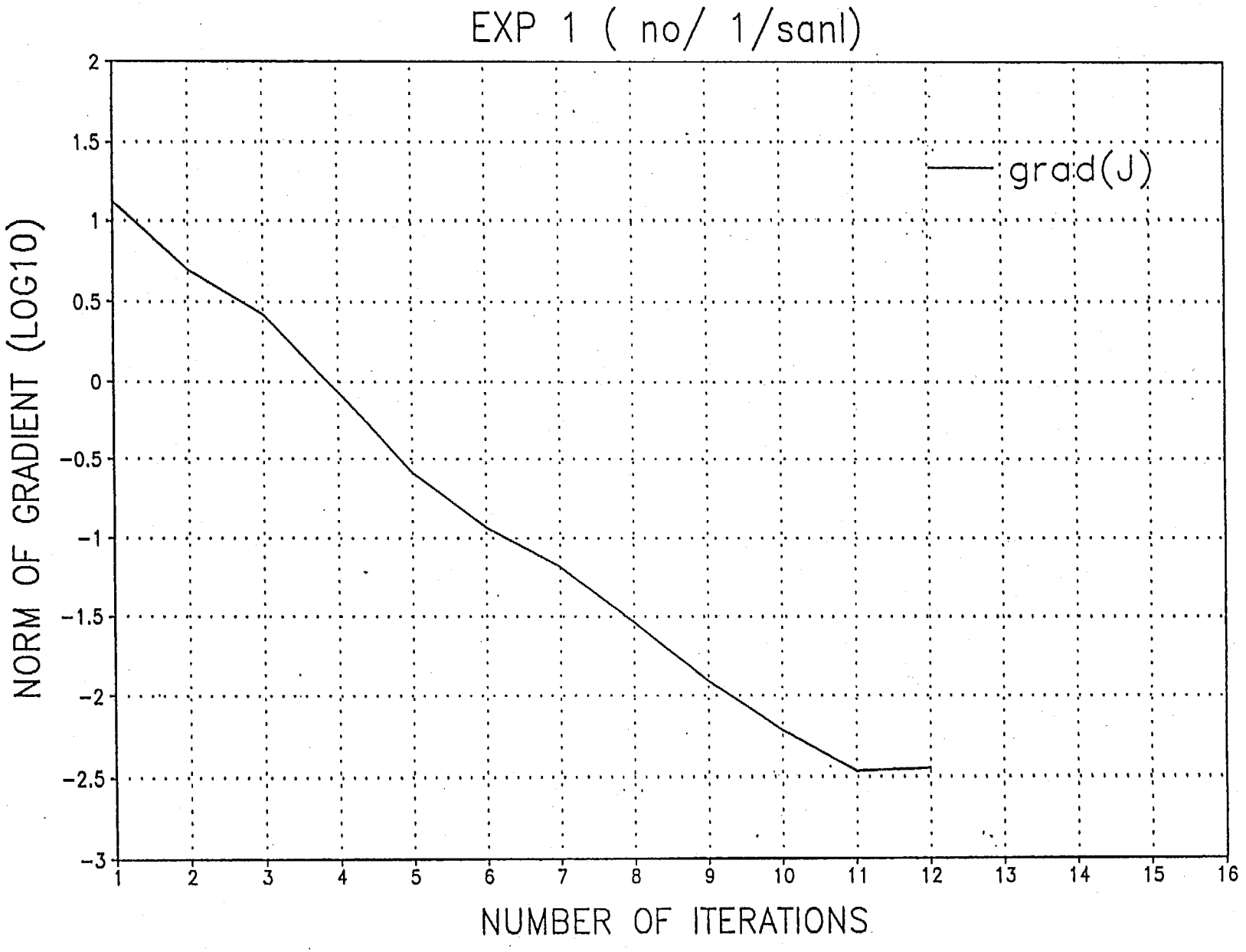

Fig. 5.4 : The norm of gradient of the cost function during the minimization procedure in EXP 1 with respect to the number of iterations. The 12th iteration corresponds to the first inner loop of the second outer iteration.

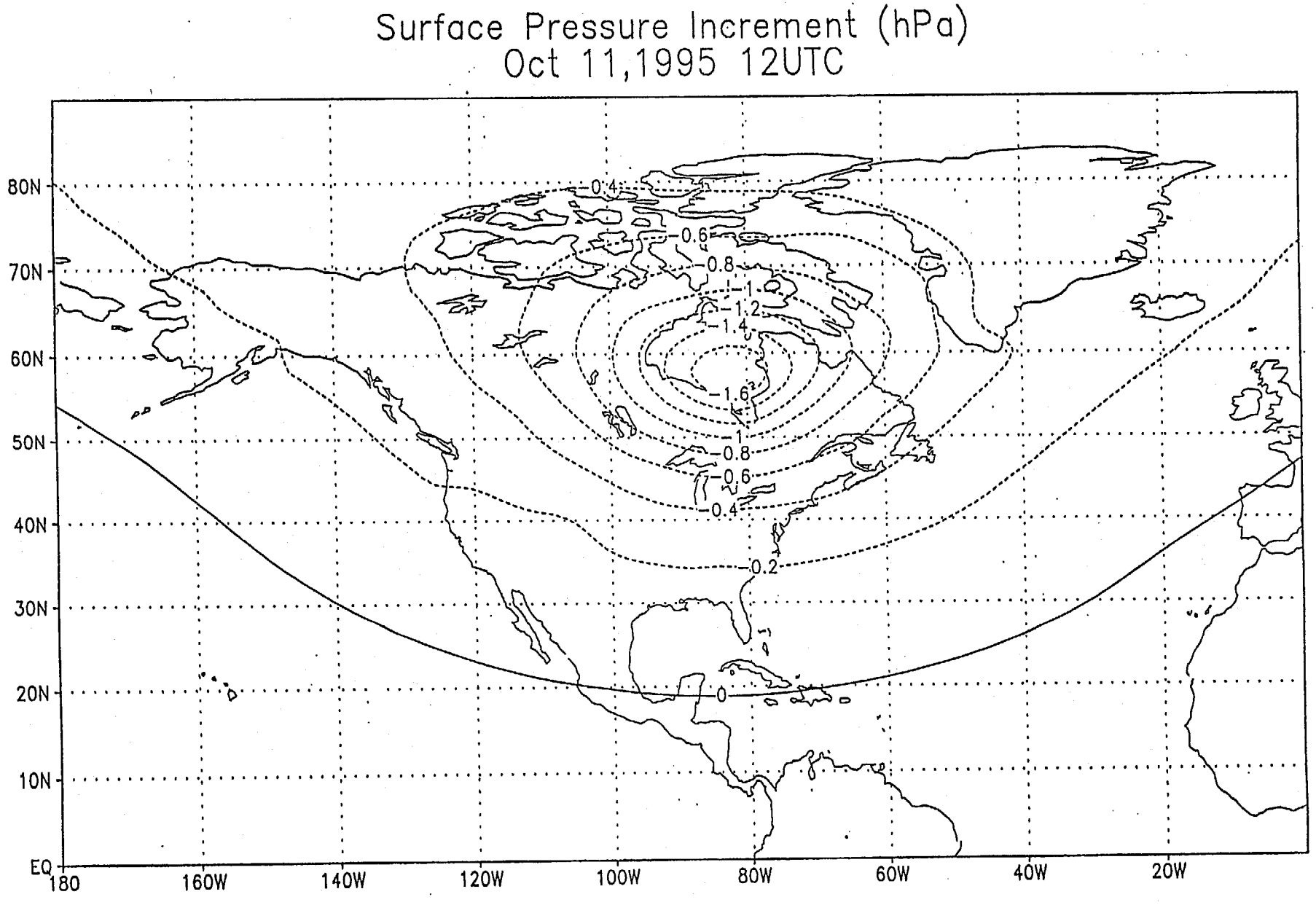

Fig. 5.5 : Analysis increment of surface pressure in EXP 1.

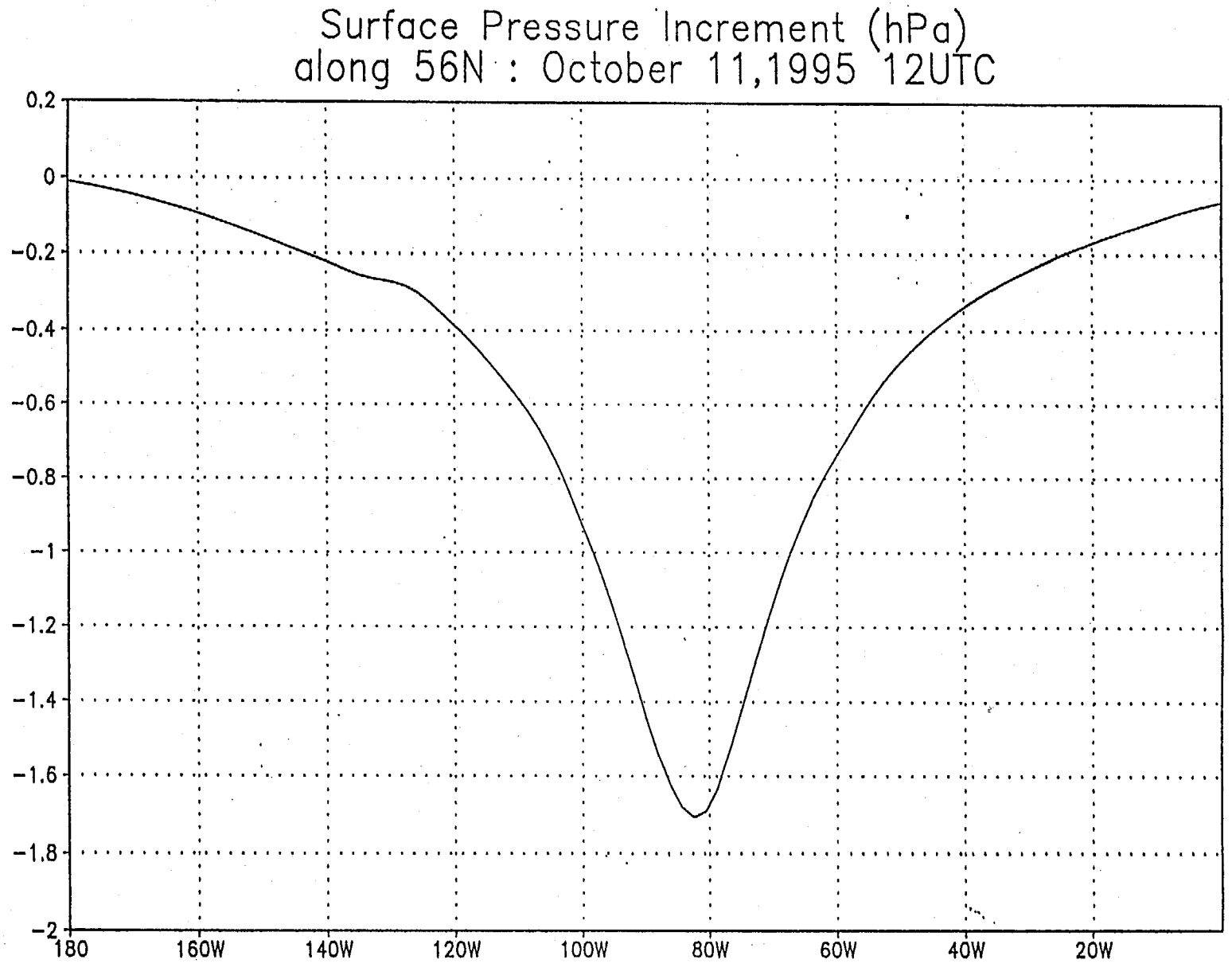

Fig. 5.6 : Analysis increment of surface pressure in EXP 1 along 56N from the date line to the Greenwich meridian.

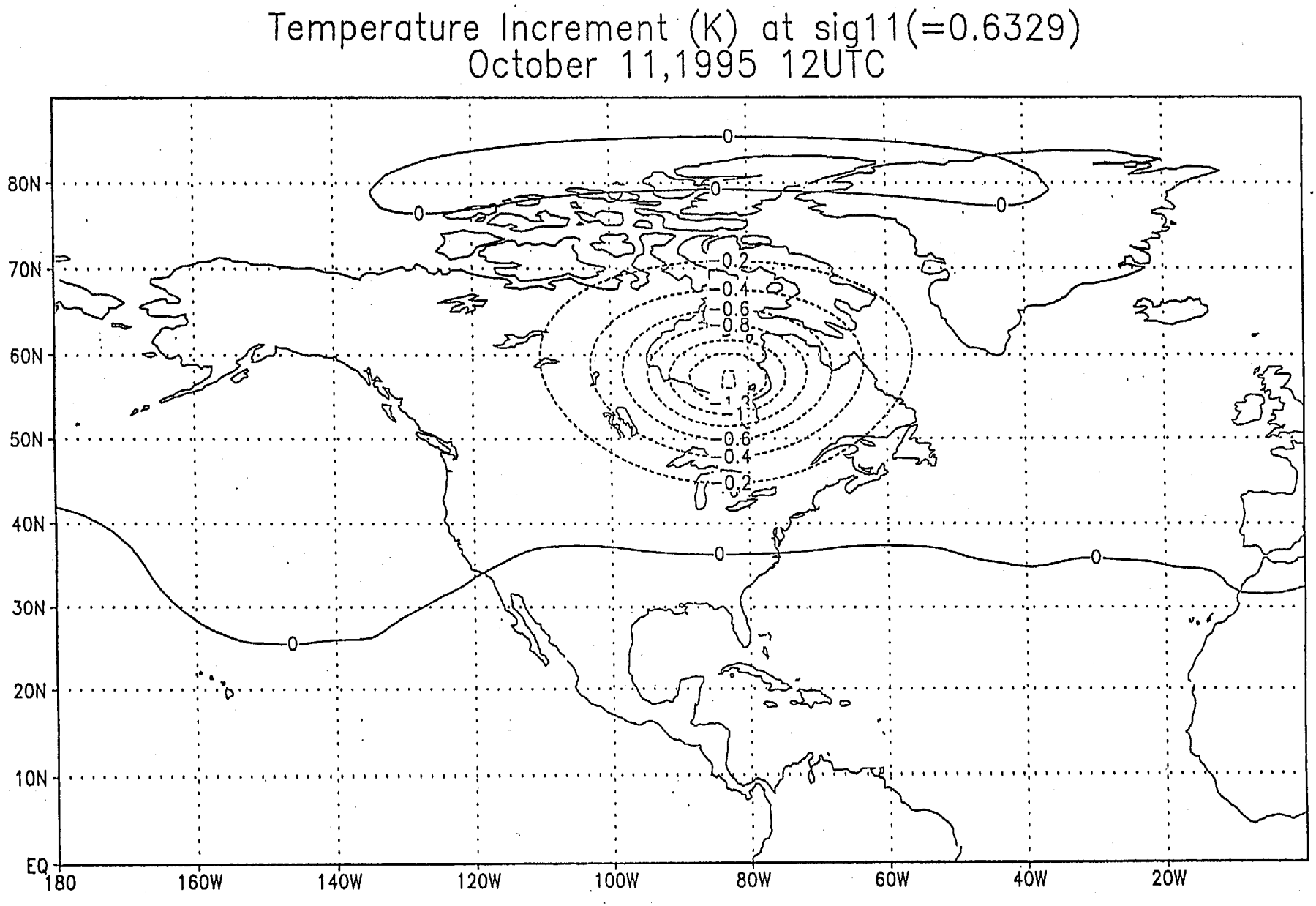

Fig. 5.7 : Analysis increment of temperature in EXP 1 at the sigma level of 0.6329 (the 11th layer from the bottom).

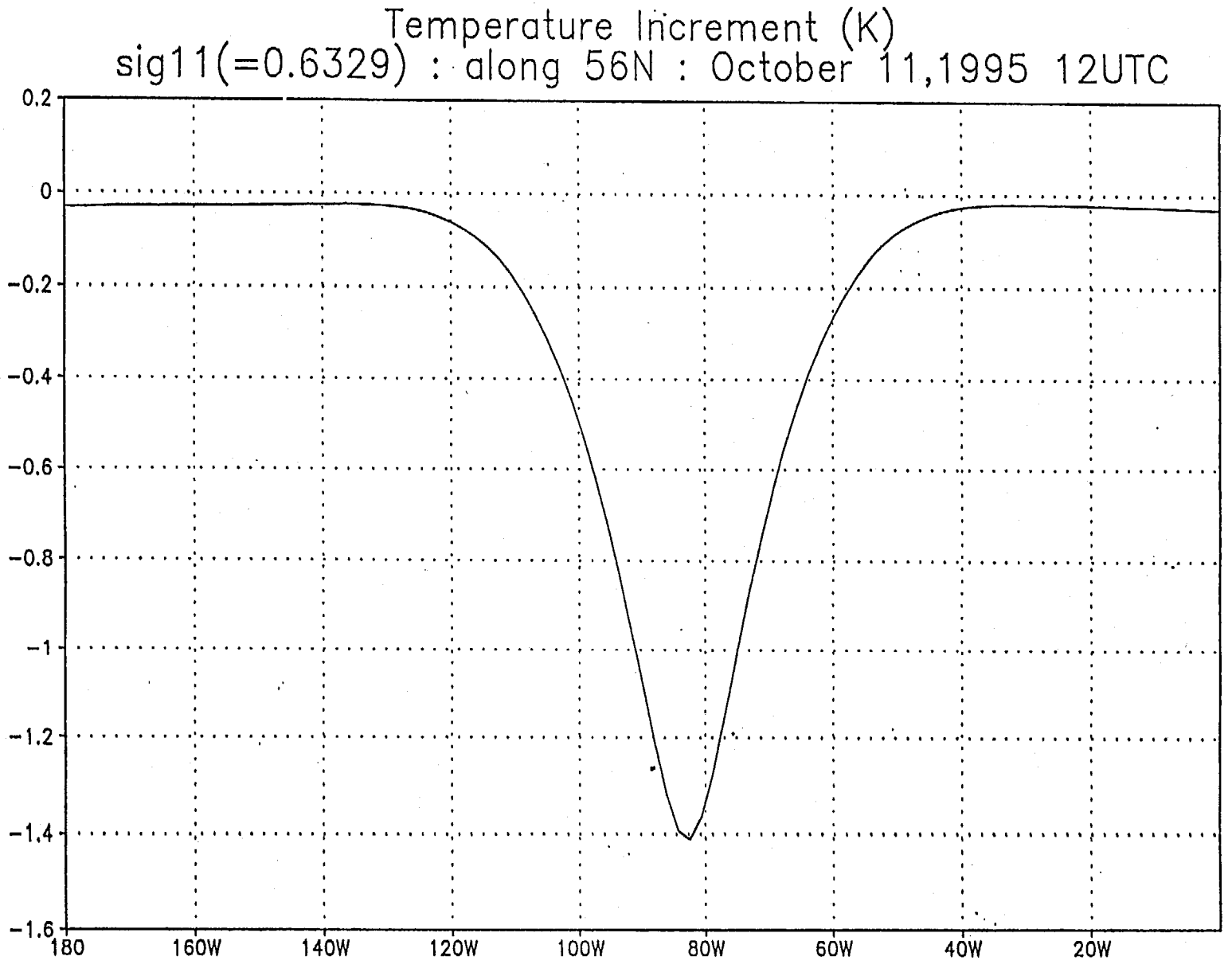

Fig. 5.8 : Analysis increment of temperature in EXP 1 at the sigma level of 0.6329 along 56N from the date line to the Greenwich meridian.

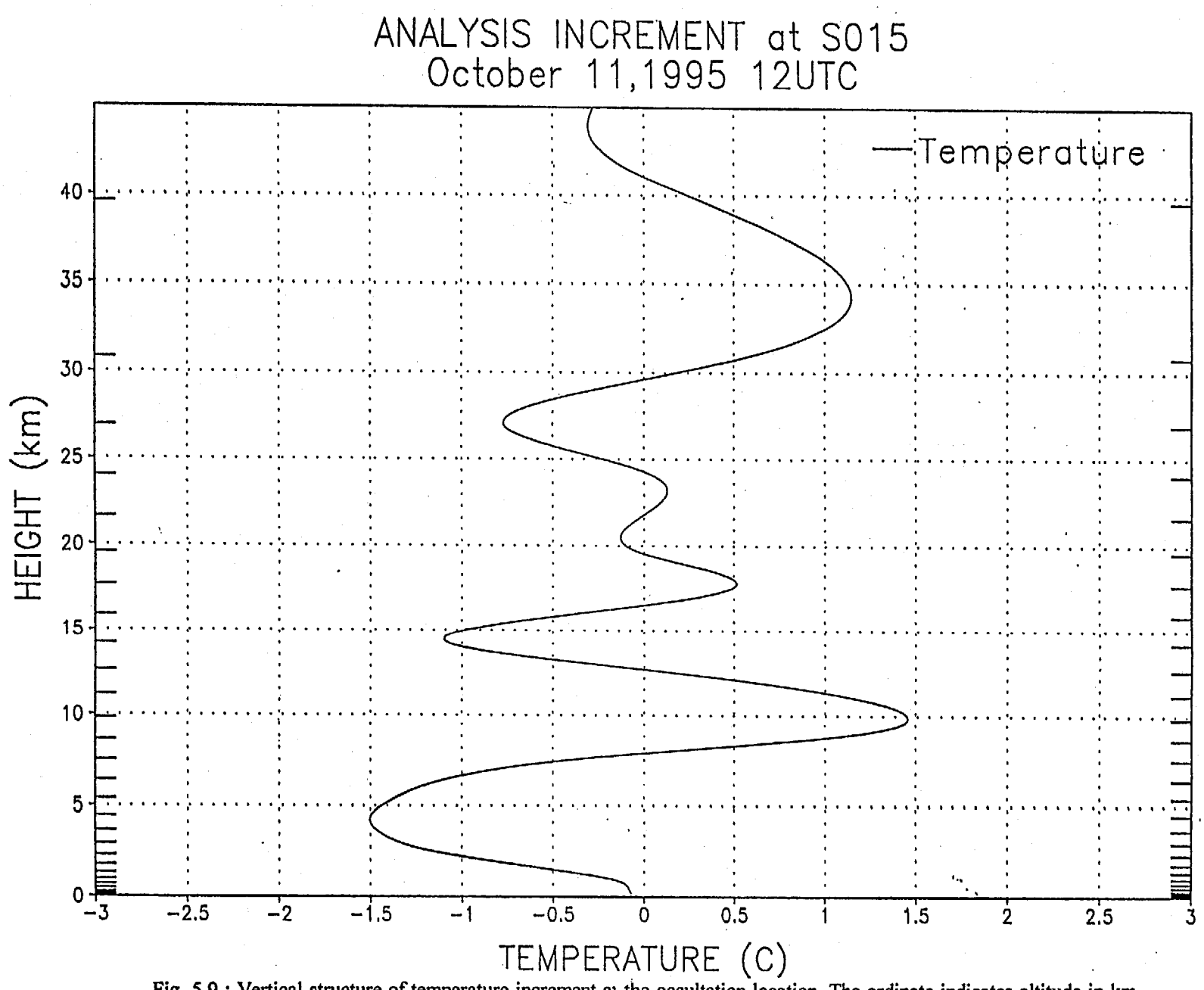

Fig. 5.9 : Vertical structure of temperature increment at the occultation location. The ordinate indicates altitude in km. The thick mark along the ordinate corresponds to the model layer.

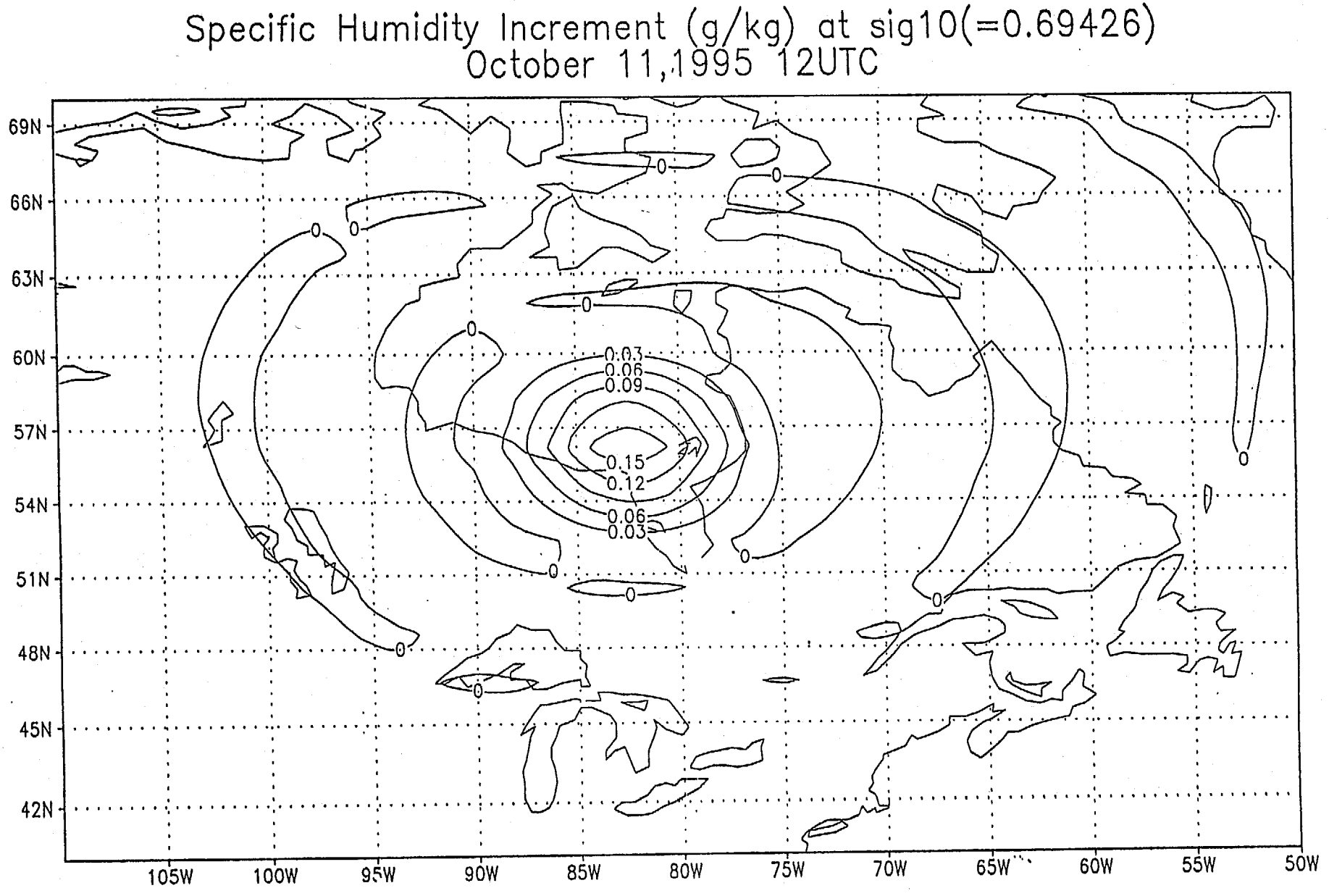

Fig. 5.10 : Analysis increment of specific humidity in EXP 1 at the sigma level of 0.69426 (the 10th layer from the bottom).

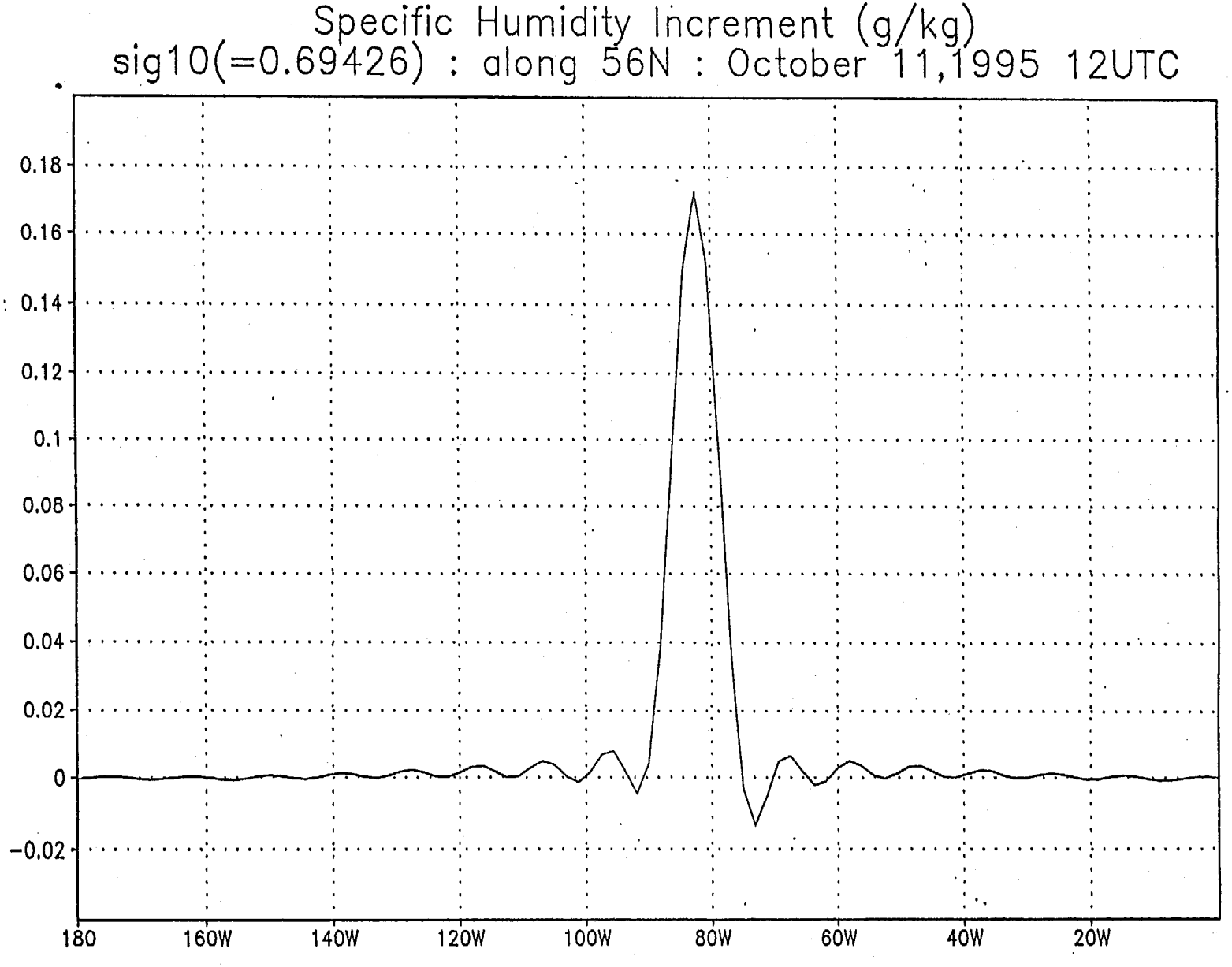

Fig. 5.11 : Analysis increment of specific humidity in EXP 1 at the sigma level of 0.69426 along 56N from the date line to the Greenwich meridian.

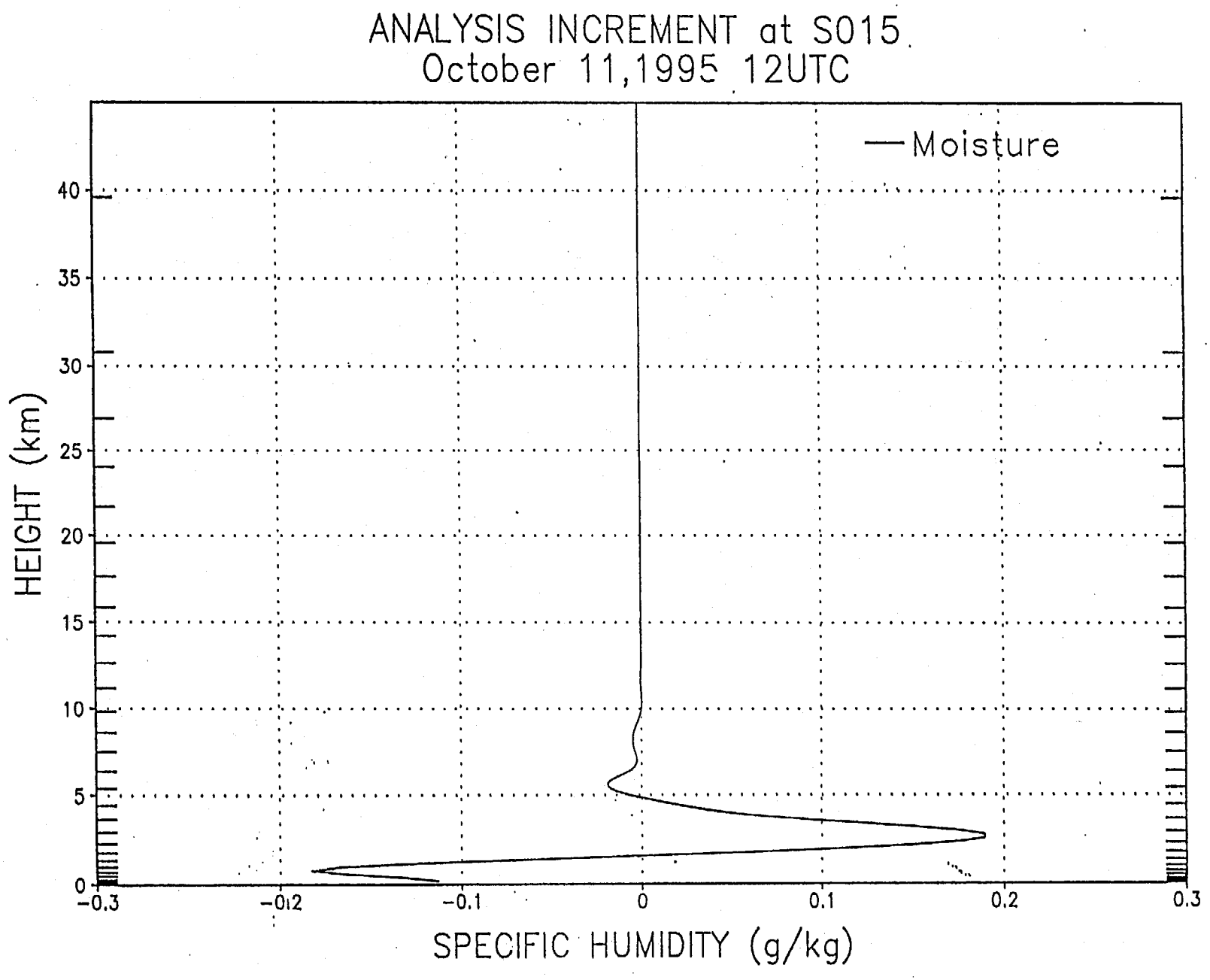

Fig. 5.12 : Vertical structure of specific humidity increment at the occultation location. The ordinate indicates altitude in km. The thick mark along the ordinate corresponds to the model layer.

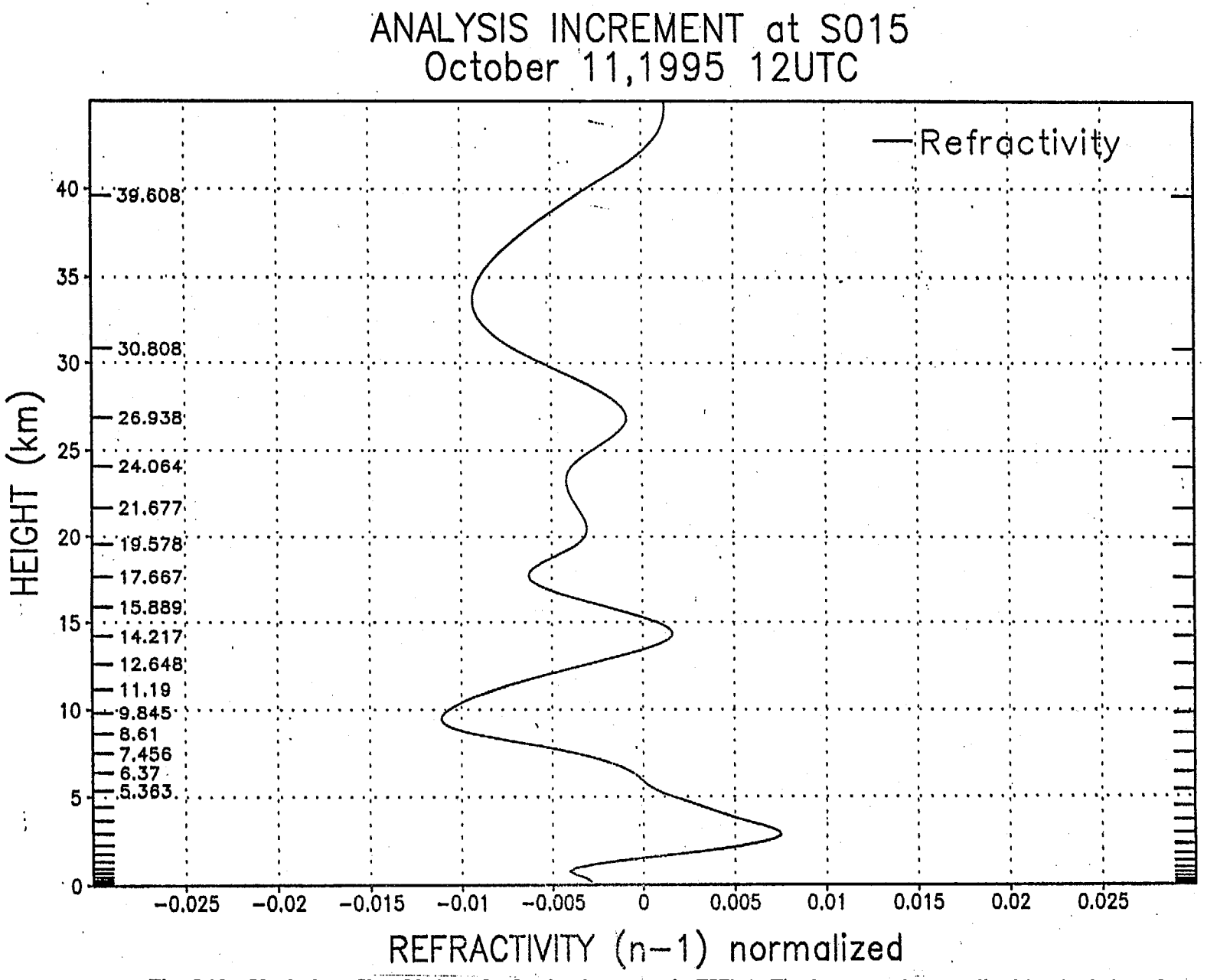

Fig. 5.13 : Vertical profile of index of refraction increment in EXP 1. The increment is normalized by the index of refraction of the background field at each vertical level.

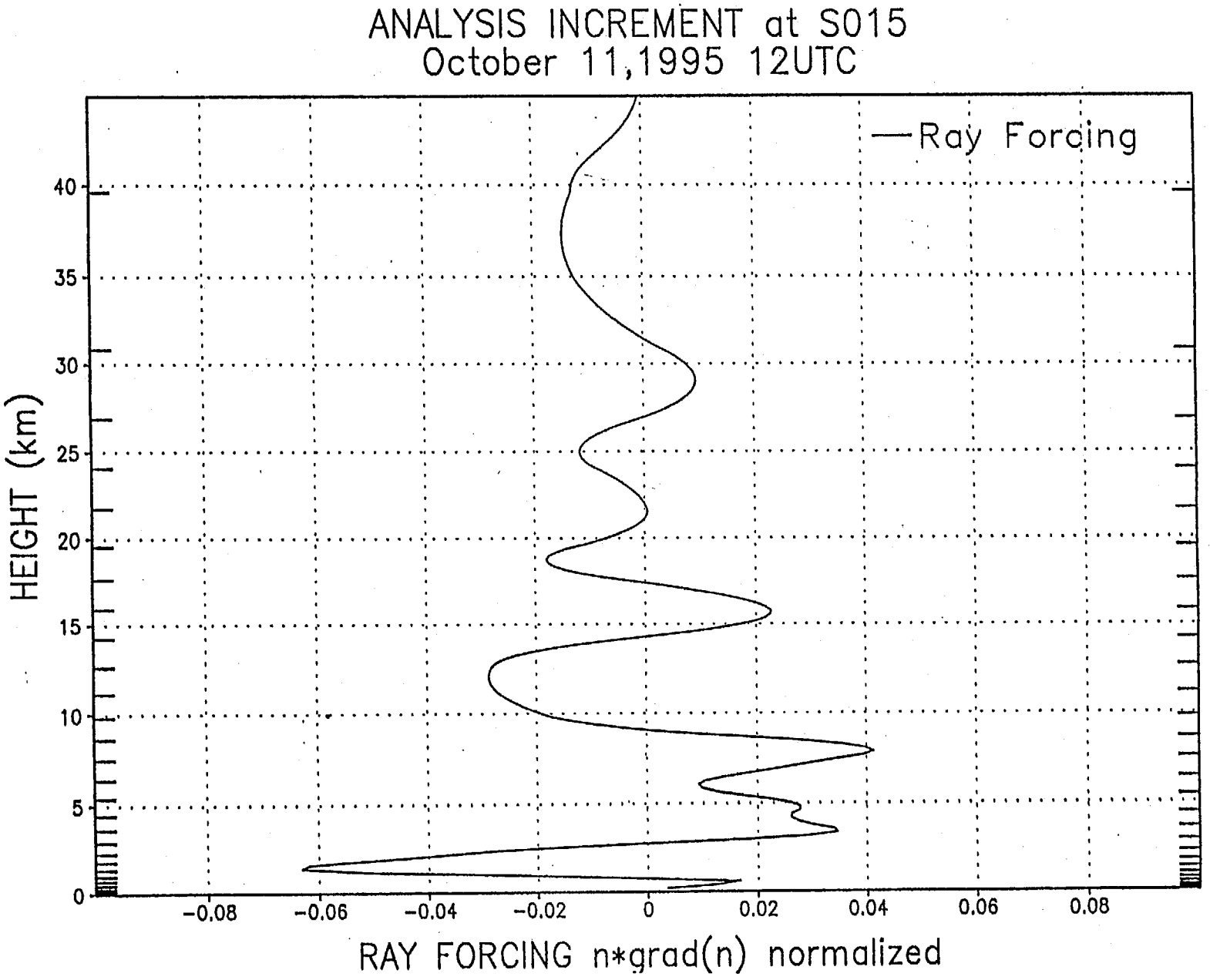

Fig. 5.14 : Change of the ray forcing term $(n\nabla n)$ during the assimilation procedure in EXP 1. The value is normalized by the ray forcing of the background field at each vertical level.

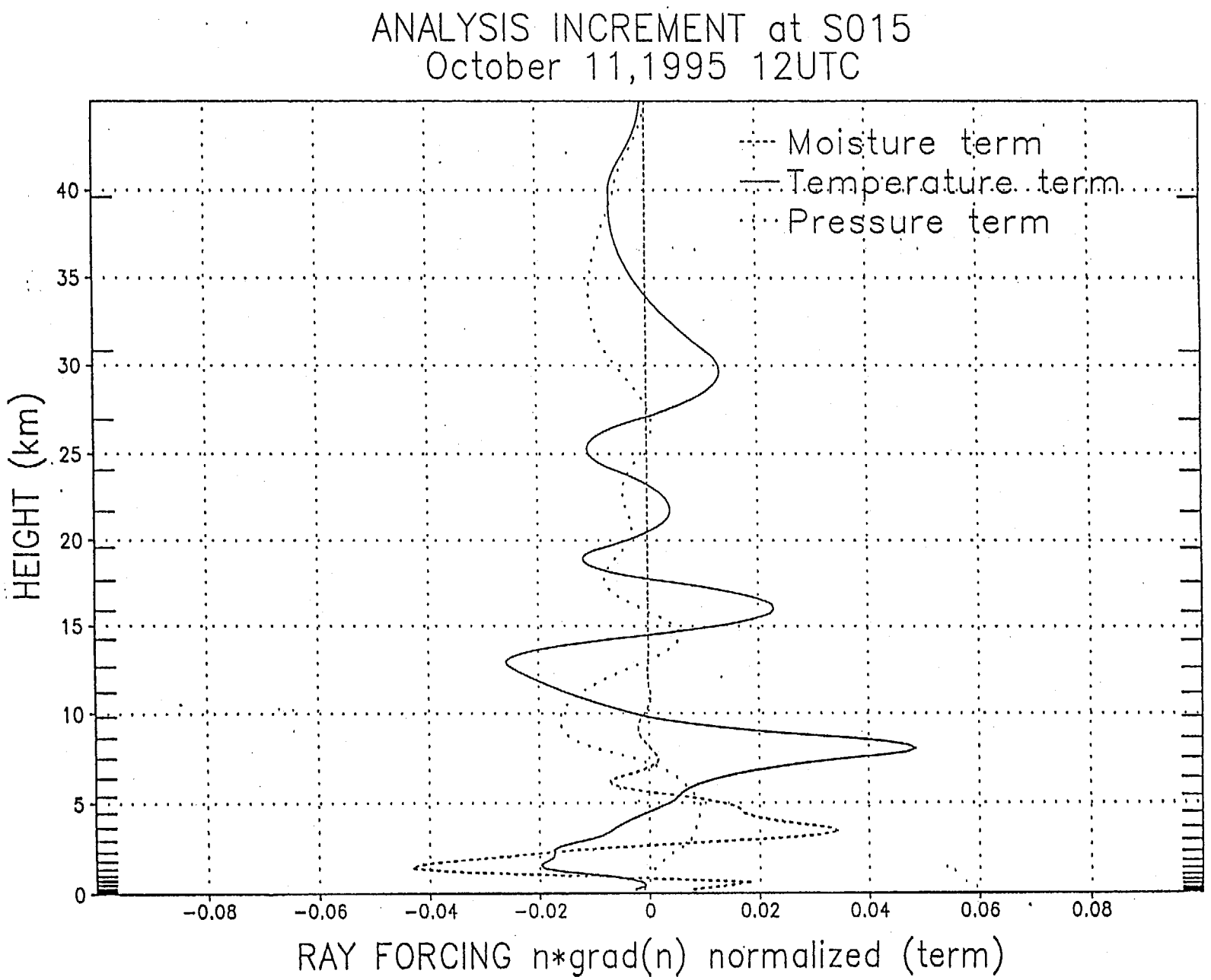

Fig. 5.15 : Change of the three components of the forcing term (see eq. (4.1)) during the assimilation procedure in EXP 1. The value is normalized by the ray forcing of the background field at each vertical level.

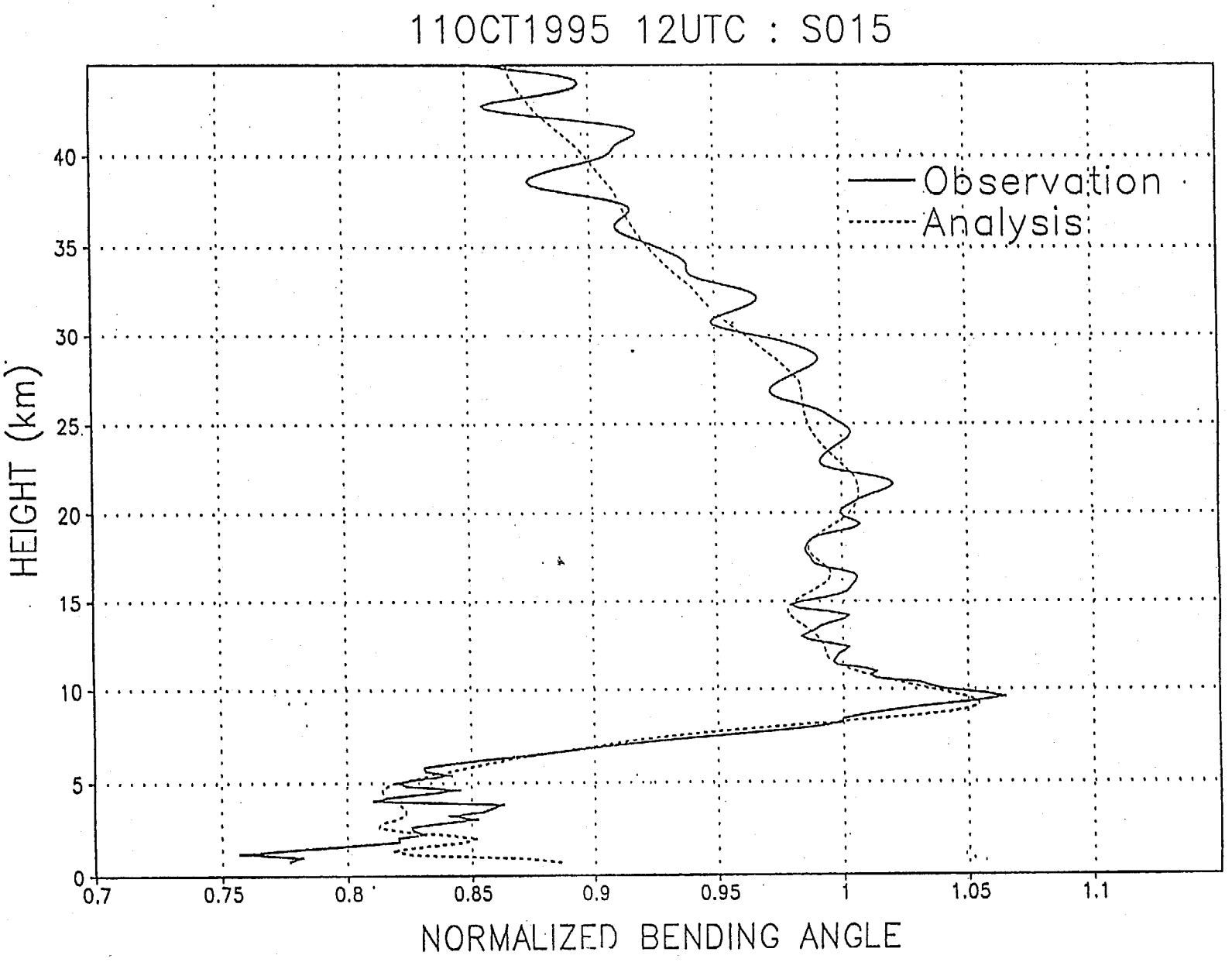

Fig. 5.16 : Simulated bending angle from the analysis in EXP 1. The observation is also superimposed as Fig. 5.2.

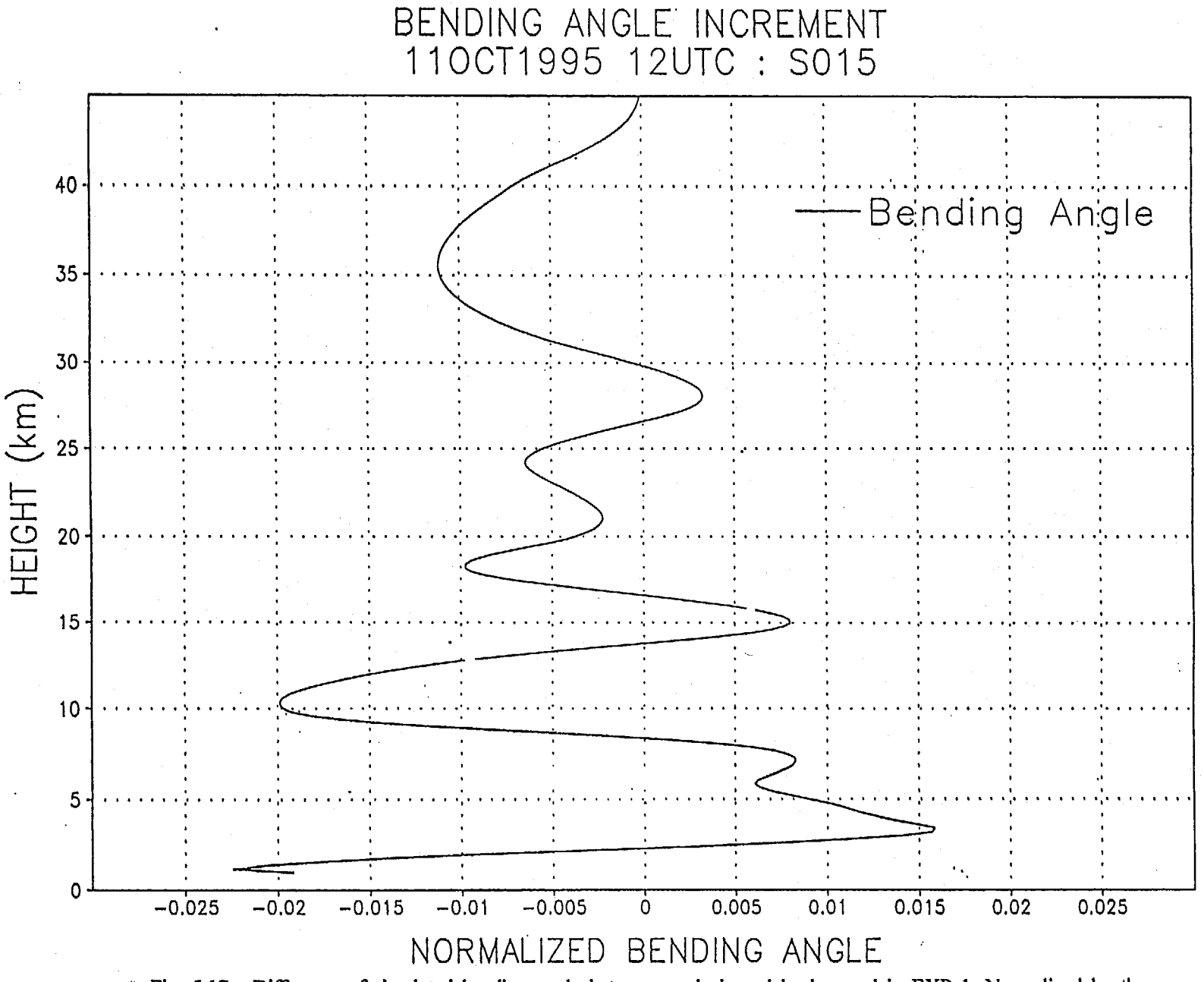

Fig. 5.17 : Difference of simulated bending angle between analysis and background in EXP 1. Normalized by the reference profile ε_r.

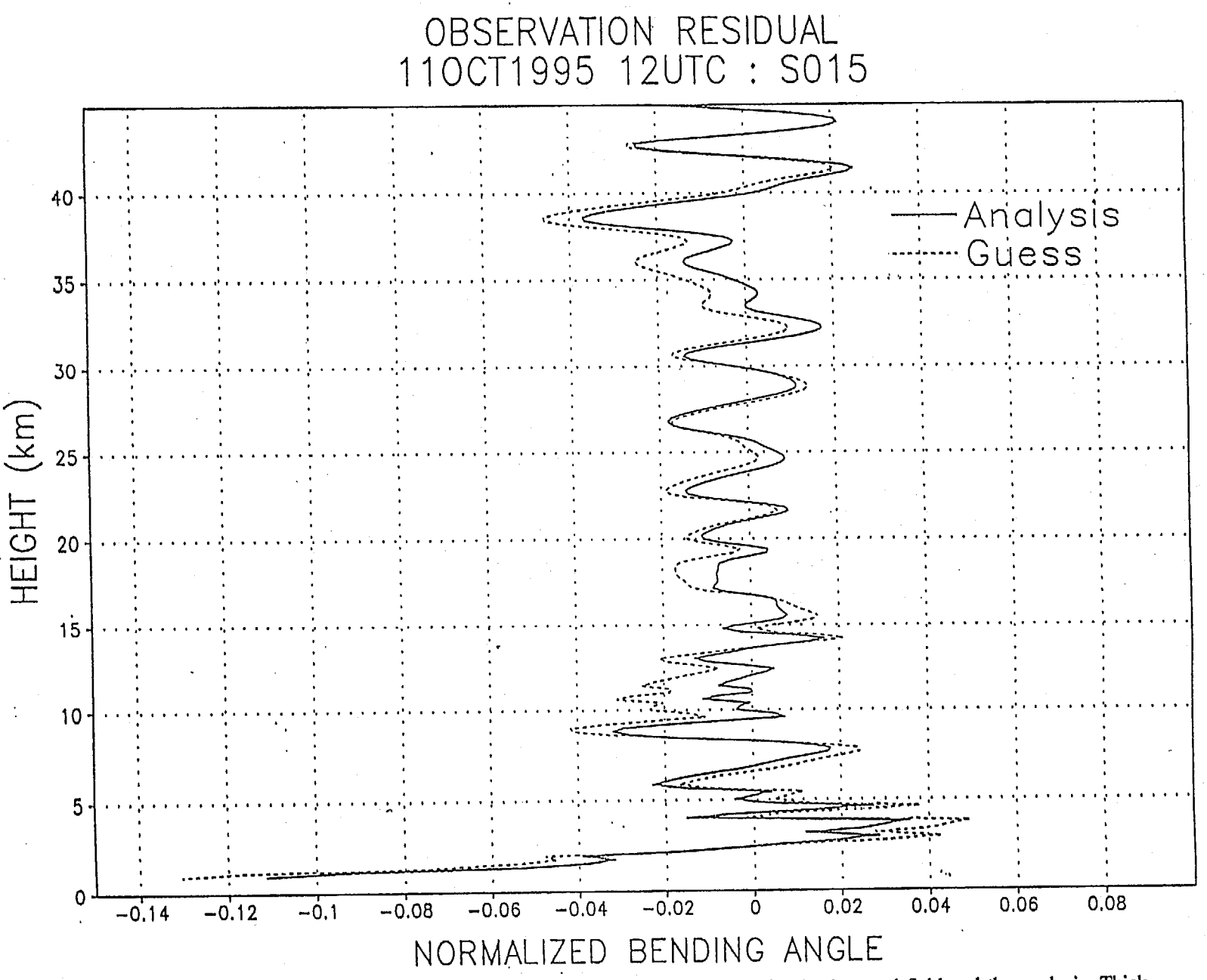

Fig. 5.18 : Observational residuals of bending angle obtained from both the background field and the analysis. Thick solid line is for the analysis field. Thin dashed line is for the background field. Normalized by the reference profile ε_r .

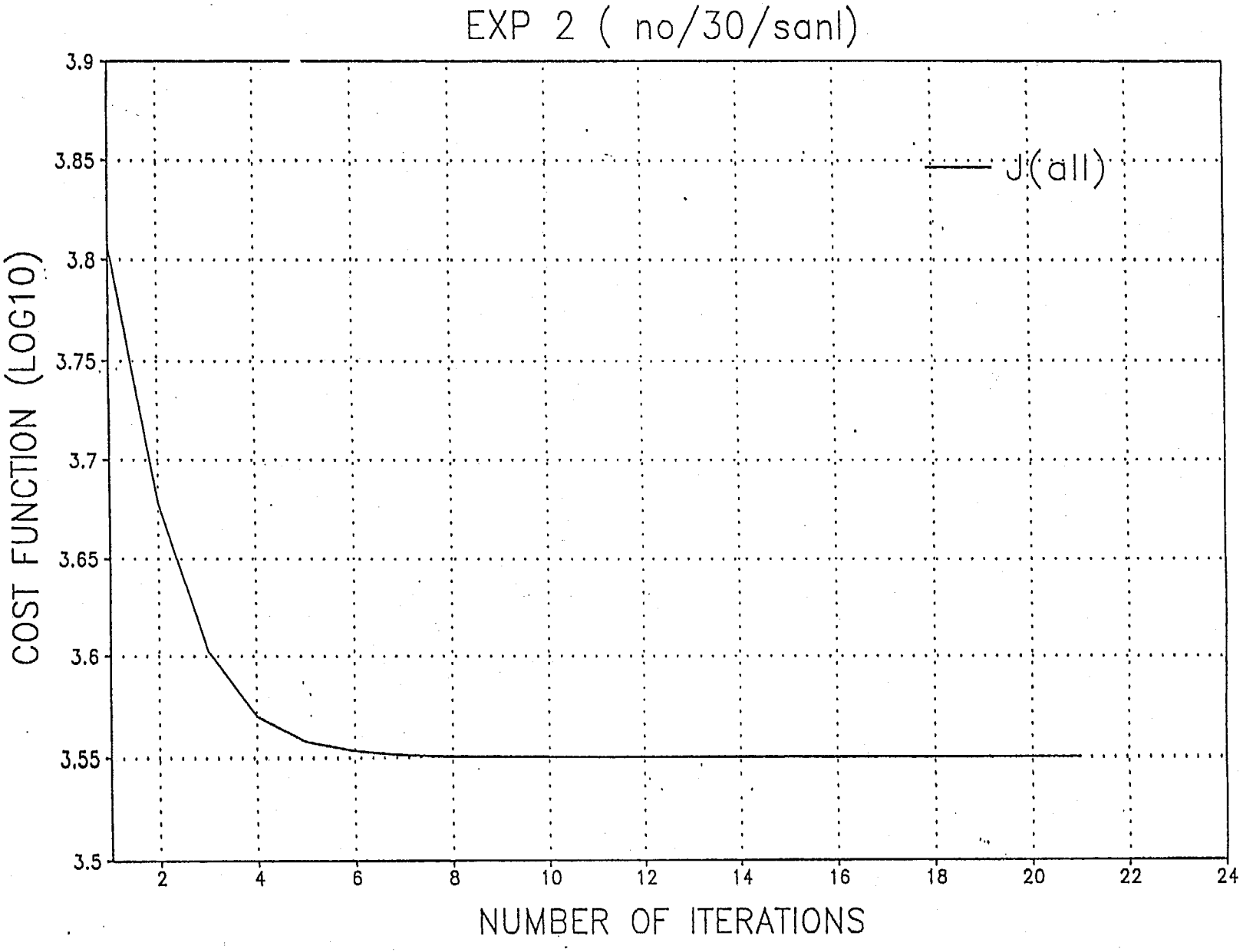

Fig. 5.19 : Variation of cost function during the minimization procedure in EXP 2 with respect to the number of iterations.

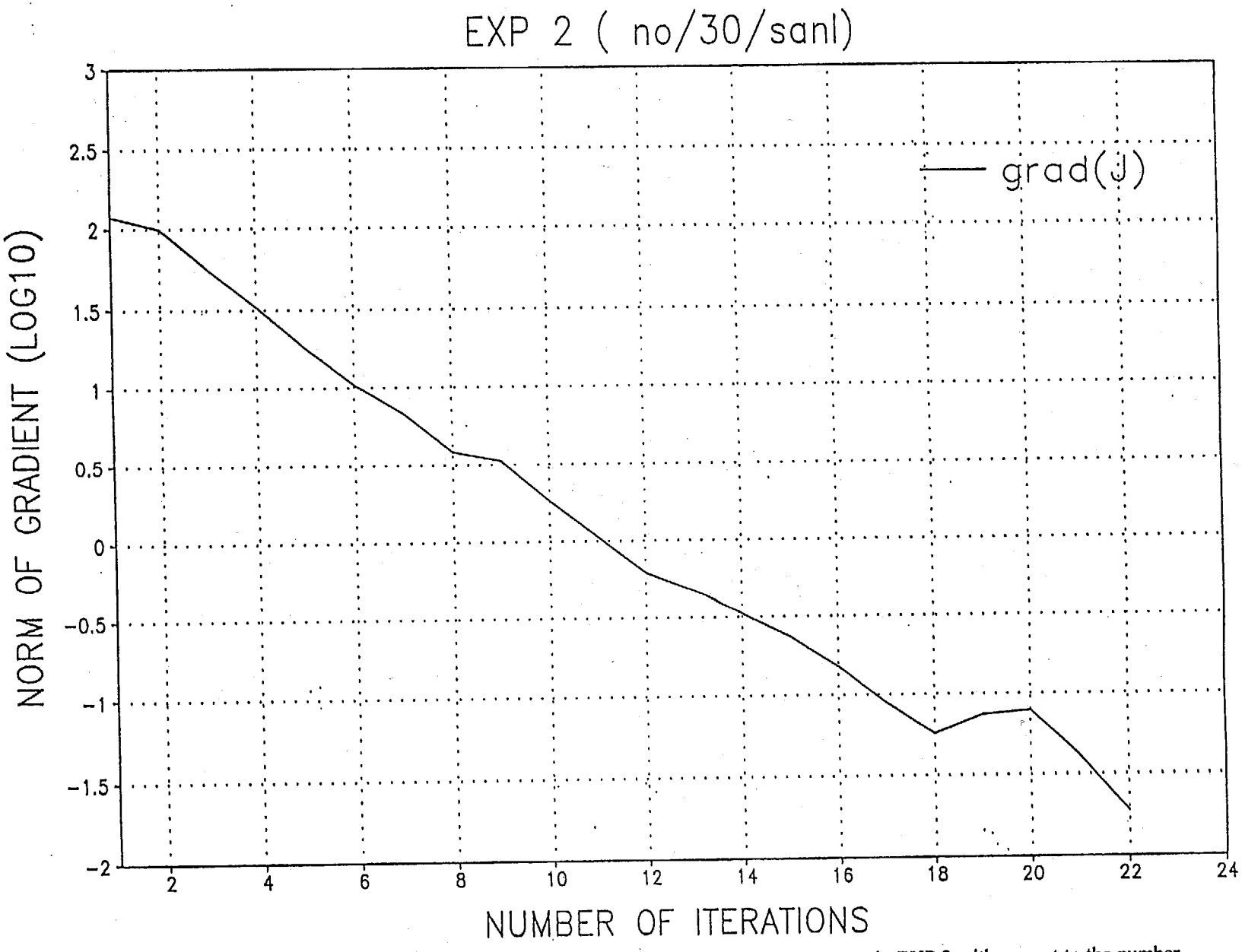

Fig. 5.20 : Norm of gradient of the cost function during the minimization procedure in EXP 2 with respect to the number of iterations. The iterations after the 18th correspond to the second outer iteration.

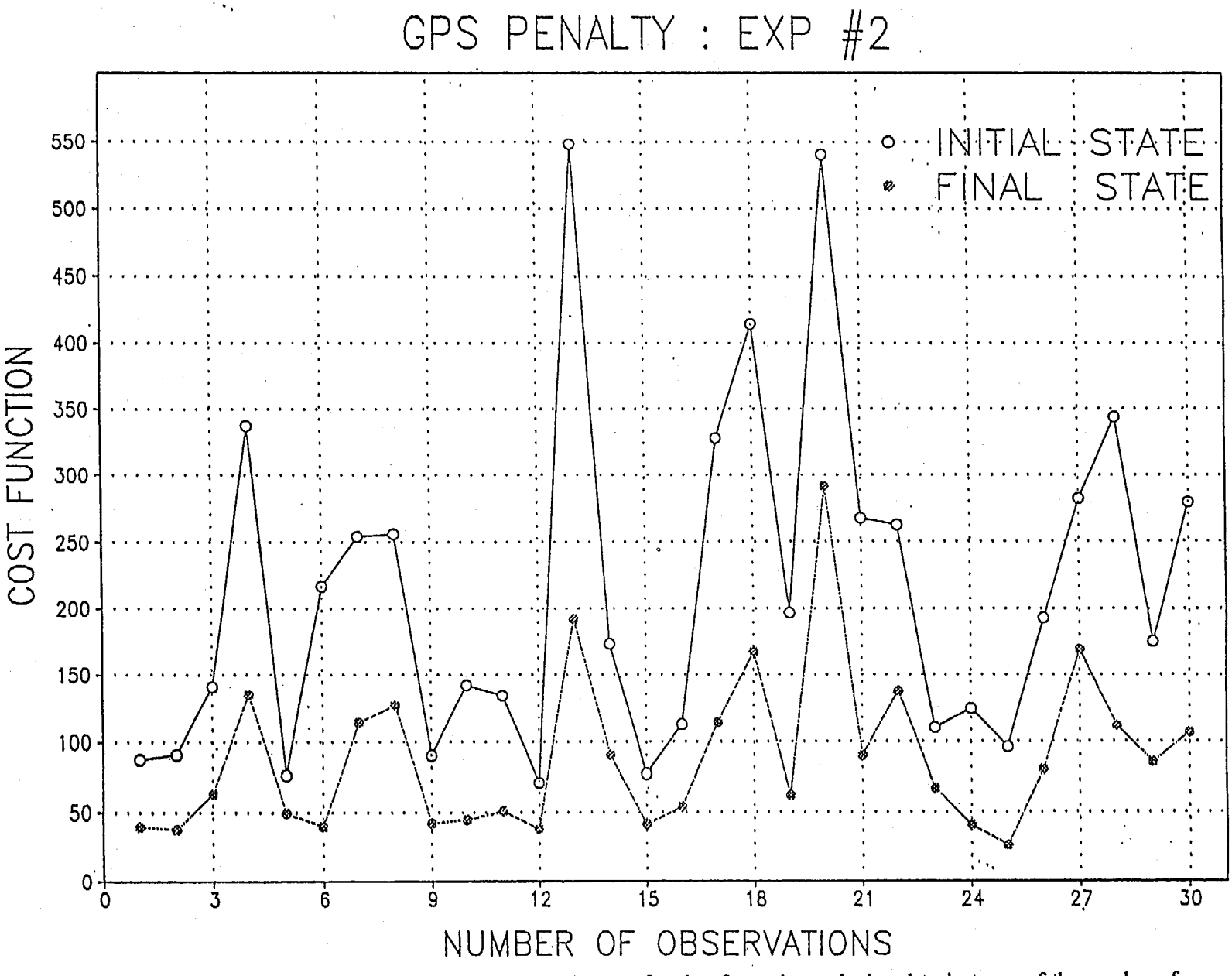

Fig. 5.21 : Values of the individual terms of the cost function for each occultation data in terms of the number of observations. Open circle indicates initial value of the penalty and closed circle denotes the value at the final state.

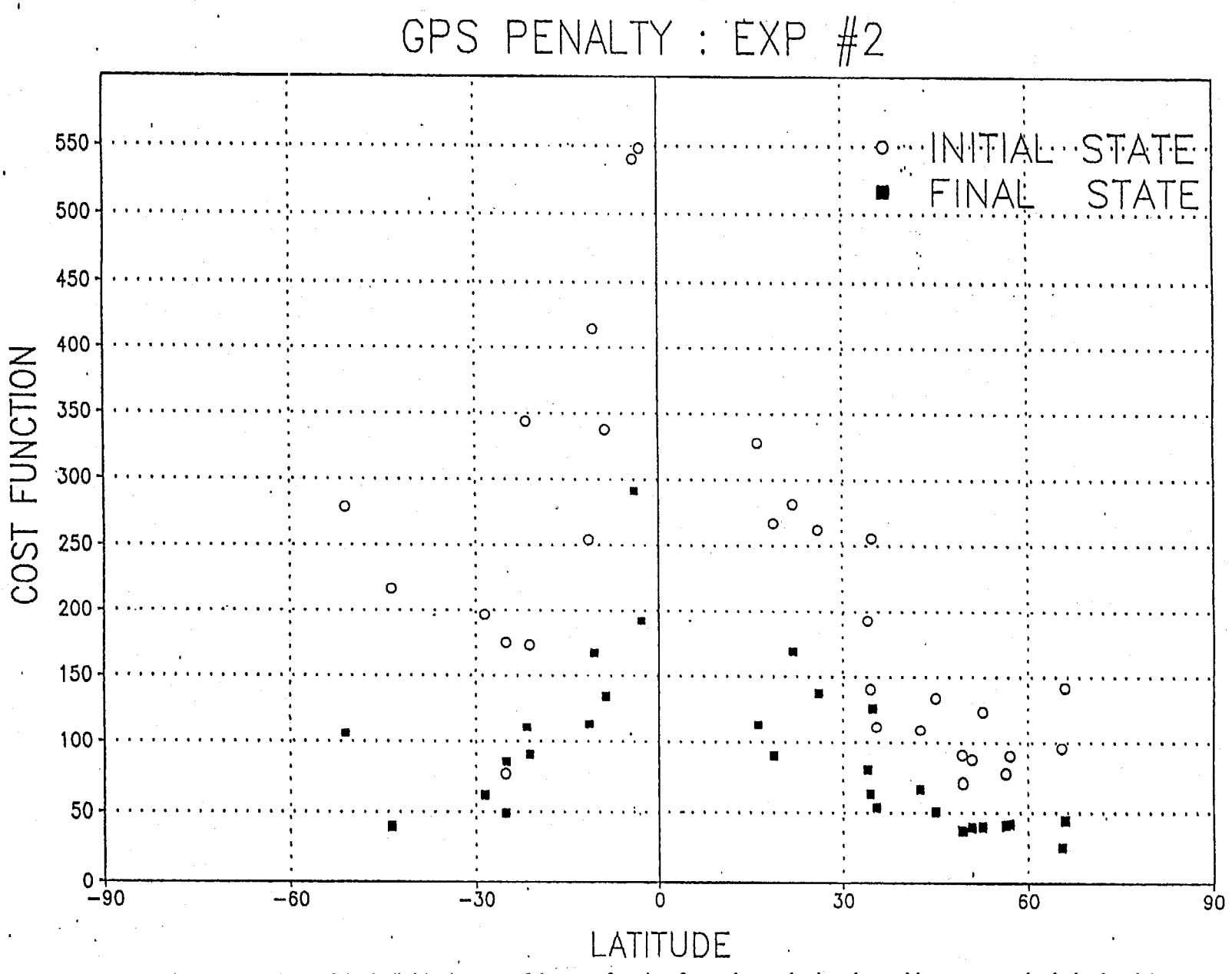

Fig. 5.22 : Values of the individual terms of the cost function for each occultation data with respect to the latitude of the occultation event. Open circle indicates initial value of the penalty and closed square denotes the value at the final state.

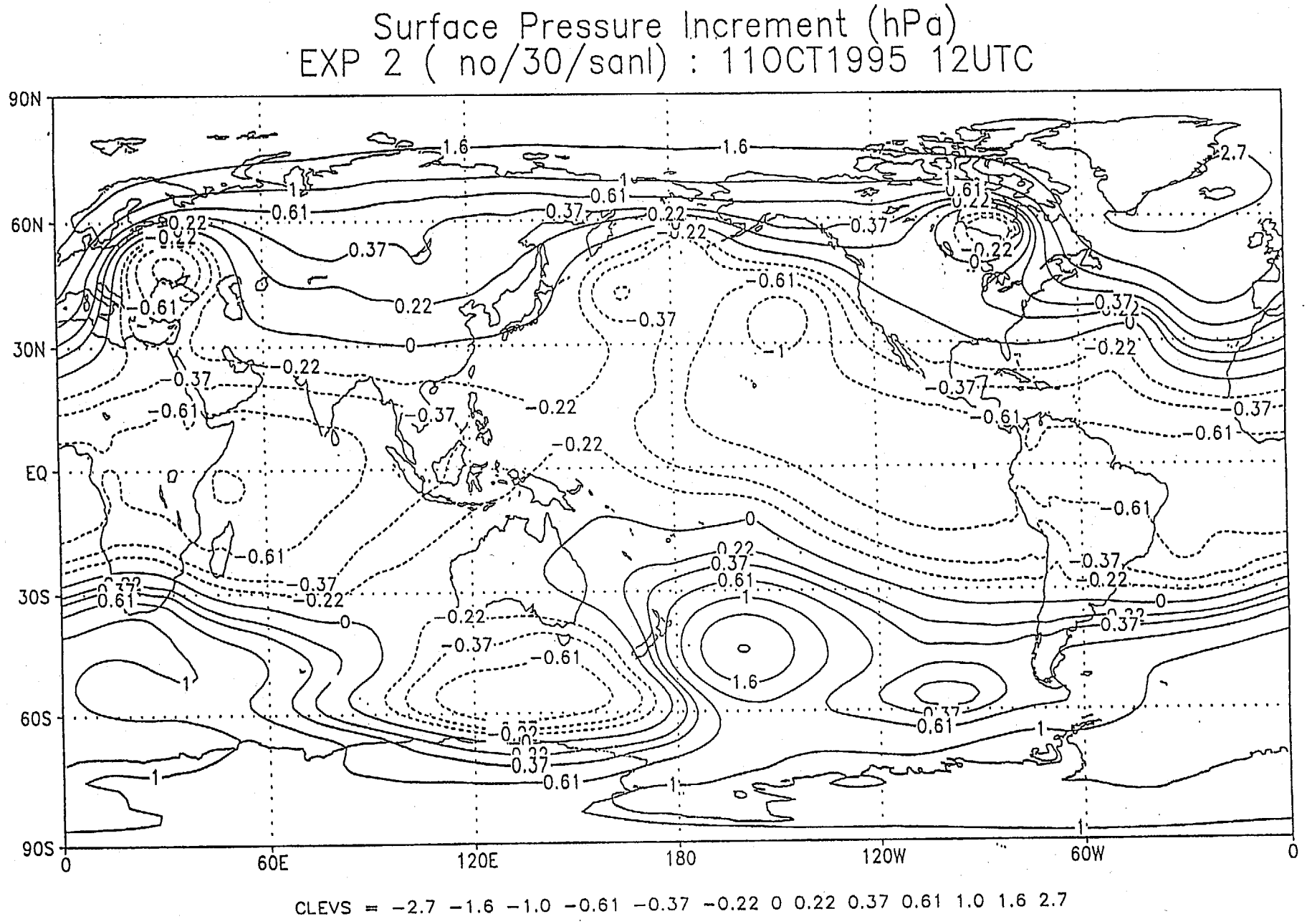

Fig. 5.23 : Analysis increment of surface pressure in EXP 2.

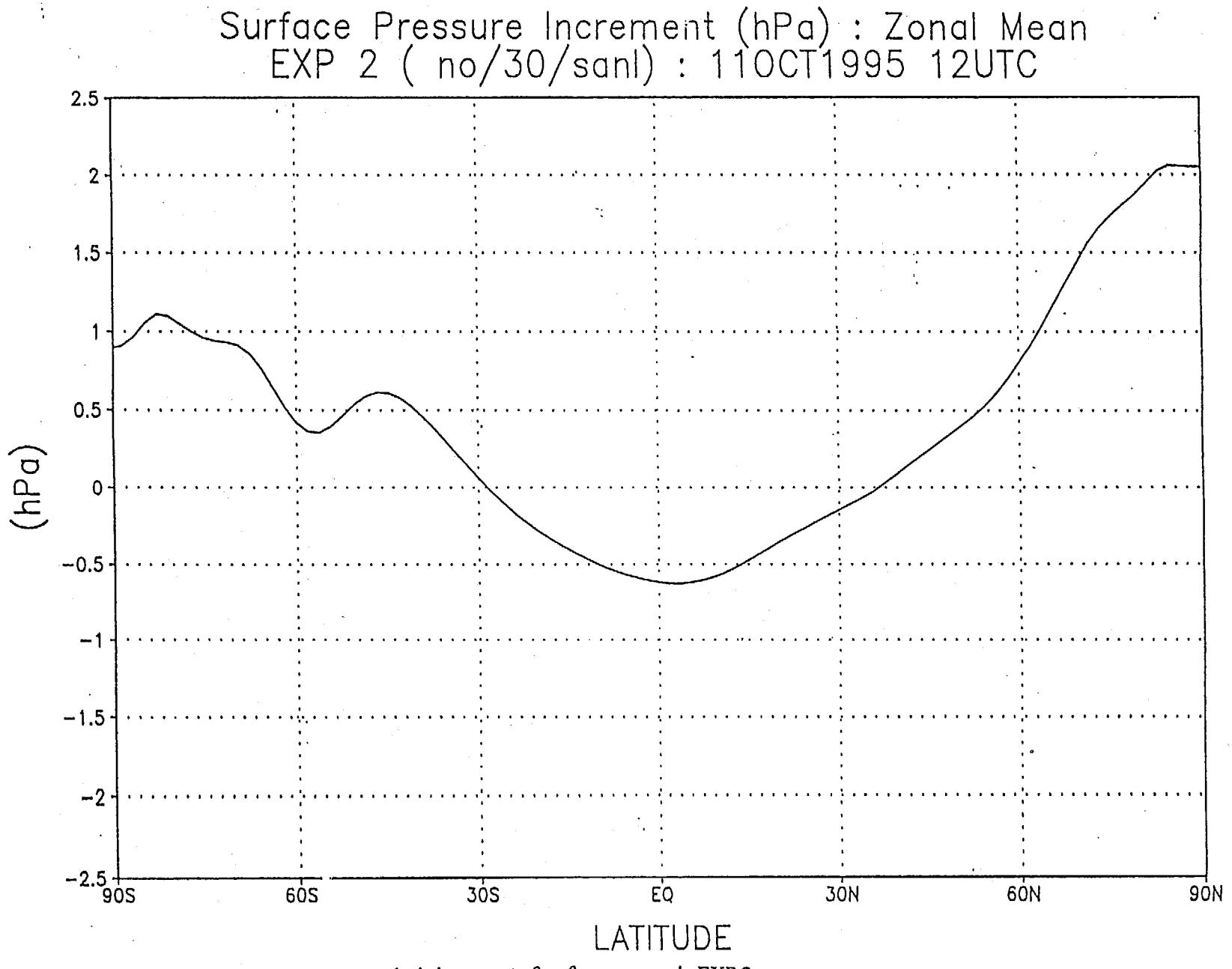

Fig. 5.24 : Zonal mean analysis increment of surface pressure in EXP 2.

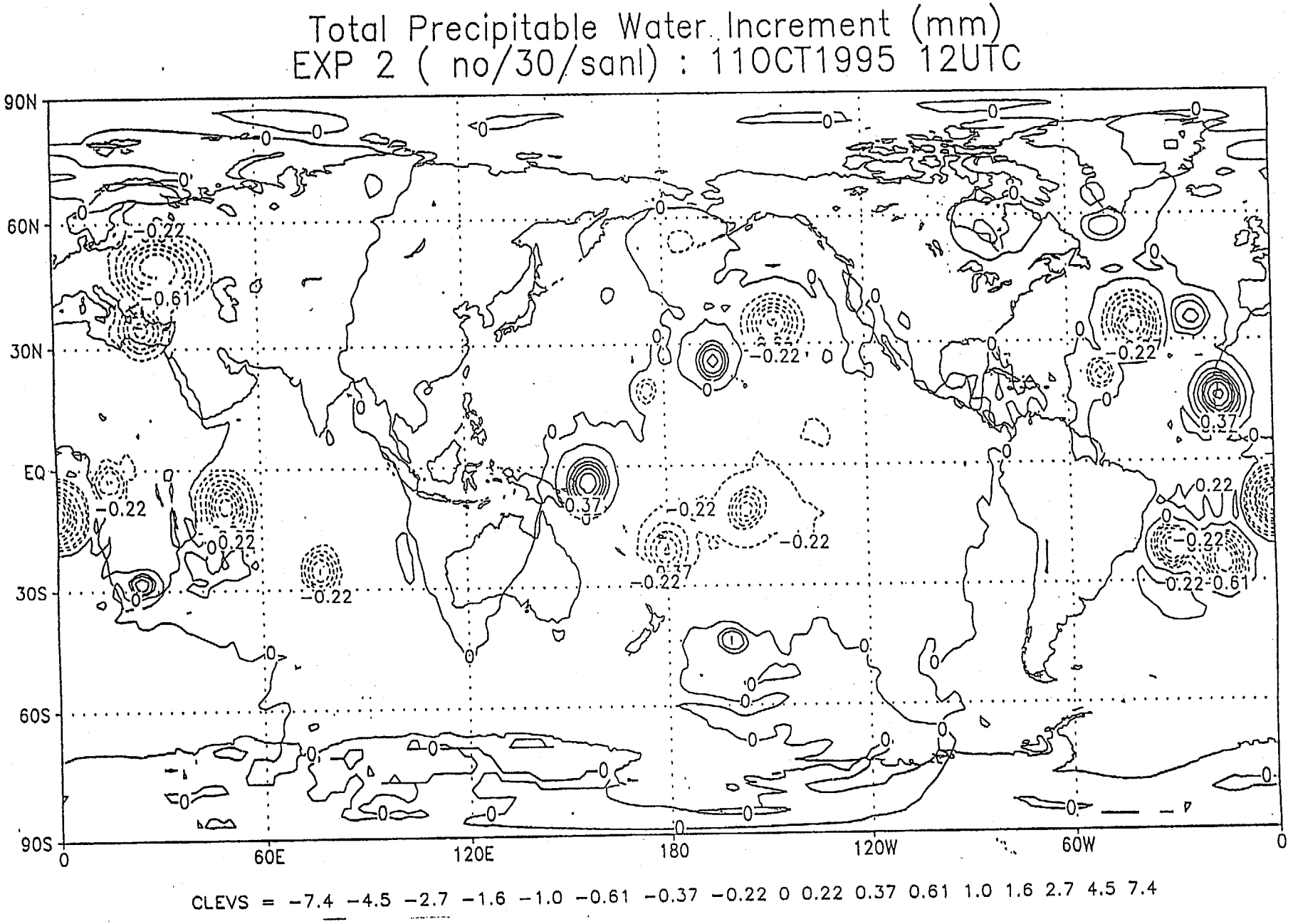

Fig. 5.25 : Analysis increment of total precipitable water in EXP 2.

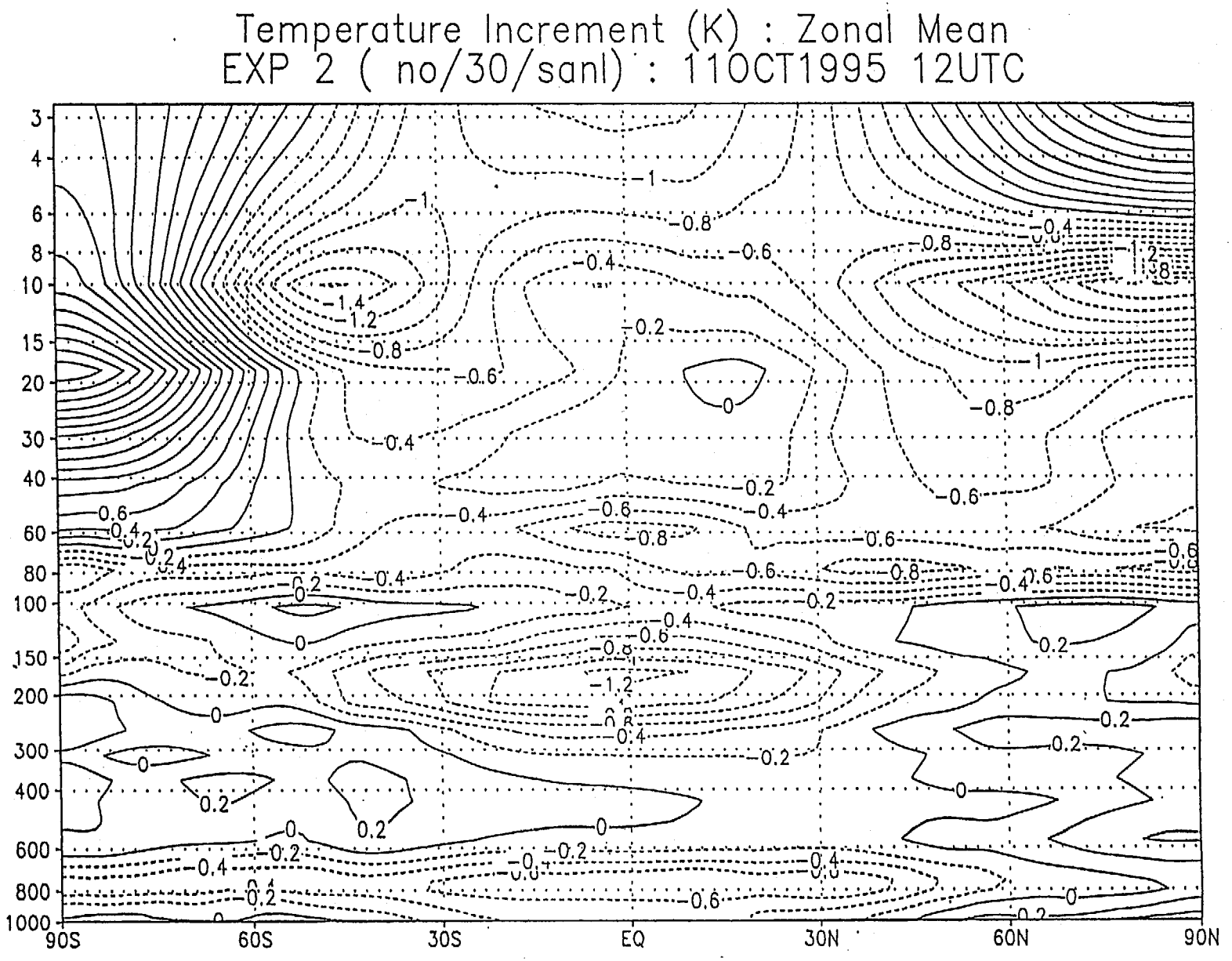

Fig. 5.26 : Zonal mean analysis increment of temperature in EXP 2.

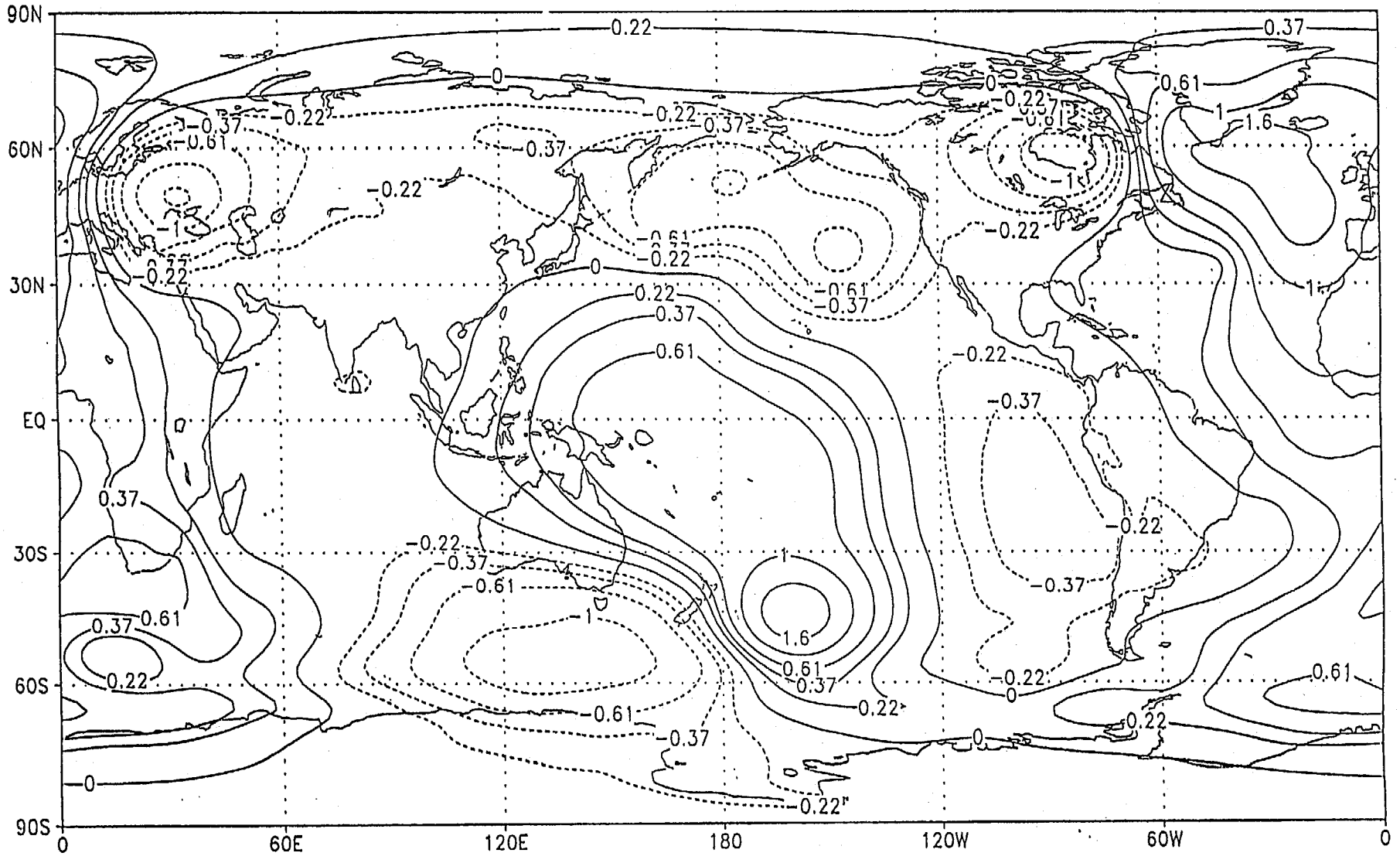

Fig. 5.27 : Analysis increment of surface pressure for EXP 2A in which the acceleration of gravity is set to constant. Other conditions are identical with those in EXP 2.

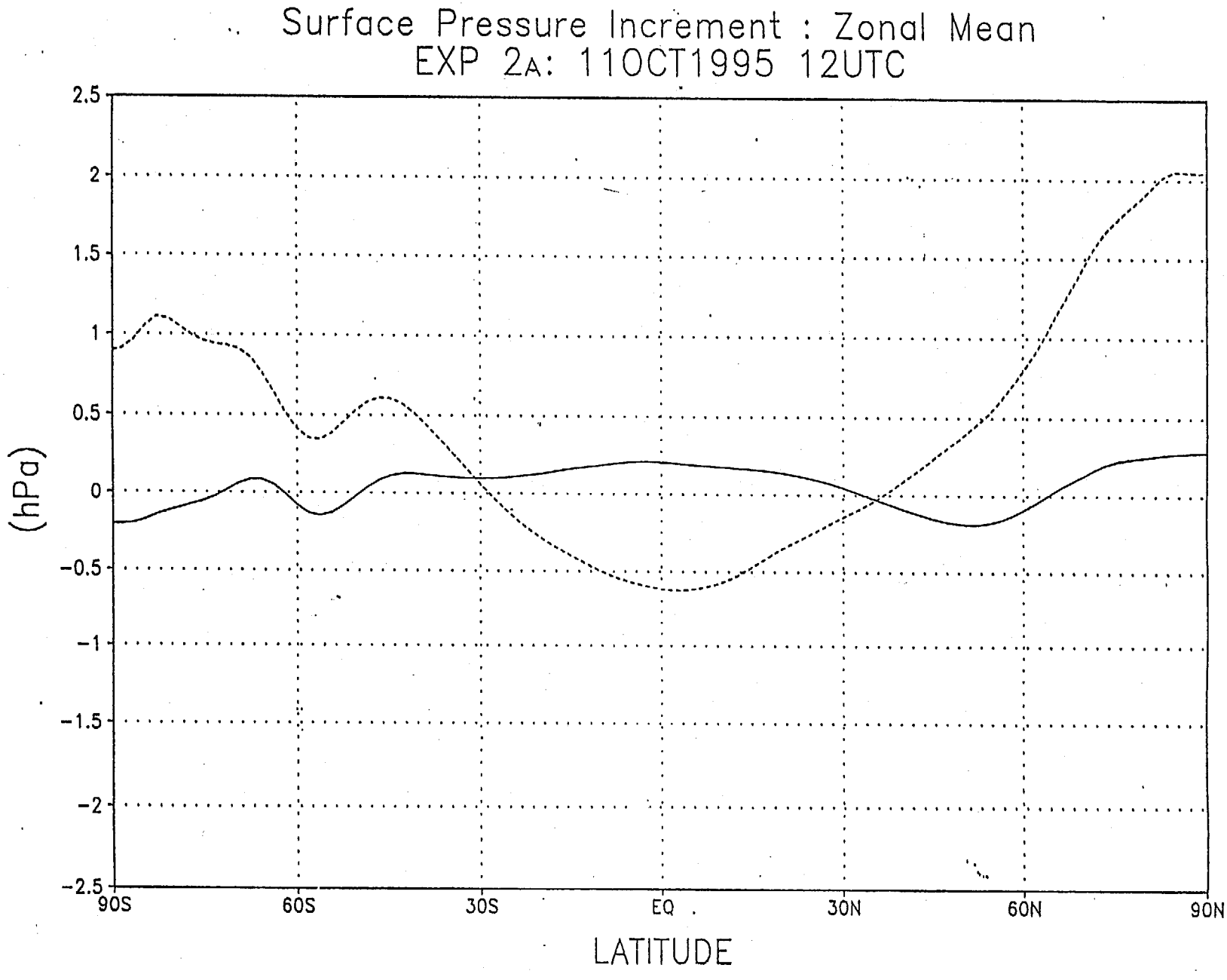

Fig. 5.28 : Zonal mean analysis increment of surface pressure for EXP 2A (solid) and for EXP 2 (dashed). Other conditions are identical with those in EXP 2.

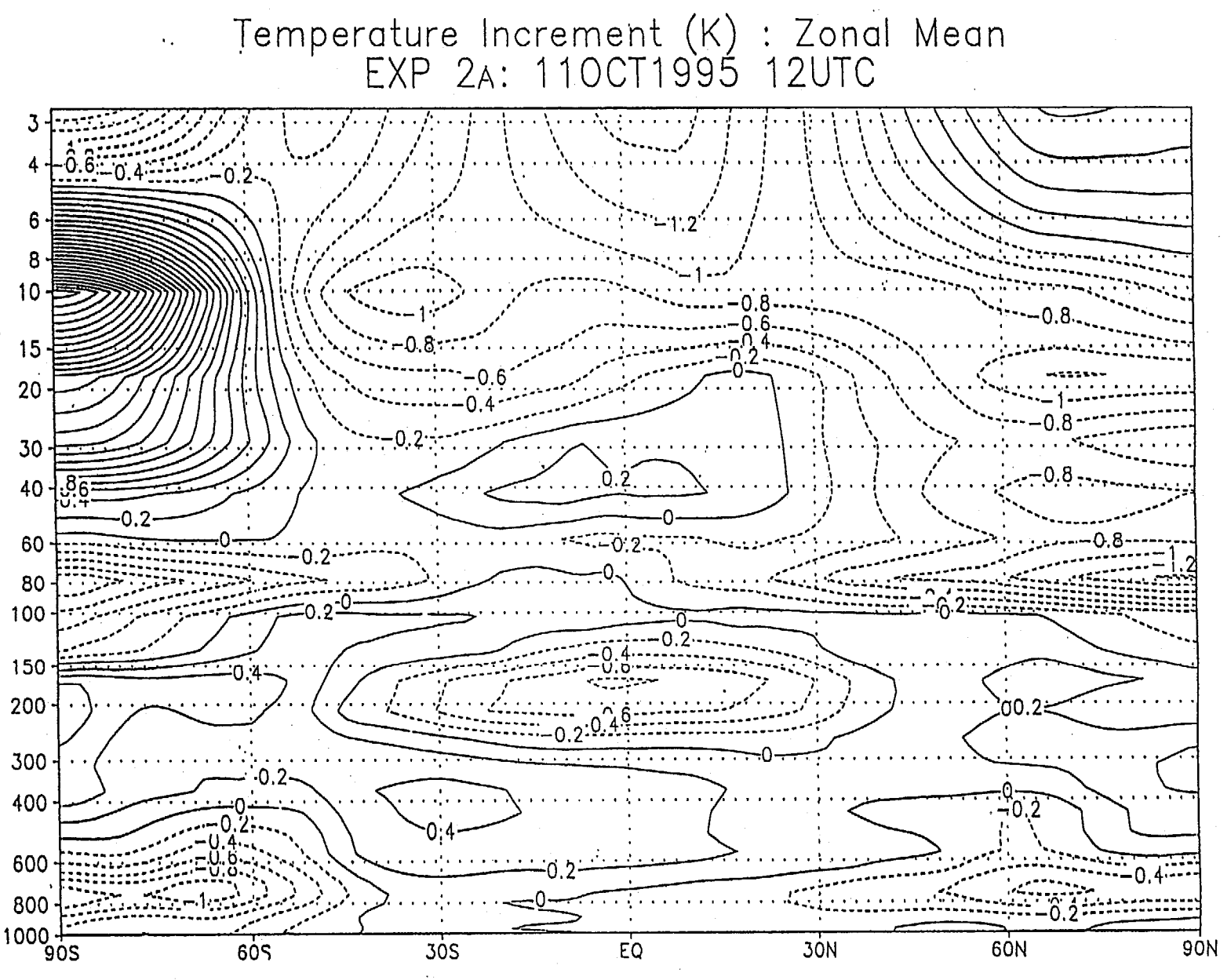

Fig. 5.29 : Zonal mean analysis increment of temperature for EXP 2A in which the acceleration of gravity is set to constant. Other conditions are identical with those in EXP 2.

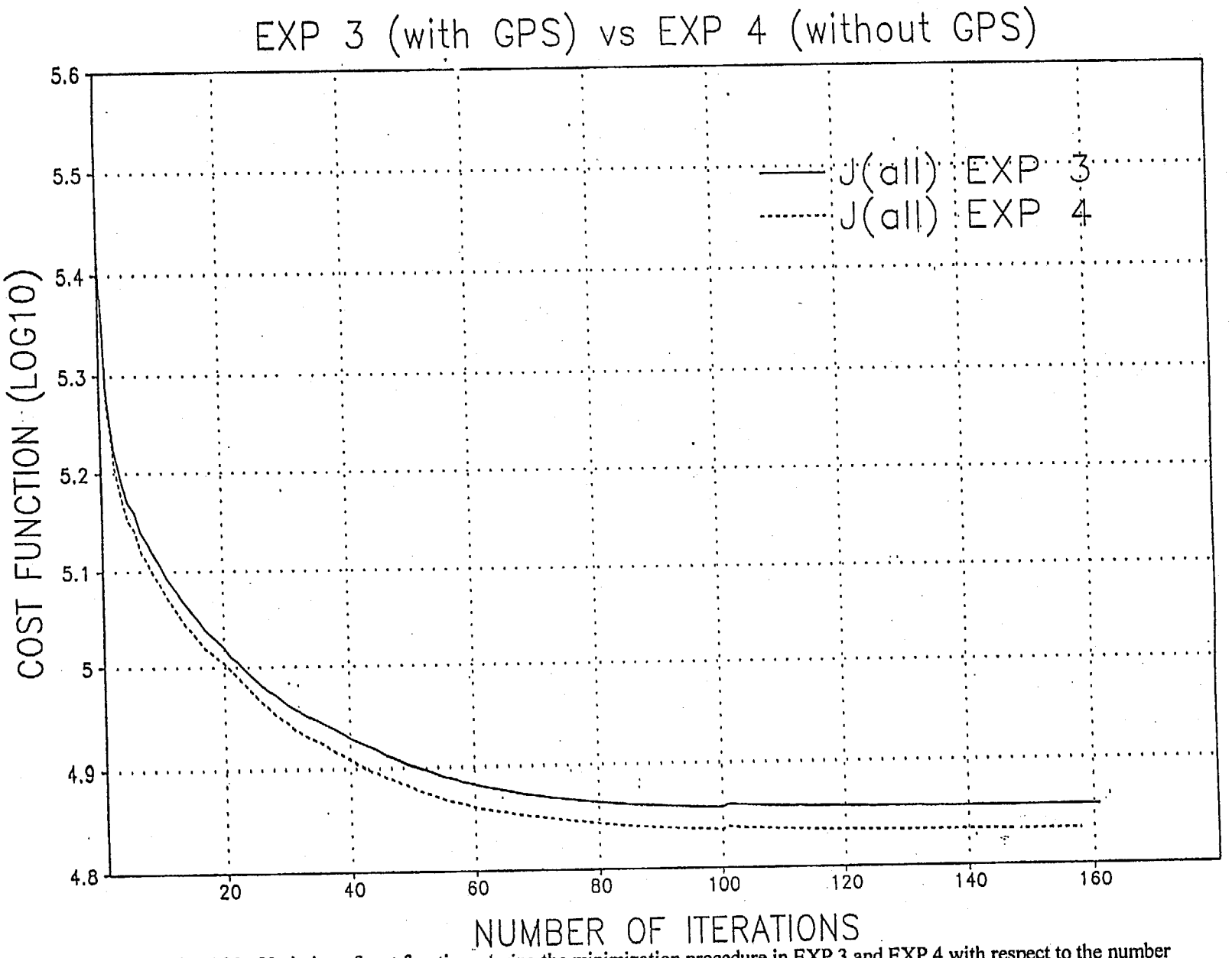

Fig. 5.30 : Variation of cost functions during the minimization procedure in EXP 3 and EXP 4 with respect to the number of iterations.

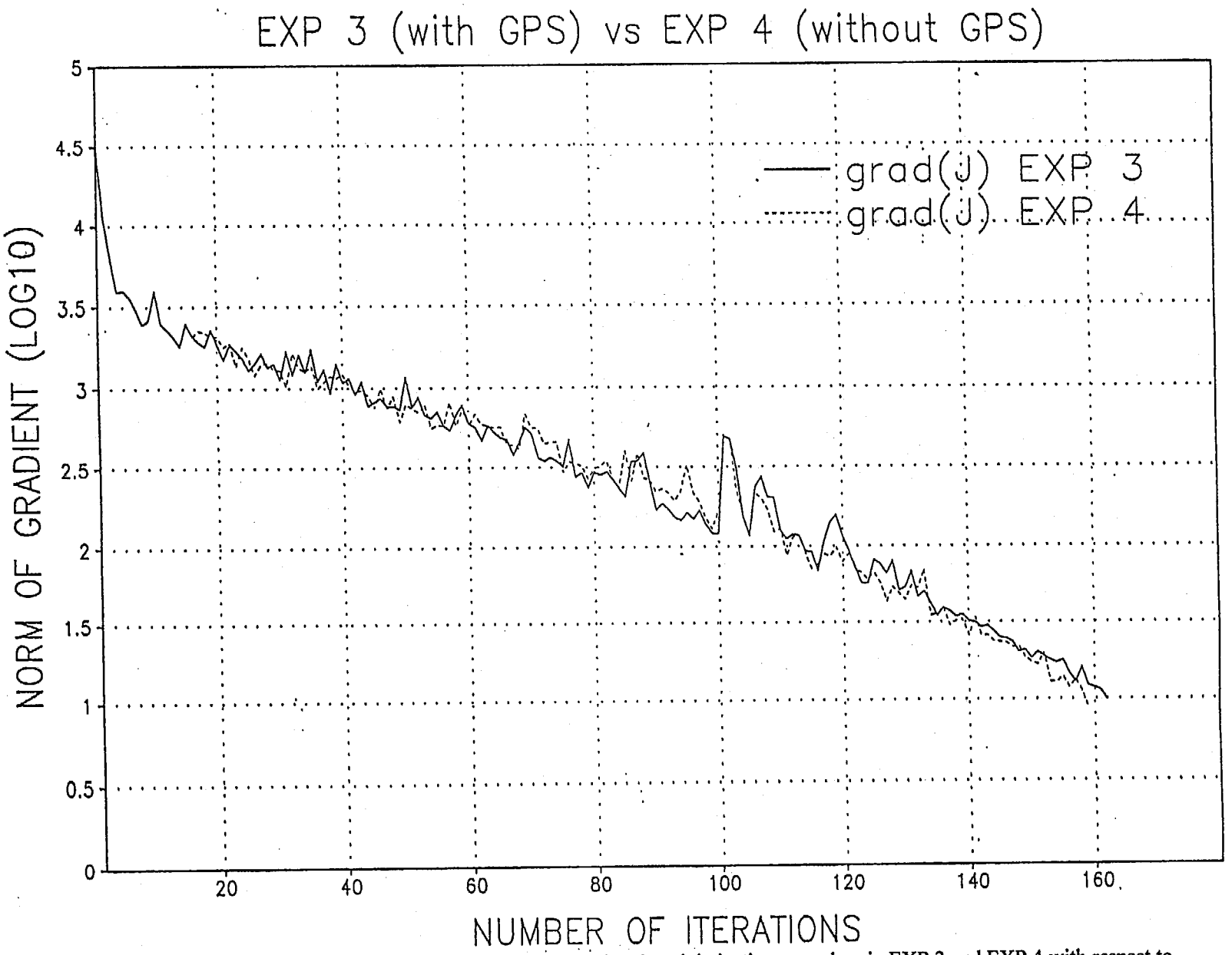

Fig. 5.31 : Norm of gradient of the cost functions during the minimization procedure in EXP 3 and EXP 4 with respect to the number of iterations. The iterations after the 100th corresponds to the second outer iteration.

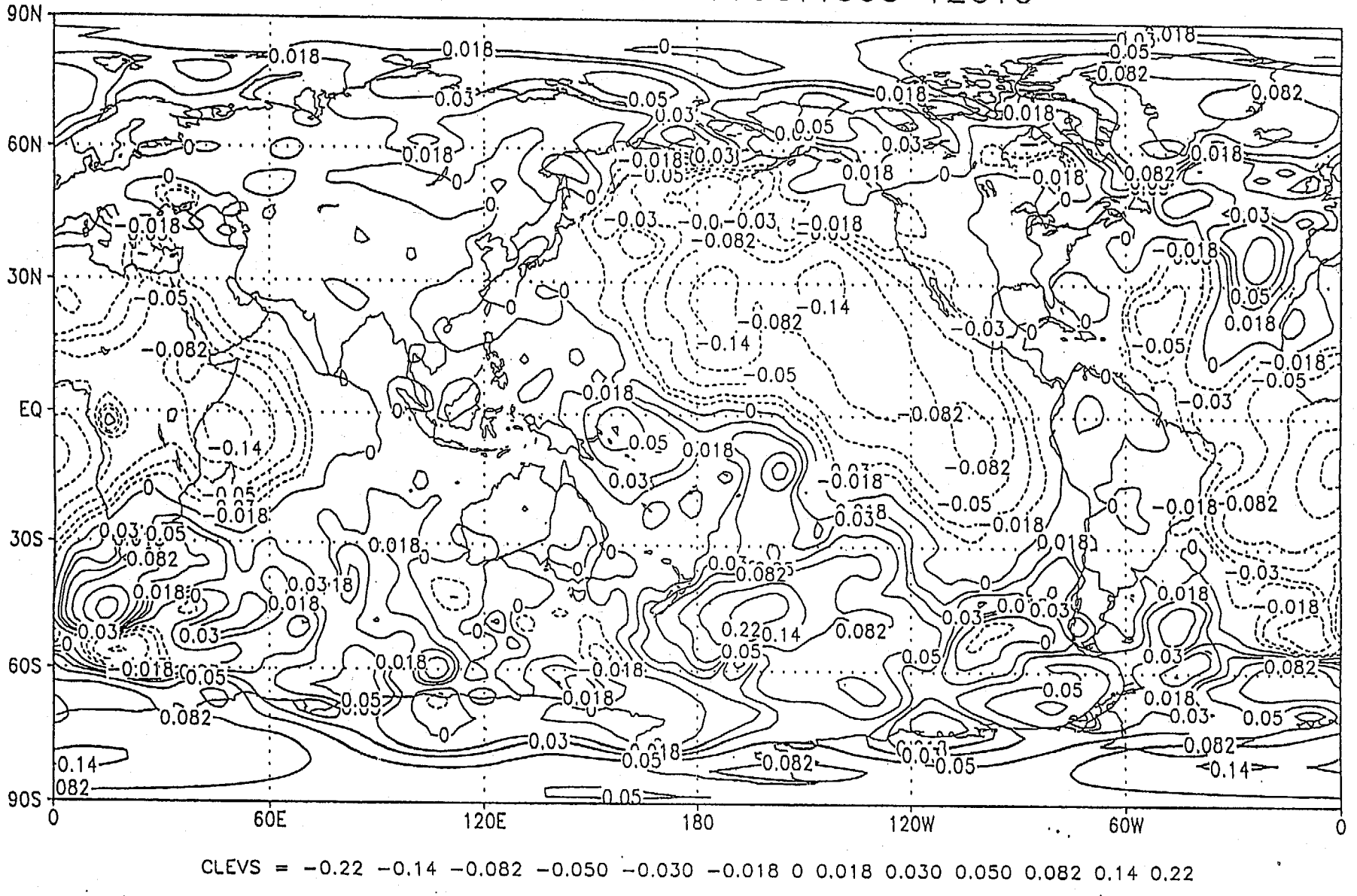

Fig. 5.32 : Difference of analyzed surface pressure between EXP 3 and EXP 4.

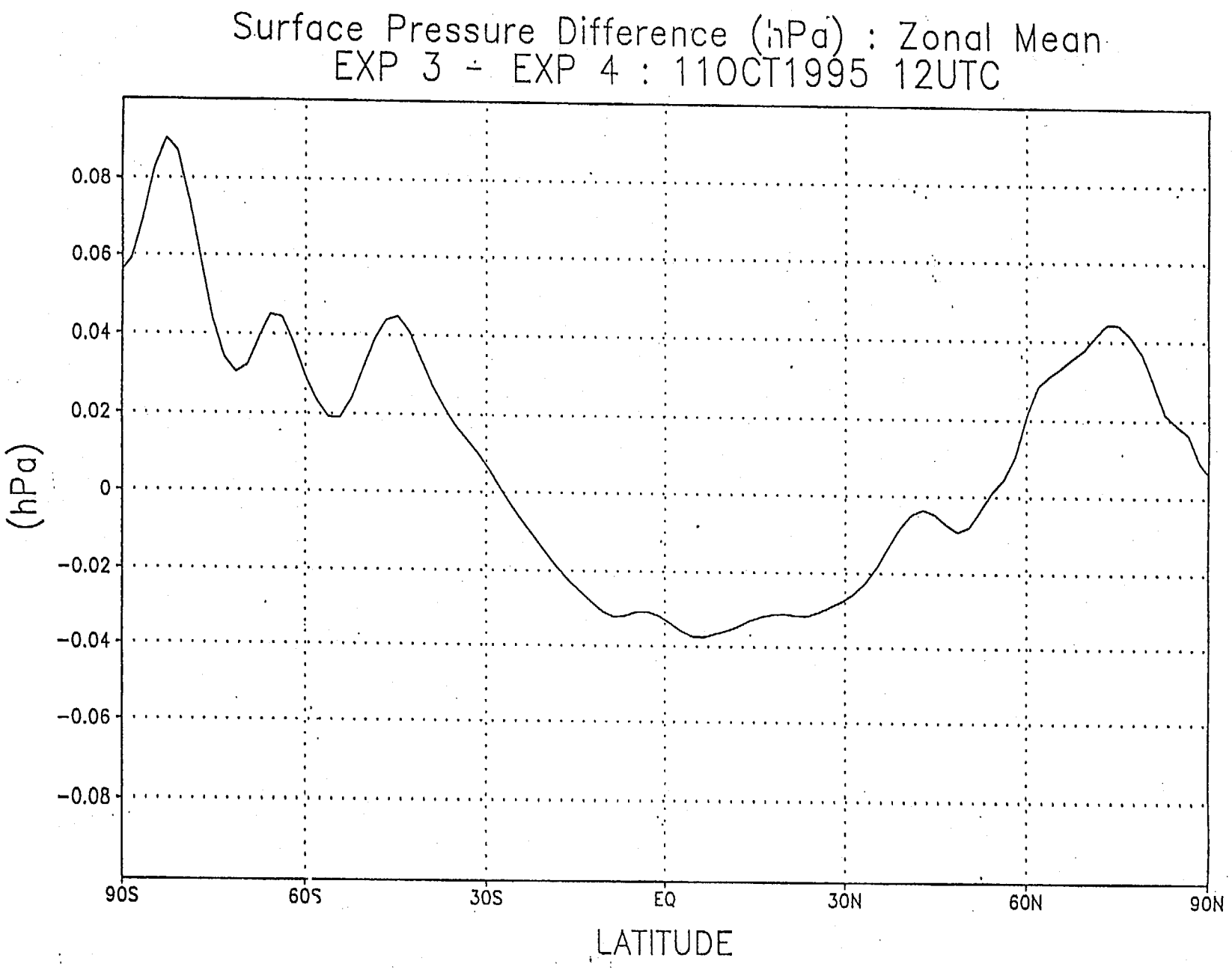

Fig. 5.33 : Zonal mean difference of analyzed surface pressure between EXP 3 and EXP 4.

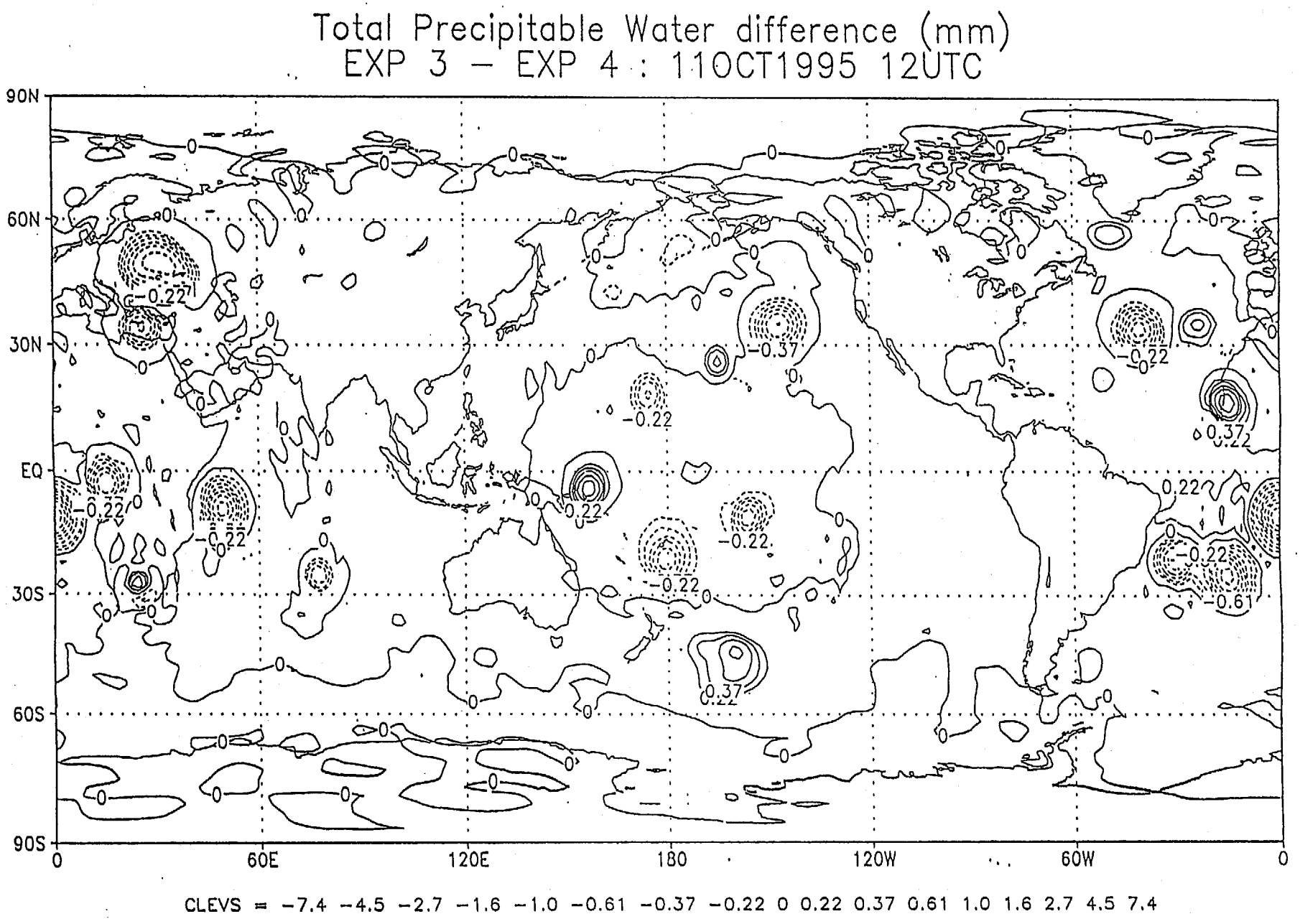

Fig. 5.34 : Difference of analyzed total precipitable water between EXP 3 and EXP 4.

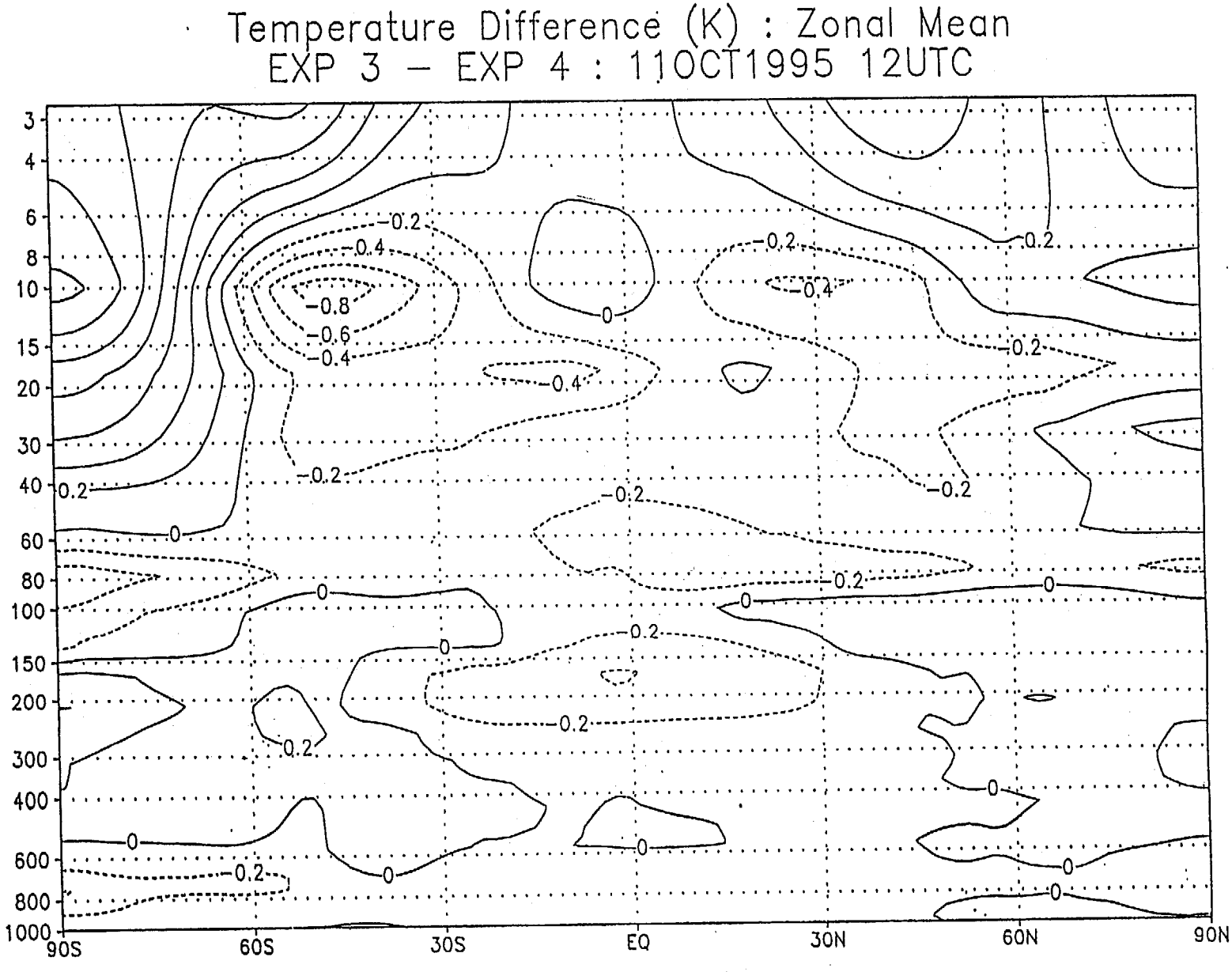

Fig. 5.35 : Zonal mean difference of analyzed temperature between EXP 3 and EXP 4.

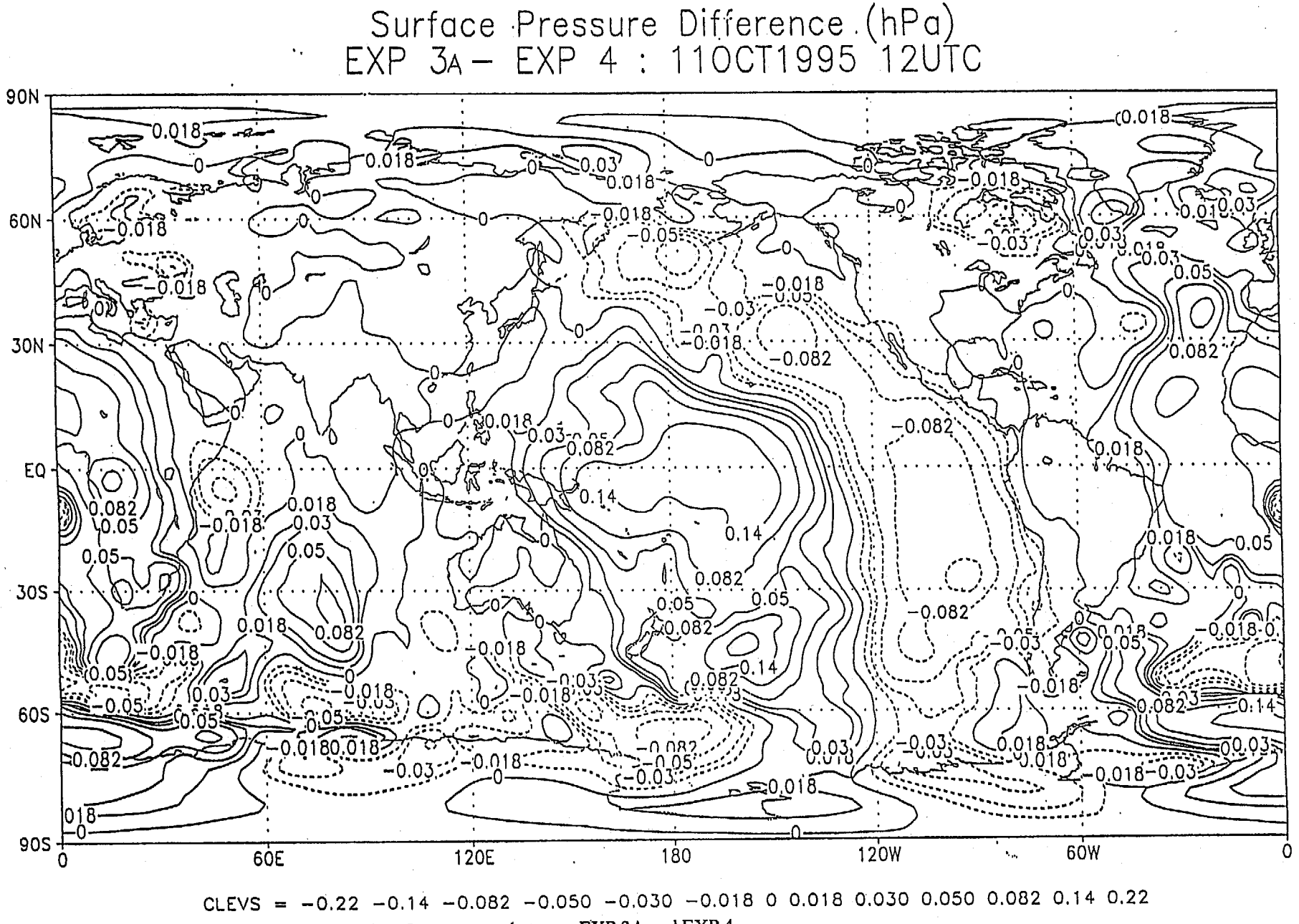

Fig. 5.36 : Difference of analyzed surface pressure between EXP 3A and EXP 4.

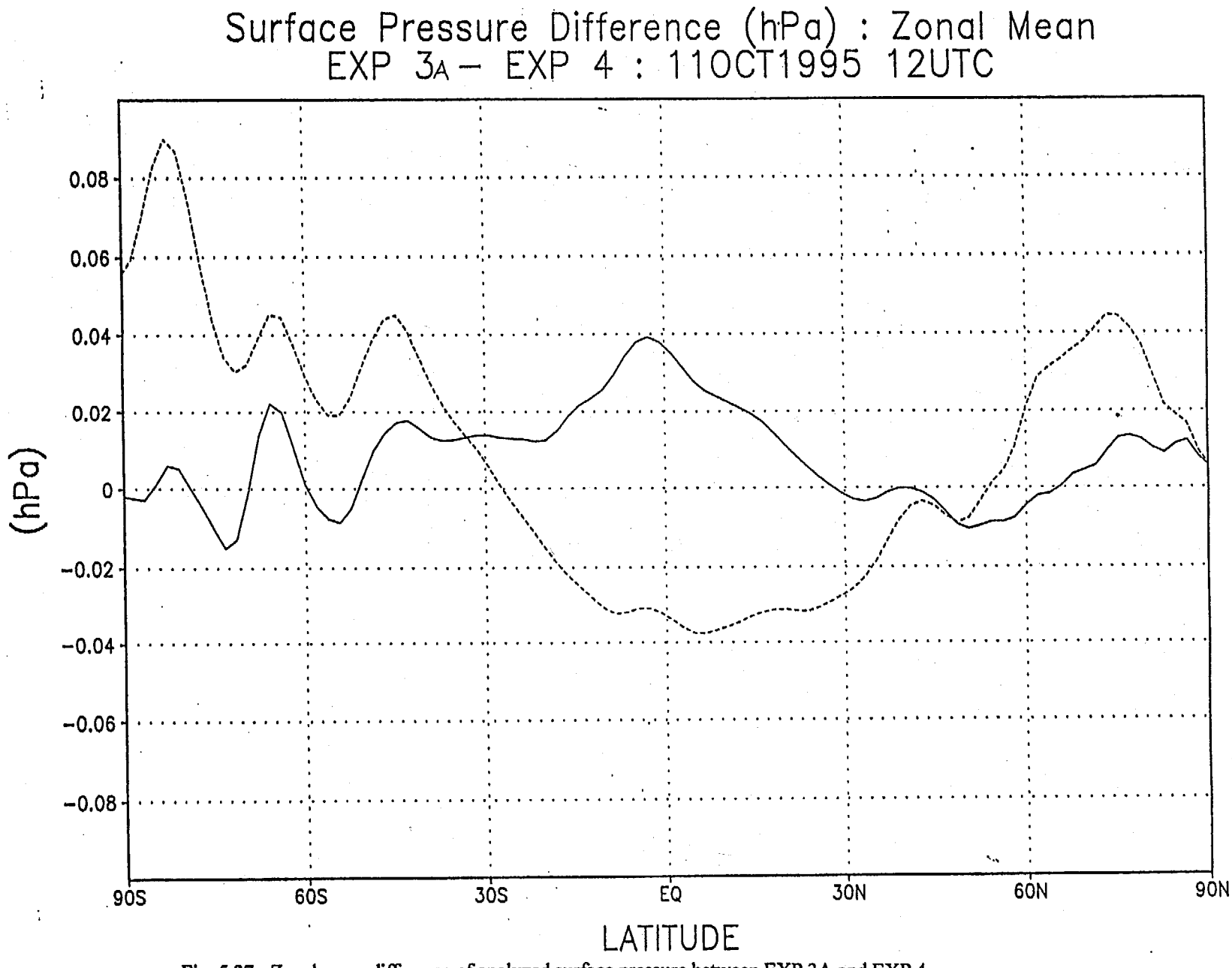

Fig. 5.37 : Zonal mean difference of analyzed surface pressure between EXP 3A and EXP 4.

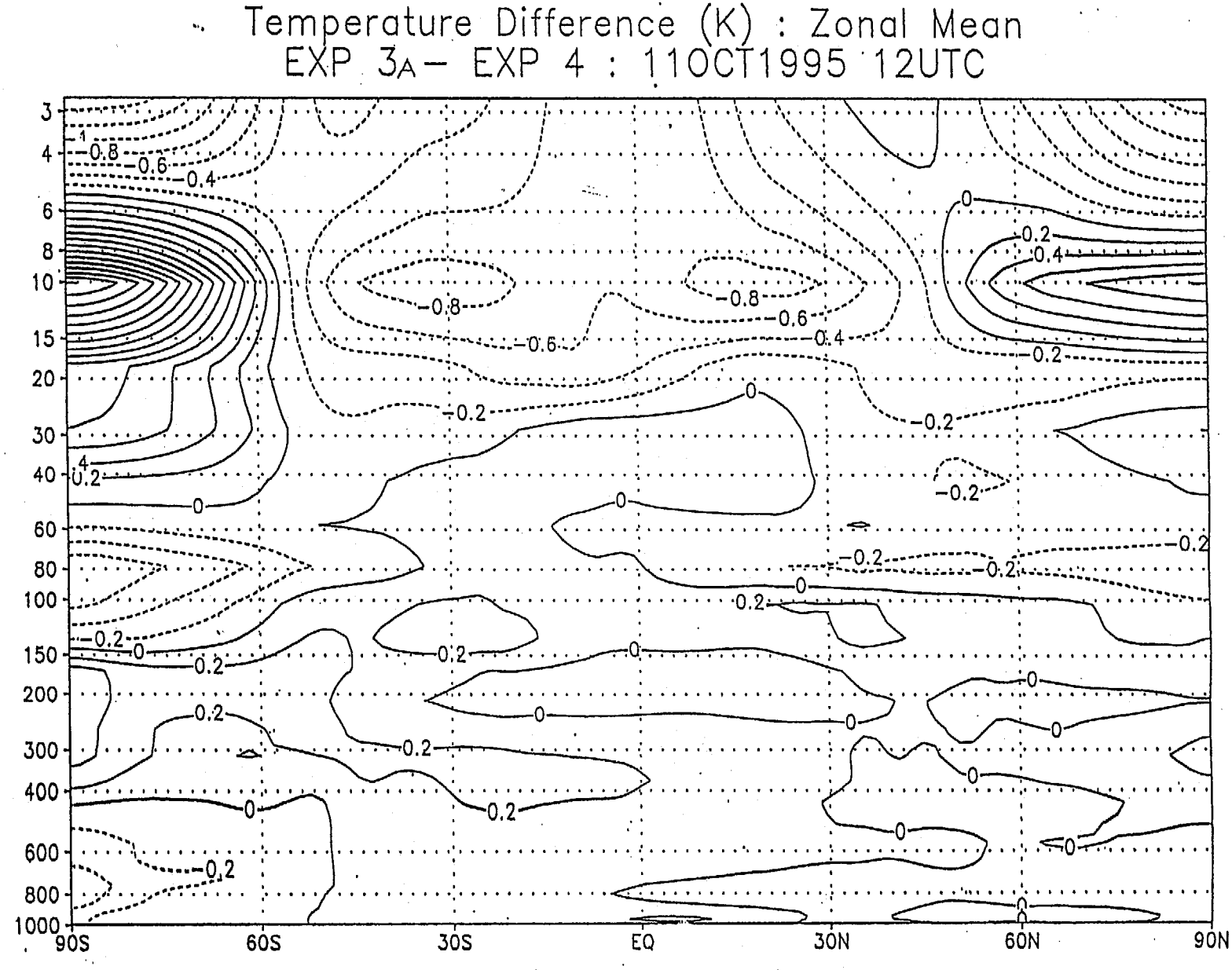

Fig. 5.38 : Zonal mean difference of analyzed temperature between EXP 3A and EXP 4.